Master thesis : Multi-material 3D printing with varying volume ratio for biomimetic application

Auteur : Grossman, Quentin
Promoteur(s) : Ruffoni, Davide
Faculté : Faculté des Sciences appliquées
Diplôme : Master en ingénieur civil biomédical, à finalité spécialisée
Année académique : 2018-2019
URI/URL : http://hdl.handle.net/2268.2/6787

Master thesis

Voxel 3D printing and bioinspired bimaterial attachment.

Quentin Grossman
June 2019

Graduation Studies conducted for obtaining the Master's degree of Civil Engineer in Biomedical by Quentin Grossman

University of Liège
Faculty of Applied Sciences
Academic year 2018-2019

Advisor & supervisor : Professor Davide Ruffoni
Jury : Davide Ruffoni , Liebset Geris , Laura Zorzetto

Preface

This master thesis was done at the university of Liège during the academic year 2018-2019 as part of the master program : "Master : ingénieur civil biomédical, à finalité spécialisée (AMUBIO009901), ATFE0016-1 Master thesis". It was done during my last year of study in biomedical engineering at the faculty of applied sciences under the supervision of Davide Ruffoni, who proposed this topic of master thesis.

Acknowledgment

I would like to thank Laura Zorzetto, who taught me everything there is to know about the use of the printer and its software as well as the MTS machine.

And a big thank to Davide Ruffoni who took me under his supervision, proposed me this subject that i personally like a lot and guided me through the realisation of all the work of this master thesis.

I am very grateful for all their advices, hints and helping hands through the year.

Contents

1 Introduction **5**
- 1.1 Additive manufacturing and multimaterial printing . . . 5
  - 1.1.1 The printer : Stratasys Objet260 Connex 1 . . . 5
  - 1.1.2 Photopolymers . . . 6
- 1.2 Voxel 3D printing . . . 7
- 1.3 Biologically inspired 3D printing . . . 9
- 1.4 Bimaterial attachment . . . 9
- 1.5 Aims . . . 13

2 Voxel 3D printing **14**
- 2.1 Material and Methods . . . 14
  - 2.1.1 Dithering pattern to fabricate blends with intermediate properties . . . 14
  - 2.1.2 Sample design for voxel size investigation . . . 16
  - 2.1.3 The polishing machine and protocols . . . 20
  - 2.1.4 Optical microscope . . . 21
- 2.2 Results & Discussion . . . 22
  - 2.2.1 Digital Material : Grey 60 . . . 22
  - 2.2.2 Sample design for voxel size investigation . . . 24
- 2.3 Conclusion . . . 38

3 Improving bimaterial attachment with voxel printing **40**
- 3.1 Material and Methods . . . 40
  - 3.1.1 Sample design . . . 40
  - 3.1.2 Sample manufacturing . . . 43
  - 3.1.3 Sample testing . . . 44
- 3.2 Results & Discussion . . . 46
  - 3.2.1 Pixel map of the graded samples . . . 46
  - 3.2.2 Crack length & fracture energies . . . 48
  - 3.2.3 Post-failure analysis . . . 52
- 3.3 Conclusion . . . 55

4 Conclusion **56**
- 4.1 Voxel 3D printing . . . 56
- 4.2 Bimaterial attachment . . . 56
- 4.3 Limitations . . . 57
- 4.4 Experimetal tests . . . 57
- 4.5 Design only achievable with 3D printer . . . 57
- 4.6 Indication for further work . . . 58
  - 4.6.1 Voxel 3D printing . . . 58
  - 4.6.2 Bimaterial attachment . . . 58

5 Bibliography **59**

6 Appendix **62**
- 6.1 Digital materials & dithering patterns . . . 62
  - 6.1.1 Random pattern in 2D . . . 63
  - 6.1.2 Error diffusion in 2D [24] . . . 63
  - 6.1.3 Error diffusion in 3D [25] . . . 65
  - 6.1.4 Ordered pattern . . . 66
  - 6.1.5 Random dithering pattern . . . 66
  - 6.1.6 Semi-random dithering pattern in 2D . . . 67
  - 6.1.7 Semi-random dithering pattern in 3D . . . 68
  - 6.1.8 Comparison between random and semi-random dithering pattern . . . 70
- 6.2 Very first sample design . . . 73
  - 6.2.1 Sample geometry . . . 73

6.2.2 Results 74
6.2.3 Conclusion 78
6.2.4 Sample design for inverse materials 78

1 Introduction

1.1 Additive manufacturing and multimaterial printing

Nowadays, additive manufacturing, commonly called 3D printing, has developed sufficiently using a broad range of different technologies and techniques to be a competitive alternative to conventional manufacturing concerning rapid prototyping, pre-series fabriction and testing as well as for final products. Additive manufacturing has the advantages over conventional manufacturing to be unlimited in the geometry and the complexity of the pieces it can produce, e.g., it is possible to print self-folding object at once [1]. However, in order to master the quality of the final product, especially if its complexity is high, it is of primal interest that every characteristics of the 3D printing process is understood.

This study will focus on the material jetting technology developped by Stratasys, called Polyjet technology, which has the advantage it can print multimaterial pieces whereas most of the other 3D printing technics can only build monolithic pieces. Multimaterial objects allow new possibilities and complexities of achievable design, mechanical properties and behaviors. However, more attention must be put into characterising the printing process and the interaction between the different printed materials.

1.1.1 The printer : Stratasys Objet260 Connex 1

The technology

The 3D printer used is the *Objet260 Connex1* from Stratasys. This printer relies on the principle of material jetting technique for additive manufacturing. This technique consists in a print-head depositing droplets, when moving along the x-axis, of photocurable polymer liquid resin on a build tray in a xy plane. It then flattens those droplets by using a roller and finally it cures them using a UV lamp, making the resin solid. The tray is then lowered along the z axis in order to proceed to the printing of the next layer. A scheme representing this technique is shown on Figure 1,

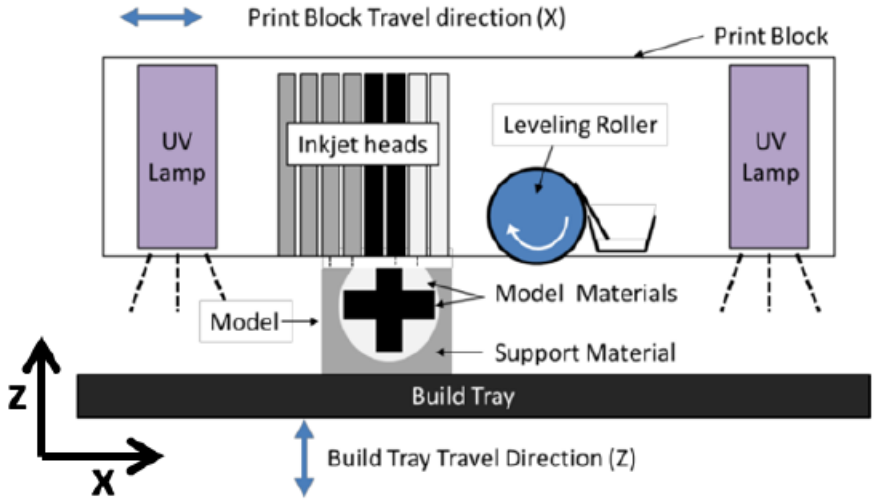

Figure 1: Representation of the Polyjet printing process [22].

The main advantage of this technique is the multimaterials possibility as there are many different nozzles on the print-head (in order to reduce the time of printing). Some of those nozzles can be filled with another resin material and deposit it on the building tray, as this resin is also photocurable, the UV lamp will solidify it as well and the two materials will be printed on the

same piece. Then it becomes possible to print at once very complex pieces with any combination of different resin-materials. Another advantage of this technique is that it is "desktop clean", meaning that the piece is built without waste of material usually obtained from spraying powder for example, waste that is common in other additive manufacturng techniques.

However the main drawback of this techniques is a huge consumption of support : as the printhead is depositing droplets of liquid resin, there needs to be a support at every layer on which the droplets can be flatten and cured otherwise the printing is not achievable. This results in a high consumption of support material for hollow structures or pieces with lots of holes. The support is printed onto the build tray exactly as the others liquid photopolymers because it is also one. The support can be easily removed by hand without the need of using a cleaning station or it can also by removed by using a water jet.

This study will investigate on the combination of especially two materials, the *VeroWhite Plus* and *TangoBlack Plus* from the *Vero* family and the *Tango* family of Polyjet materials developed by Stratasys. Those materials will be presented in the next sections.

The specifications

The specifications that are relevant for this work are the resolution of the printer in the different axis when it is printing multimaterial. This is specified by the printer as the Digital Material mode and the resolution are [1]

$$\begin{cases} x : 600\text{dpi} = 42.5\mu\text{m} \\ y : 300\text{dpi} = 85\mu\text{m} \\ z : 800\text{dpi} = 31.875\mu\text{m} \end{cases}$$

1.1.2 Photopolymers

Photopolymers are polymers that undergo polymerisation when exposed to UV light in a process called UV curing. This process transforms the liquid resin of photopolymer into a solid polymer state. The principle of this process can be seen on FIGURE 2.

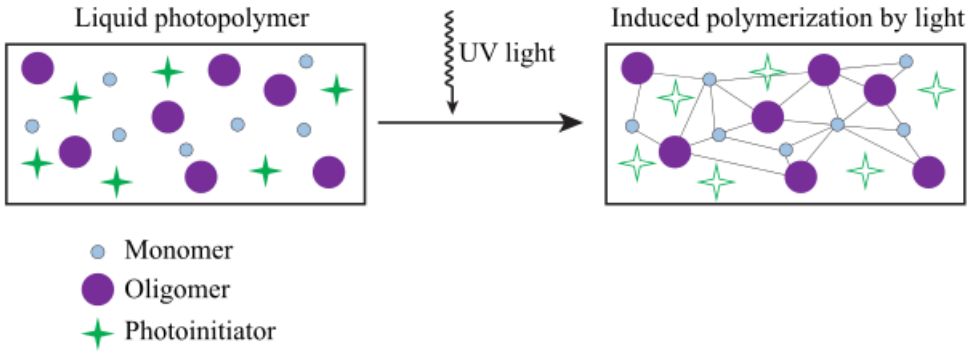

Figure 2: Representation of the photopolymerisation process induced by UV light.

The photopolymers furnished by Stratasys are from what they called the *Polyjet* technology. This technology is known for producing smooth surfaces, fine precision and diverse material properties but also its ability to deliver special properties such as transparency, flexibility and even bio-compatibility.

[1] The specifications are available at `http://usglobalimages.stratasys.com/Main/Files/Machine_Spec_Sheets/PSS_PJ_Objet260Connex1.pdf`

The support material

The support material used in this 3D printer is the SUP705, which is an acrylic compound. It is stored in a liquid form and its color is yellowish. This support material has the property to be easily removed mechanically by hand or by using a waterjet [2].

VeroWhite Plus

The VeroWhite Plus (VW+) is a material of the Vero^{TM} family. This material comes in the form a hard polymer of white color when printed. The most useful informations about this material are listed in Table 1 [3].

Property	Value
Tensile Strength	50 - 65 MPa
Elongation at break	10 - 25%
Modulus of elasticity	2 - 3 GPa
Shore hardness (D)	83 - 86 (Scale D)

Table 1: Mechanical properties of the VeroWhite Plus material

The VW+ will be used in this study and it can be considered as the hardest material in the following printed samples.

TangoBlack Plus

The TangoBlack Plus (TB+), also referred to as FLX980, is one of the material of the Tango^{TM} family. The TangoBlack Plus exhibits elastomeric properties and can be considered as a rubber-like material. This material comes in the form of a soft polymer of black color when printed. The most useful informations about the TangoBlack Plus are listed in Table 2 [4].

Property	Value
Tensile Strength	0.8 - 1.5 MPa
Elongation at break	170 - 220%
Shore hardness (A)	26 - 28 (Scale A)

Table 2: Mechanical properties of the TangoBlack Plus material

The TB+ will be used in this study and it can be considered as the softest material in the following printed samples.

1.2 Voxel 3D printing

The use of multimaterial in 3D printing allows to create various combination of voxels in order to improve the material behaviour of the printed piece [2]. Such possibilities are presented by *Hiller et al.* [11] in their study where they investigated tunable digital material properties for 3D voxel printers. The goal of this study was to explore the wide range of material properties attainable using a voxel-based freeform fabrication process, and to show the adaptability of fabricating strucutres with multiple materials using this method. They showed the possibility to fabricate auxetic materials made out of an assembly of prefabricated voxel structures that are made of different materials. They also showed the influence of the voxel microstructure pattern on the overall material properties of the structure. Such assembly can be seen on Figure 3. One can see that for

[2]Information about the support material is available at www.stratasys.com
[3]Information about the VeroWhite Plus is available at `https://www.stratasys.com/materials/search/vero`
[4]Information about the TangoBlack Plus is available at `https://www.stratasys.com/materials/search/tango`

the same volume fraction of materials and depending on the pattern of the voxel microstructure, the stiffness varies by a factor greater than 3.

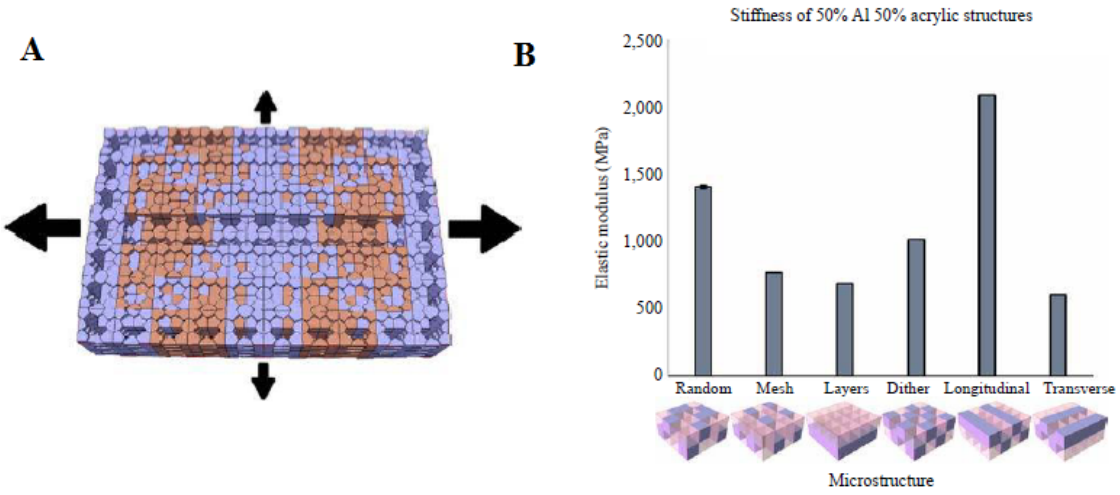

Figure 3: A : representation of an auxetic structure built out of an assembly of prefabricated voxel; B : Elastic modulus [MPa] found for different assemblies of voxels but with the same volume fraction of materials [11].

Since then, more investigation has been done on the influence of the voxel size and local distribution [3]-[5] or global distribution [26]. *Mirzaali et al.* [26] investigated the influence of the size of the voxel on the crack resistance of sample enitirely built in a chessboard pattern of bimaterials at exactly 50% volume fraction (VF) of hard material and 50% soft material. Results are that the fracture toughness and the fracture stress are both decreasing as the length scale of the voxels are increasing. A similar study but focusing on the impact strength of the printed composites has been conducted by *Swetly et al.* [9]. Their results are that the composites present an increase in impact strength by a factor 8 compare to the strongest base material. They calculated a critical voxel length of 445µm above which an increase in voxel length induces a reduction in impact strength.

A study that was using the specific voxel printing capability of additive manufacturing using bimaterials in order to improve the crack resistance of the resulting composite was conducted by *Gu et al.* who were investigating the use of an algorithm-driven design for creating fracture resistant composite materials based on a distribution of voxels of two types : one soft material and one hard [14]. They firstly used simulations to find optimised design that they then printed and tested experimentally. More than a good correspondence between the simulations and the experiments, they showed that their algorithm can produce structures that are more than two times stronger than the strongest material used and more than 20 times tougher than the stiffest material used. One can say that this methodology is very promising.

Meisel et al. investigated the impact of different VF, the distribution of multimaterial and the size of the feature on mechanical properties of jetted pieces such as the loss modulus and the storage modulus [21]. They concluded out of it in a minimal feature size that assures constant mechanical properties using this bimaterial technique. Under this size, the distribution of the bimaterials account for an anisotropy and the material properties can not be averaged on all the printed feature.

Finally, micron-scale mechanical properties of monolitic and bimaterial samples was performed using nanoindentation by *Mueller et al.* [29]. They showed that distribution of the secondary material in a base one is subjected to anisotropy resulting in elongated features of the secondary material. As a consequence, the local material characteristics are very different from the global properties of the overall printed piece. The combination of materials they used are the one defined

by the manufacturer, their printer was a Stratasys Objet500 Connex 3.

1.3 Biologically inspired 3D printing

The ability to print voxels of different materials at once opens the possibility to produce increasingly complex strucutres and systems inspired from what nature does. It is possible to break down complex multi-scale biological structures to be able to reproduce and analyse each of the differents construction principles and once they are well understood they can be combined to produce an enhanced product. Nature is a source of inspiration in this domain, as reminded by *Studart* [10] : there exist biological livings that are producing surprisingly strong structure using minerals or proteins of very different mechanical properties in order to build a structure that is very efficient, one remarkable example is bone. Bone is consisting of collagen fibrils, i.e. a soft material, with reinforcement of hydroxyapatite, i.e. a stiff material in a brick and mortar fashion [6].

Moreover, by its layer building principle, additive manufacturing is also suitable for mimicking the biological construction principles of superposing layers of materials oriented in different directions such as the planar twisted plywood composing the outer skeleton of crustaceans and insects, the concentric twisted plywood layers composing the cylindrical part of bone or plants and the cross-lamellar strucure seen in mollusk shells [10].

A study concerning the different arrangements of concentric twisted plywood layers seen in tree as been done by *Laura Zorzetto* [7]. She demonstrated that this construction principle can be reproduced using multimaterial 3D printing to obtain composites made of a cylinder base material reinforced with an helicoidal structure of fibers in its bulk. The tuning of the helicoidal fibers, i.e., their angle and their position inside this cylindrical base material lead to programmable mechanical behavior of the structure.

Another study made by *Kokkinis et al.* [8] showed the possibility to use multimaterial 3D printing to produce structures with tunable failure behavior. They were inspired from the intervertebral disc architecture that is mainly composed of the annulus fibrosus which is the hard disc of the vertebra and a soft gel core inside it. The annulus fibrosus presents a gradient of stifness and is more stiff on its outside part than the inside one. Following this gradient, they printed a similar structure and another one without this gradient of stifness. They put both sample under compression and they observed different results. While the non graded intervertebral disc shows higher stress in the inside of its annulus fibrosus and breaks from the inside to the outside, the other one presents higher stress outside its annulus fibrosus and break from this outer part in a horizontal concentric fashion. This last results shows that the interest of reproducing such architecture is to be able to reproduce tunable failure behavior in order for the structure to not damage its surrounding environment while breaking.

1.4 Bimaterial attachment

One frequent requirement that is both encountered in biology and in engineering is the question of the attachment of two dissimilar material in a robust way. Those attachments need to perform very good regarding fatigue behaviour, it is expected they can withstand loading cycles for as long as possible and it is also expected they are not damaged by high variation of forces while in use. Regarding those aspects, nature is performing better than man-made strucutres. It is of interest to focus on a specific biological bimaterial attachment : the bone-tendon interface.

Bone can be considered a stiff material as its Young's modulus is of $\approx$ 17GPa and tendon is a soft material with a Young's modulus of 500MPa. The difference of elastic properties is very high, however tendon-bone attachment is a very tough region which can sustain high forces for millions of working cycles. As the materials that can be used in the Polyjet technology presents the same difference in magnitude, it becomes possible to try to reproduce such structure to understand how every features works and possibly tuning them to obtain a programmable behaviour at bimaterial

interface.

Concerning the fatigue study of multimaterial parts, *Moore et al.* [12] [13]investigated the tensile fatigue at the bimaterial interface. They showed that multimaterial attachment present a fatigue life as long as the base materials used but they are more occurence of irregular failure.

Rossetti et al. [34] analysed more in details the tendon-bone attachement and they could highlights the main combination of features that makes it so strong as can be seen on **Figure 4**. Those main features are : 1) The collagen fibers type II that are parallel to type I but taking different orientation to attach to the bone and transfer load, 2) the type II fibers are gradually mineralized towards the bone and 3) the interface of attachment is not flat but rough, meaning there is a strong interdigitation between the two materials.

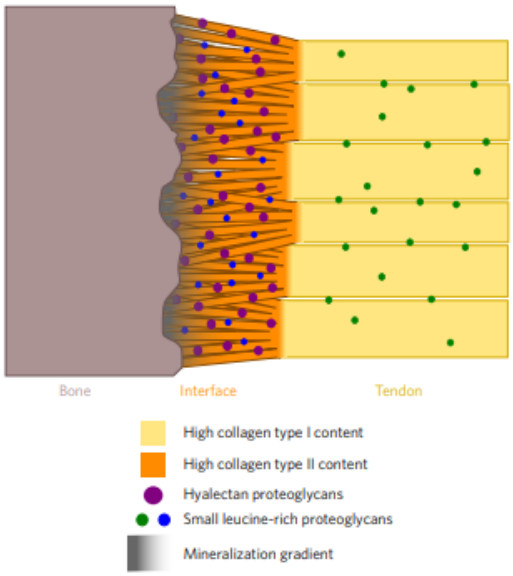

Figure 4: Collagen fibers type I at 500µm from the bone run into a transition area where both its composition and geometry is modified. Collagen fibers type II are embedded in an environment rich in different kind of proteoglycans and its mineralisation increases towards the bone [34].

Following the characteristic of the interdigitation between tendon and bone, a study of the crack propagation at the interface of two dissimilar material can be found in *Cordisco et al.* [15]. They work is of interest as they combined experimental and computational approach for investigating the relationships between patterned interface length scales, geometric features of the interface and interface toughening. They designed double cantilever beams (DCB) with a sinusoidal interface, inspired from the tendon-bone interface highlighted by *Hu et al.* as can be seen on FIGURE 5[16], and compared crack thougness for pattern differing by the sine amplitude and its length scale. They showed that fracture toughness of the DCBs increases for an increase in the A/λ ratio. They also concluded that the slip-stick behaviour of the DCBs visible on the crack propagation graphs was due mainly to the geometry of the interface.

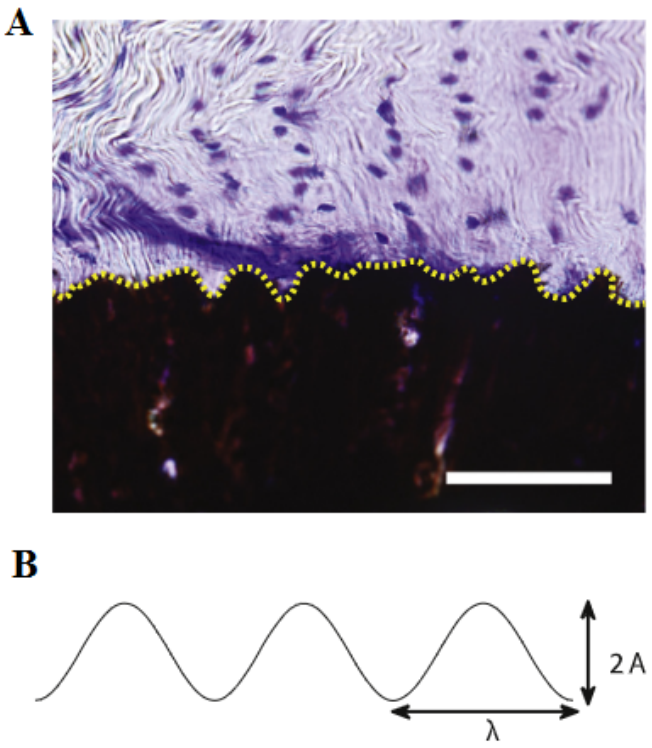

Figure 5: A : Image of the tendon-bone attachment of a mouse rotator cuff. The different tissues are in purple for the non-mineralised tissue and in black for the mineralised one. B : The interface between the two can be modeled by a sinusoid [16].

Following this trend, the influence of inclusion of defects at the sinusoidal interface has also been conducted [17]. For this, small cylindrical holes where regularly included at the interface of the two material (so along the sinusoidal interface). The conclusions are that the damage tolerance is higher for interface presenting the higher aspect ratio A/λ and that the cracks tends to propagate more at the interface than in defect-free DCBs due to the bridging between the hole inclusion.

Changing of tendon to bone construction feature, other studies are focusing on the gradual mineralisation of the interface. The influence of the printing method and the gradient of material transition on crack resistance at bimaterial attachment was investigated more recently by *Vu et al.* [32]. They designed double cantilever beam (DCB) samples using corrected beam theory [18] from which they extracted the fracture energies using a tensile test mode I as can be seen on FIGURE 6. They proceeded to tensile test for both samples but the second one had a T-peel geometry with layers of materials of intermediate volume fraction (VF) betweem the hard white polymer (VW+) and the soft one (TB+). Both samples were printed using the Polyjet technology.

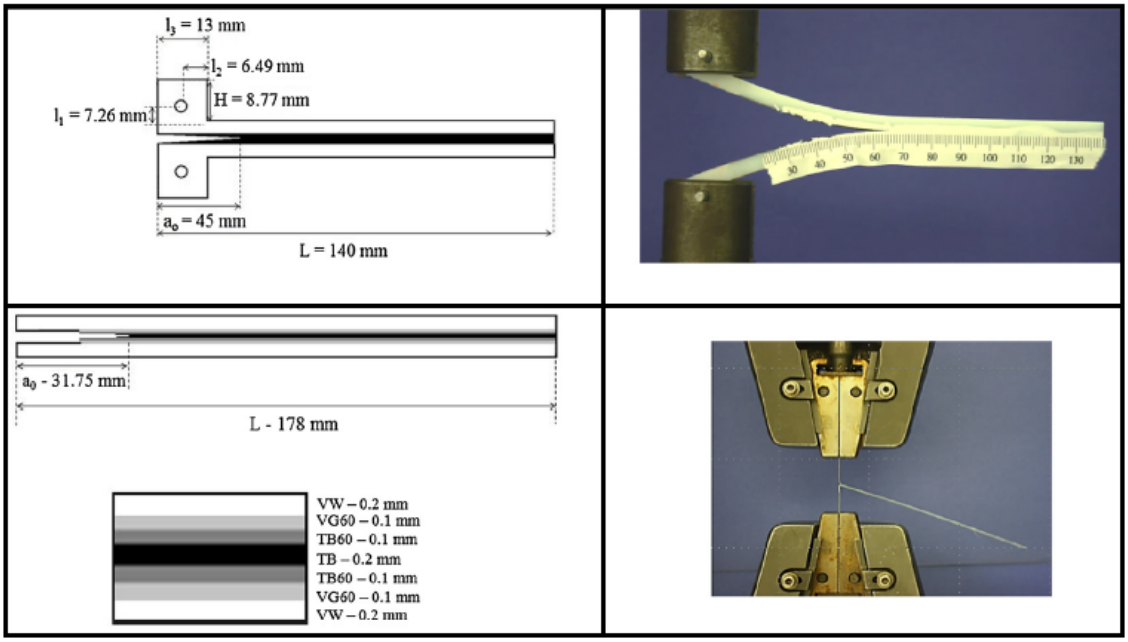

Figure 6: Illustrations of test configurations and photos of representative specimens of fully-printed DCB and T-peel geometries during testing [32]

They looked at is the influence of the different printing configurations of the samples on the building tray, see FIGURE 7, on their fracture energies and they compared the results for all configuration for each sample. What they found is that samples with their bimaterial interface in the xz-plane present higher fracture toughness and that samples designed with a gradient transition at their interface present a fracture toughness 62% higher than the one designed with a flat interface.

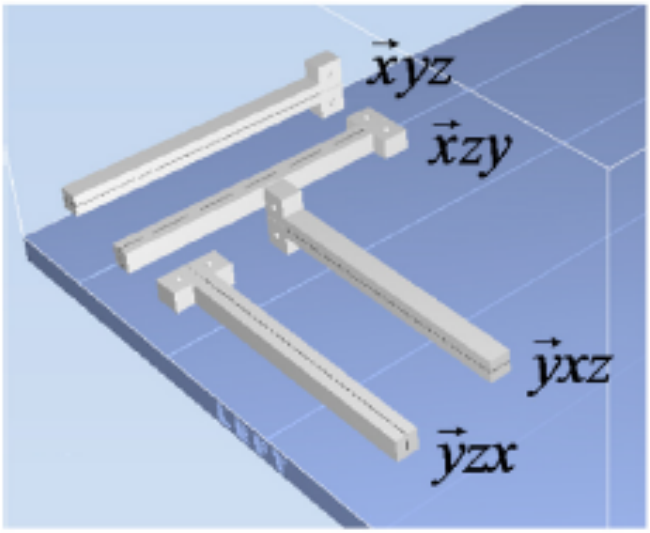

Figure 7: Illustration of various print orientations used to fabricate FP-DCB specimens with four orientations [32]

To go deeper into the gradient transition aspect, even more recently, the influence of the printing direction on the interface toughness but this time by tuning the material combination, i.e., the volume fraction, was conducted by *Lumpe et al.* [20]. They showed that some combination of

material composition and the printing direction can increases the interface strength by 20% or decrease it by 50%. They conducted their study by using the multimaterial ratios defined by the manufacturer using a Stratasys Objet 500 Connex 3 3D printer (Stratasys Ltd., Eden Prairie,MN, USA).

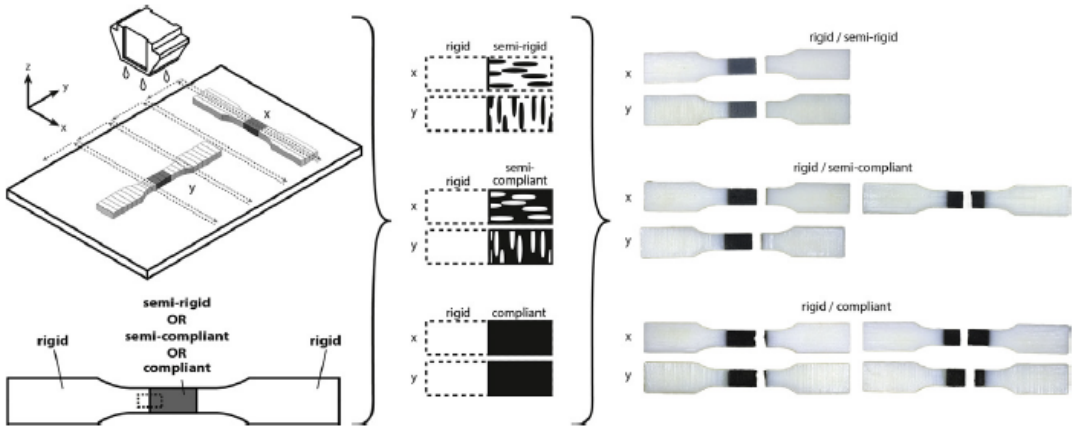

Figure 8: Illustration of the print direction and the material composition tested by *Lumpe et al.* [20]

1.5 Aims

The first part of this work will mainly focus on characterising the reliability of the printer : samples consisting in composition of a base stiff material with soft elongated features will be printed to check if the printer can correctly print features of size close to the minimal voxel size and ultimately features of the size of one voxel. To have more control, the design done will be compared to the actually printed piece but also to the final information the software of the printer is sending to the machine, which is a file under the bitmap format.

Regarding bimaterial attachment of tendon to bone interface, the present work will mainly focus on trying to mimic the gradual increase in elastic properties when moving from tendon to bone. It will mainly be inspired from the investigation of *Vu et al.* and *Lumpe et al.*. It would interesting be to go further by combining the two samples shown into one, i.e., by this time comparing the fracture energies of DCB samples printed with the same orientation configuration but with different intermediate volume fraction transistion layers at the interface between the two dissimilar materials.

The two aims at the present work can be summarised as :

1. To explore voxel 3D printing.
2. To improve bimaterial attachment using voxel 3D printing.

2 Voxel 3D printing

Firstly, this section presents the commercially available mix of digital material that can be printed by the Stratasys Objet260 Connex 1 and investigates the quality of the printed sample by looking at faces along different planes in order to detect any anisotropy or difference of quality due to the printing methods of the Polyjet technology.

Secondly, an investigation on the quality of printed elongated features reaching the voxel limit is conducted. The features are aligned parallel or perpendicular to the printing direction and differences with the designed geometry are observed. Also, a comparison between two samples made from different file processing is done in order to find the one leading to the best results.

2.1 Material and Methods

2.1.1 Dithering pattern to fabricate blends with intermediate properties

By the working principle of the printer : depositing droplets of photopolymers, using a roller to make them flat and finally curing the photopolymer with UV light, the produced pattern when using two different materials, typically VeroWhite Plus (VW+) and TangoBlack Plus (TB+), is a pixel-like mix, also called a dithering pattern. An example of a dithering pattern is visible on Figure 9. A dithering pattern can be regarded as a binary image of white and black pixels. Such a pattern is achievable because the printing done by the Polyjet technology is a discrete process : droplets are deposited by the printheads in a discrete fashion at a specific location, while they are continuously moving and so on for every specific location until the total printing is achieved.

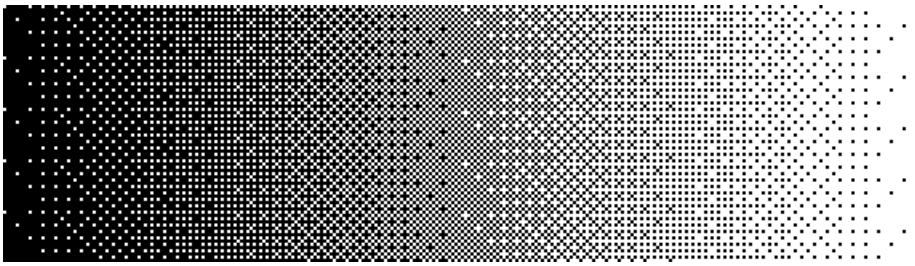

Figure 9: Example of dithering pattern

It is possible to build multimaterial piece following this dithering pattern process, printheads just need to be filled with different materials. As the size of the droplets are very small (resolution of 42.5µm in x-axis and 85µm in the y-axis), it is possible to adjust the ratio of VW+ and TB+ deposited in order to have an overall printed material with mechanical properties in between the two material used. The number of mixing ratio using VW+ and TB+ is determined by the manufacturer and is set at 12 for the Objet260 Connex1.

In order to know about the volume fraction (VF) printed, a basic beam was designed, imported into ObjetStudio and the pixel maps of eleven successive longitudinal slices were analysed in order to verify the ratio that would actually be printed. This was done for each 12 possible ratios. the results are shown on Table 3. As one can see, the standard deviation are very small, meaning the volume fraction from one slice to the other is almost the same and by so, constant.

	Grey 20	Grey 25	Grey 35	Grey 40	Grey 50	Grey 60
Average VF of TB+	0.6%	1.29%	2.51%	4.98%	9.97%	17.96%
Std VF of TB+	0.019%	0.03%	0.023%	0.023%	0.089%	0.087%
	Shore 95	Shore 85	Shore 70	Shore 60	Shore 50	Shore 40
Average VF of TB+	64.01%	75.02%	81.98%	87%	91.98%	96%
Std VF of TB+	0.097%	0.132%	0.122%	0.081%	0.06%	0.051%

Table 3: Actual mixing volume ratio found, expressed in volume fraction of TB+

It can be understood from the previous TABLE that the 12 intermediate VF that can be printed are respectively 0.6%, 1.3%, 2.5%, 5%, 10%, 18%, 64%, 75%, 82%, 87%, 92%, 96% in VF of TB+. There is a big gap of values between 18% and 64% that can not be printed, solutions to be able to print any VF for a dithering pattern with different distribution strategies is investigated in the appendix. However, the impact of material VF and distribution on composite part made of multimaterials are investigated also by *Meisel et al.* [21] but less extensively and by *Mirzaali et al.* [26] but only for ordered pattern.

The commercial names of those intermediate gradients, when ranging from the hardest to the softest, are Grey 20, Grey 25, Grey 35, Grey 40, Grey 50, Grey 60, Shore 95, Shore 85, Shore 70, Shore 60, Shore 50 and Shore 40.

It is thought that the name *Shore* is an indication of the hardness of the material and of its composition. *Shore* is the indication of hardness for elastomers and others rubber-like polymers, the higher the number on the scale, the greater the resistance to indentation and thus the hardness of the material. As one can see on TABLE 3 for the Shore intermediate gradients, the higher the volume fraction of TB+, the lower the number of the scale, which is consistent as TB+ is an rubber-like polymer. However, the name *Grey* do not refer to any hardness measure to the knowledge of the author.

Digital material : Grey 60

An investigation is conducted on the faces of a sample of printed using multimaterials. The goal is to do a visual inspection of the faces of the sample to see if there is any differences or anisotropy of results due to the printing methods. To do so, a sample of size $14x10x11.2$mm is printed in the multimaterial Grey60 intermediate gradient. The orientation of the sample on the building tray can be seen of FIGURE 10, such as done by *Mueller et al.* [29]. The xy-face and the yz-face will be polished and examined visually.

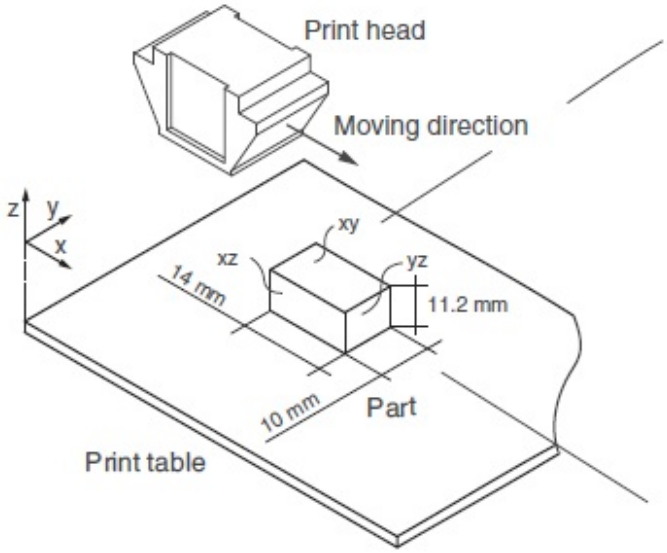

Figure 10: Orientation of the sample on the building tray [29]

2.1.2 Sample design for voxel size investigation

Pixel map of *ObjetStudio*

ObjetStudio is the software developped by Stratasys and furnished with the printer that allows to prepare the samples : orientation, layout of multiple pieces on the building tray, materials used, printing mode,... before proceeding to printing. It is a necessary step to use this software as it is from it that the printing is launched. Moreover, this software only read .STL file. A .STL file is a format of file standing for "Stereolithography" or "Standard Triangle Language", it is a format used by everyone who is working with Computer Assisted Design software (CAD) and so it is a format used in 3D printing and rapid prototyping. Such a file is composed of a representation of a CAD approximated by triangles all connected that defines a shell on the perimeter of the CAD. Such a representation of a .STL file is shown on FIGURE 11 [5].

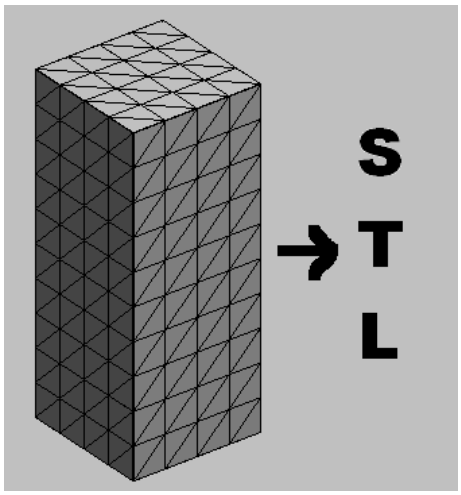

Figure 11: STL representation of a rectangular beam.

It is possible to extract from *ObjetStudio* an interesting information which is the .bmp files that

[5]Image taken from www.Mathworks.com

the software sends to the printer in order for it to proceed to printing. They are the final files read before printing. In order to understand in details and to have more control on what is happening, those .bmp files, called "pixel map", will be extracted and compared to the microscope images obtained from the printed polished samples used for the design of benchmark. The pixel maps are .bmp files representing the successive layers of material that the printer will deposit one after another. They are a pixelised representation of the dithering pattern of one layer with information such as the materials that will be deposited as well as the support. Such a pixel map is visible on FIGURE 12. The software obtains those images by slicing the .STL file into layers stacked along the z-axis, the thickness between those layers is the thickness of the deposited droplets.

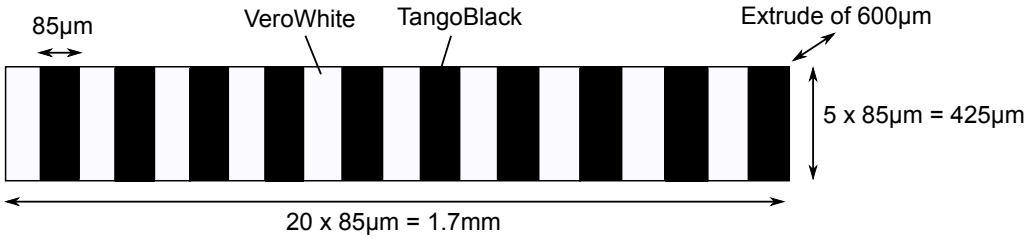

(a) Desing of a beam in bimaterial

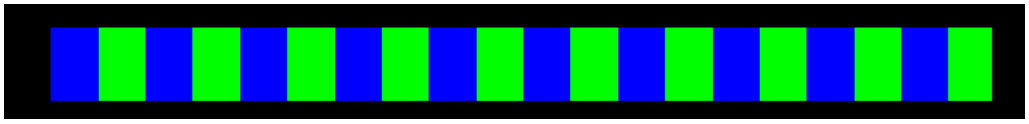

(b) Pixel map of the beam in ObjetStudio

Figure 12: Design and pixel map of a beam in ObjetStudio. The VW and TB are respectively represented in blue and green on the pixel map.

Sample geometry

The design of the sample is made to analyse the capability of the printer to repeatably print elongated features of different dimensions and to investigate the printing directions quality, the smaller dimensions that it can correctly print as suggested for making a design strategy of benchmark [27], [28]. The CAD is done using IronCAD software and extraced as a .STL file. Once printed, the sample will be polished, images at the microscope will be taken and compared to the pixel maps sent to the 3D printer by the post-processing software *ObjetStudio*, which is the final software to use for printing samples.

The design is visible on FIGURE 13. It is designed with a resolution of x : 42.5µm ; y : 85µm ; z : 31.75µm to be sure that the division of any length will give an entire multiple number of pixels. The bulk in which the features are is now a square for convenience and there has been a re-positioning of the features more symmetrically around the center in order to obtain a better polishing. This geometry will be extruded of about 6cm along the z-axis.

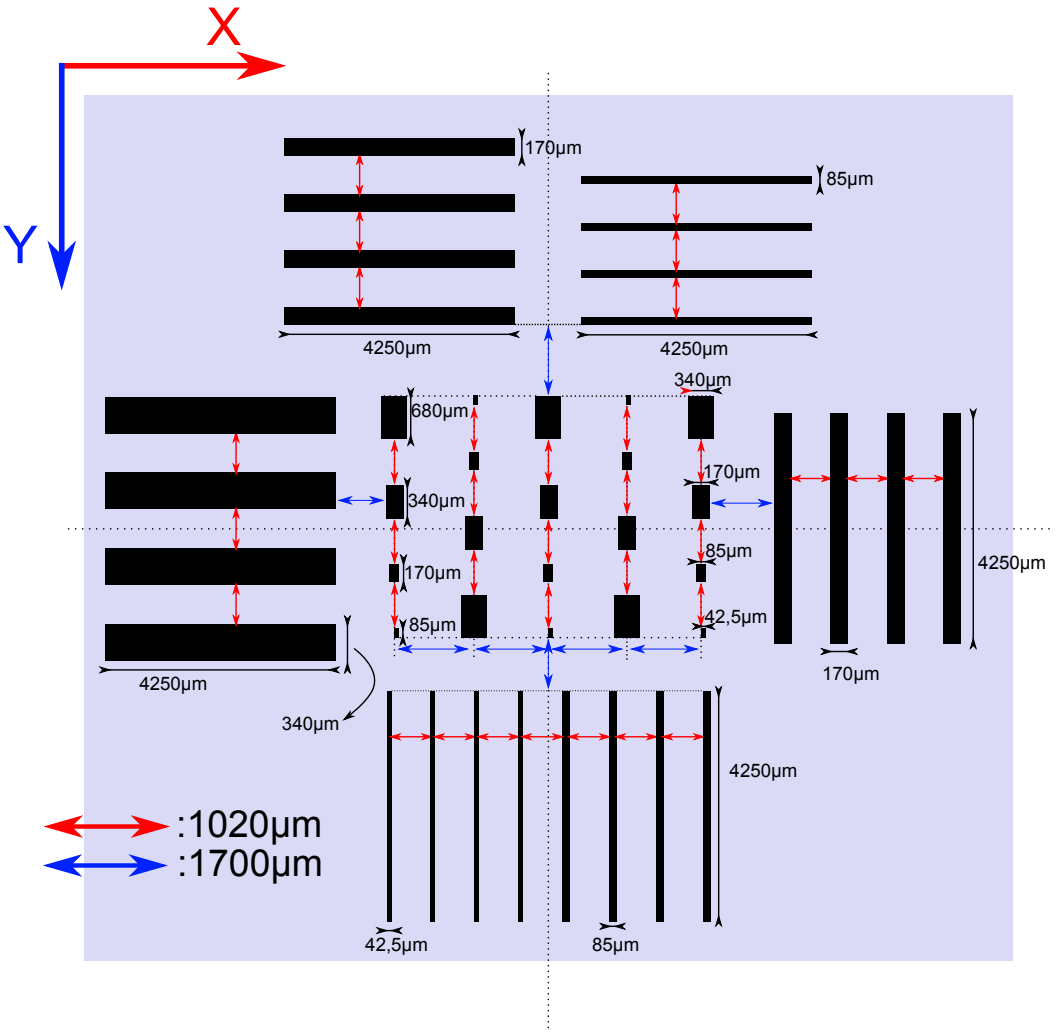

Figure 13: Sample design

The sample presents lines of length 4250µm and of various width, as well as squares of various dimensions. The dimensions of the features are :

- Four horizontal lines of dimensions 4250µm x 340µm.
- Four horizontal lines of dimensions 4250µm x 170µm.
- Four horizontal lines of dimensions 4250µm x 85µm.
- Four vertical lines of dimensions 4250µm x 170µm.
- Four vertical lines of dimensions 4250µm x 85µm.
- Four vertical lines of dimensions 4250µm x 42.5µm.
- Five squares of dimensions 680µm x 340µm.
- Five squares of dimensions 340µm x 170µm.
- Five squares of dimensions 170µm x 85µm.
- Five squares of dimensions 85µm x 42.5µm.

Identification and reduction of critical steps

Along the designing process, three critical steps were identified. Each one directly following each other. Those three critical steps are :

- (i) The CAD software, because it could not achieve the high precision required at the order of the 0.1 µm. Instead the CAD software would approximate the length at the order of the micrometer, sometimes rounding it up, sometimes rounding it down, leading to errors in the design lengths of the features.
- (ii) The .STL generation, because the design is directly exported into an .STL file from the CAD design. No control is then possible on the .STL file generation.
- (iii) The software *ObjetStudio*, because there is no control from the user over the slicing of the .STL file imported and so on the pixel map created.

A representation of the process path of a file is shown on Figure 14 A. In order to reduce those critical steps, it is chosen to design the samples directly from a stack of bitmaps that are then converted into .STL using an open source code in *Matlab*. Two steps are then controlled : the CAD step is removed as the design is done using bitmaps, there is then no approximations of values, it can be as much precise as the resolution put at the step of creating the .STL and the .STL generation is controlled by the voxel resolution. This shortened process path is represented on Figure 14 B.

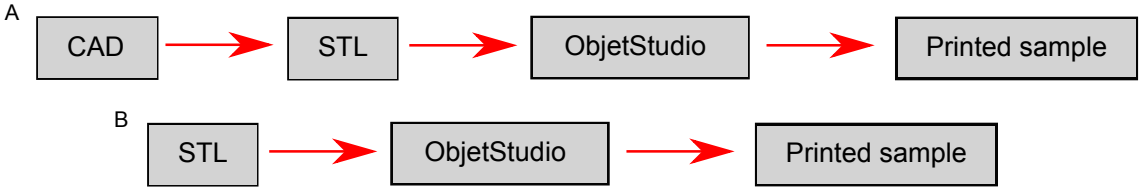

Figure 14: Representation of the file processing when : A, starting from a CAD; B, starting from the .STL

Only the step involving *ObjetStudio* cannot be avoided with the Connex printer used. However, it is expected that as the resolution to generate the .STL is the same as the one used during the generation of the pixel map, the result will be at best.

Direct .STL generation

By making directly the .STL from stacks of bitmaps it is then possible to avoid using a CAD, its uncertainty on the precision of the design and also to avoid the process of exporting from the CAD software into a .STL file.

The advantage is that the resolution of the .STL be equal to the one of the printer in the different printing directions to have the best results for the smallest features. As a reminder , for the Objet260 Connex 1 used, the resolution in digital material mode is

$$\begin{cases} x : 600\text{dpi} = 42.5\mu\text{m} \\ y : 300\text{dpi} = 85\mu\text{m} \\ z : 800\text{dpi} = 31.875\mu\text{m} \end{cases}$$

The design used for the generation of the .STL will be the one of Figure 13 in order to compare the results between the samples printed using a CAD and using the own .STL generation.

2.1.3 The polishing machine and protocols

The machine used to polish all the samples is a MaetaServ®250 grinder-polisher from Buehler visible on FIGURE 15.

Figure 15: Polishing machine of Buehler

The polishing procedure used is the one recommended for polymers by Buehler on their website [6]. This procedure, visible on FIGURE 16, was strictly followed as the abrasive and material used were the one indicated.

Sectioning	Precision Saw with 30HC blade recommnded for polymers				
Mounting	Castable, typically EpoThin 2				
Surface	Abrasive / Size	Load - lbs [N] / Specimen	Base Speed [rpm]	Relative Rotation	Time [min:sec]
CarbiMet	320 [P400] grit SiC water cooled	4 [18]	300		Until Plane
CarbiMet	400 [P800] grit SiC water cooled	4 [18]	300		1:00
CarbiMet	600 [P1200] grit SiC water cooled	4 [18]	300		1:00
CarbiMet	1200 [P2500] grit SiC water cooled	4 [18]	300		1:00
TexMet C	3 µm MetaDi Supreme Diamond	5 [22]	150		4:00
MasterTex	0.05 µm MasterPrep Alumina	3 [13]	150		3:00

Figure 16: Polishing protocol for polymers

[6] Image of the protocol of FIGURE 16 taken from www.buehler.com

2.1.4 Optical microscope

The microscope used is an optical microscope model Olympus BX60M, as can be seen on FIGURE 17, coupled with a recording software called *Stream motion*, allowing to process to reconstructed images being the concatenation of series of microscopic images of a wide sample area as can be seen on FIGURE 18.

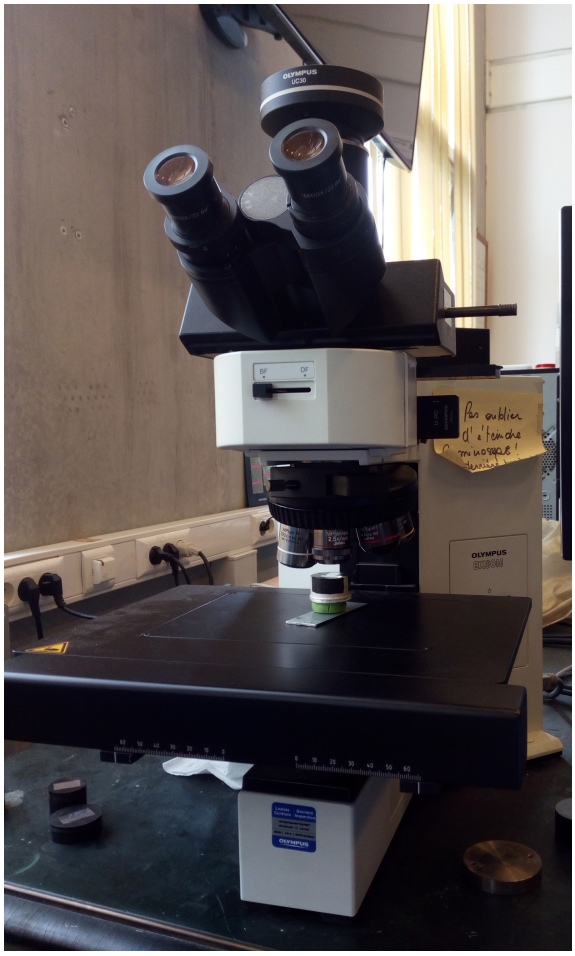

Figure 17: Microscope Olympus BX60M

Figure 18: Reconstructed image made of a concatenation of 72 microscopic images. 6 microscopic images are highlighted in red on the top right corner.

2.2 Results & Discussion

2.2.1 Digital Material : Grey 60

First, the xy-face is inspected on FIGURE 19. One can see that the TB+ inclusion are elongated along the x-axis, which is the direction of the printheads when they deposit droplets. This is due then to an inertia effect because of the speed of the printheads. However, this elongated geometry is not as prominent as on FIGURE 19 because the voxel size that is of 42.5µm along the x-axis and 85µm along the y-axis and that plays as a counter-effect. One can also see the wavy pattern that is repeating, it is characterisc from a good polishing of the xy-plane when polishing sample made with those Polyjet materials.

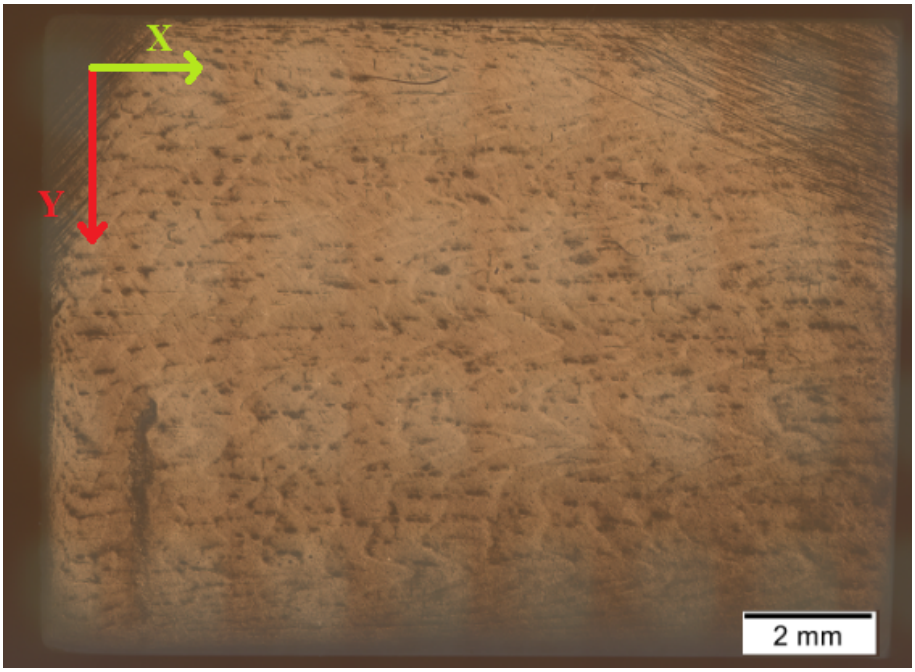

(a) Image of all the yz-plane

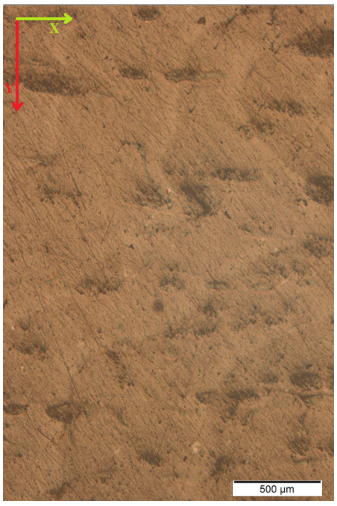

(b) Image of a 2.5x magnification at the yz-plane

Figure 19: Microscope images of the xy-plane polished at the level of 3µm of the sample of Grey60 with magnification of 1x, 2.5x [31]

Second, the yz-face is inspected on FIGURE 20. One can see that the face is very different from the previous one. The inclusion of TB+ are more numerous, more easily distinguishable and they are also elongated along the y-axis but more than the inclusion of the previous FIGURE. This elongated geometry has to be seen at the light of the resolution of the printer, which can be seen as the voxel size, that is of 85µm in the y-axis and 31.75µm in the z-axis. Moreover, this elongated geometry is most probably increased by the factors suggested by *Mueller et al.* [29] : the fast speed of the printheads not allowing for a clear punctual deposition of the droplets because of the ineria in the droplets and due to the rheology of the ink of photopolymers.

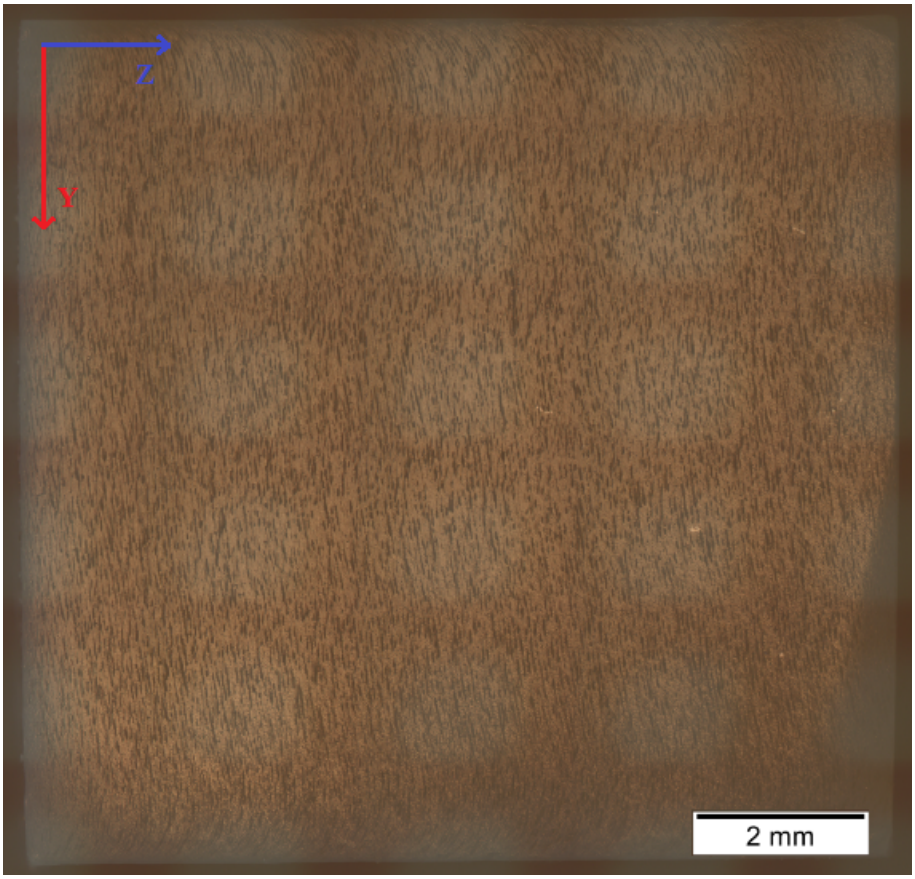

(a) Image of all the yz-plane

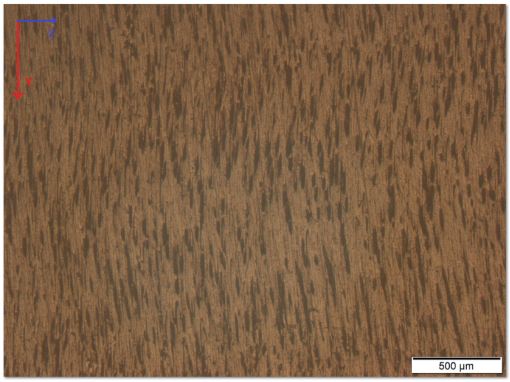

(b) Image of a 2.5x magnification at the yz-plane

(c) Image of a 5x magnification at the yz-plane

Figure 20: Microscope images of the yz-plane polished at the level of 3µm of the sample of Grey60 with magnification of 1x, 2.5x and 5x [31]

The results of the faces of the multimaterial sample of Grey60 shows that there is a strong anisotropy in the geometry of the TB+ inclusion depending on both the printing method and the voxel size of those inclusion.

2.2.2 Sample design for voxel size investigation

The pixel map and the polished surface of both samples can be seen on FIGURE 21. A detailled comparison of the horizontal lines, vertical lines and squares between the two samples will be done in the following section based on their respective pixel map and the measure of the lengths and the widths of the differents features on the polished surface of both samples. For facility, the sample

designed using *IronCAD* software will be referred to as the "CAD sample" and the sample designed directly in .STL will be referred to as the ".STL sample".

One can see the difference of quality of the sample surfaces, it is because of a difference of polishing. The difference of polishing is that the CAD sample is polished until 0.05µm and the .STL sample is polished until 3µm. The author could not achieve polishing up to 0.05µm on the .STL sample because everytime this level of polishing was reached, a strange hard phase of grinded material was solidying on the surface of the sample, completely hiding all the features and so no matter the cleaning that was done after polishing. For this reason it was chosen to stop the polishing at the level of 3µm.

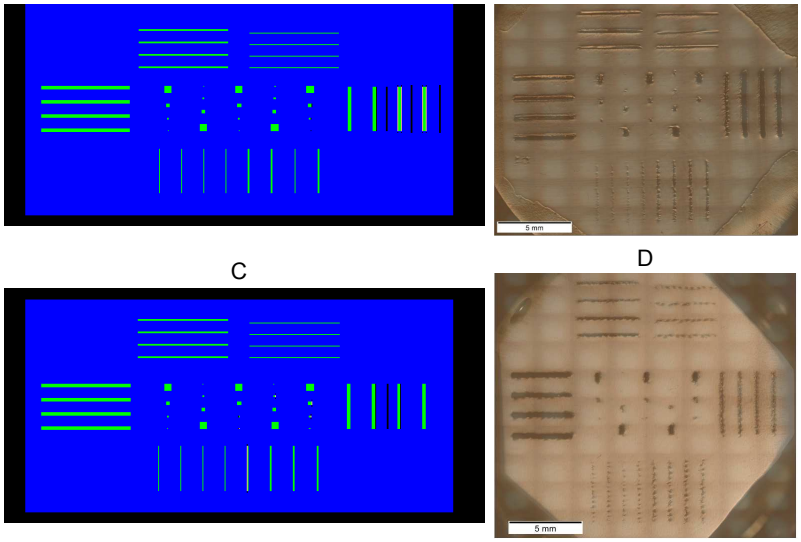

Figure 21: Representation of both samples for : A, the pixel map of the CAD sample; B, the polished CAD sample; C, the pixel map of the .STL sample; D, the polished .STL sample.

Lines parallel to printing direction

On FIGURE 22, the horizontal lines of width 340µm can be seen. The pixel map of both sample do not exhibit any defect, they both respect the designed width of 4 pixels and the result on the printed sample is also good, the polished lines are correctly drawn and respect the geometry of their pixel map. The only difference between the two polished samples being a small staircase effect on the lower edges of the .STL sample that is due to the less fine polishing.

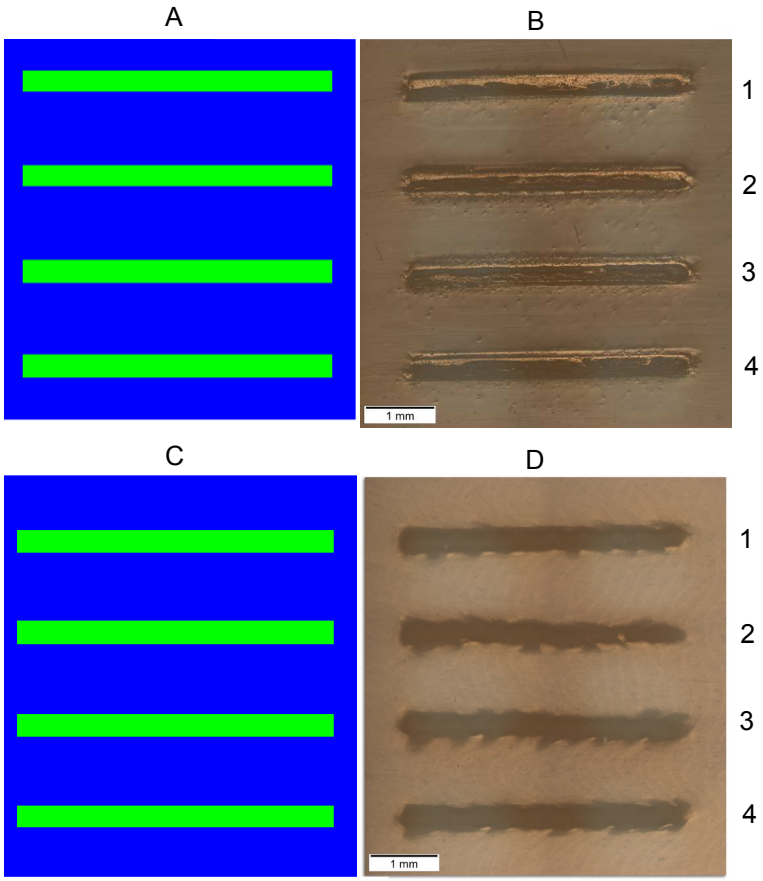

Figure 22: Representation of the horizontal lines of width 340µm for : A, the pixel map of the CAD sample; B, the polished CAD sample; C, the pixel map of the .STL sample; D, the polished .STL sample.

One can see on FIGURE 23, the bargraphs representing the lengths and the widths of the lines supposed of FIGURE 22 B and D. The lines of the CAD sample are generally a bit shorter than the one of the .STL sample, with their respective mean at 4204µm and 4259µm. The .STL sample is then closer to the designed value of 4250µm than the CAD sample and presents a smaller standard deviation than the CAD sample.

Concerning the width of those lines, both samples presents a mean width over their four lines of 335µm, so a bit below the designed value of 340µm, but one can see that the CAD sample exhibits a smaller standard deviation in this case.

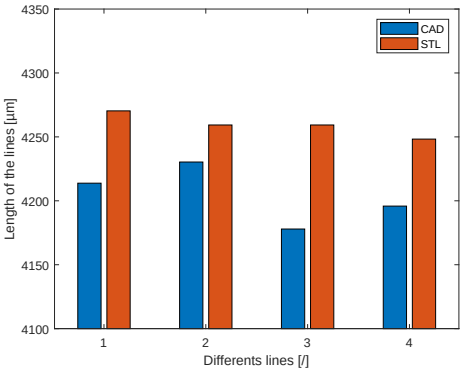

(a) Measured length of the lines supposed to be of length 4250µm

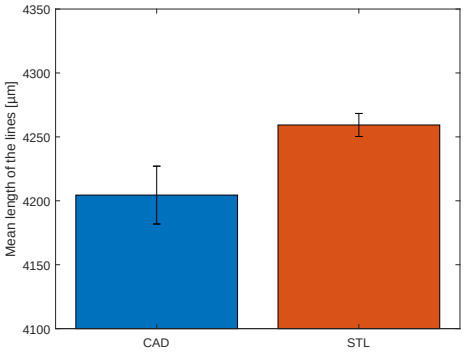

(b) Mean length of the four lines measured

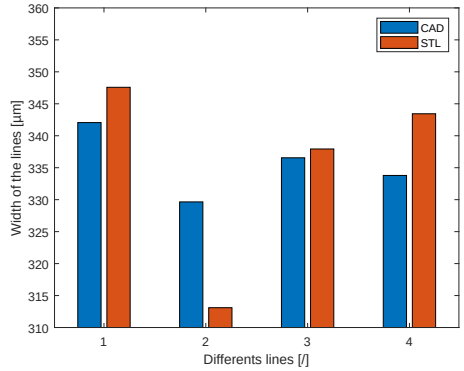

(c) Measured width of the lines supposed to be of width 340µm

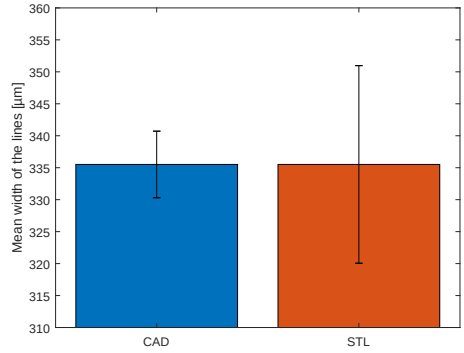

(d) Mean width of the four measured lines

Figure 23: Comparison of the measures of the lengths (a) and widths (b) of the polished horizontal lines supposed to be of 4250µm x 340µm and their mean length (c) and width (d).

Concerning the small horizontal lines of width 170µm and 85µm of the CAD sample, both the pixel map and the sample features on FIGURE 24 A and B are of correct dimensions and good quality. The lines are well drawn, the edges are clear and there is no defect. Except for the third thinner line on the right which seem to have an edge crossing its length diagonaly, there is no clear reason why but it is expected this problem comes from the polishing or the cleaning after polishing.

The results for the four horizontal lines of width 170µm and width 85µm of the .STL sample can be seen on FIGURE 24. First for the pixel map, all lines exhibit correct dimension and geometry, the lines of width 170µm are exactly 2 pixels wide and the lines of width 85µm are exactly 1 pixel wide. The pixel map is perfect for those lines. For the printed polished results, the observations are less good : the four lines of width 170µm are still continuous lines even though there is a strong staircase effect on one or both sides of the lines. The four lines of width 85µm, however, are not continuous anymore. They are composed of small packs of TB+ separated by regular VW+ cut through the lines. This lack of continuity in the thinnest lines is supposed to be due to the polishing that was stopped at 3µm.

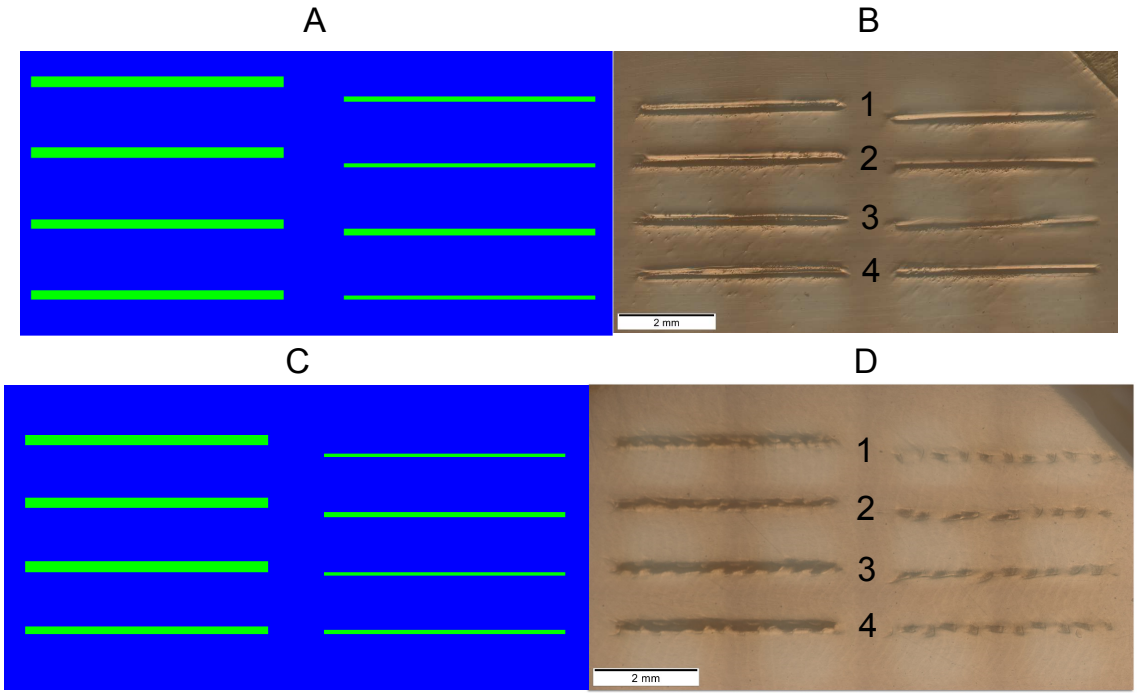

Figure 24: Representation of the horizontal lines of width 170µm (on the left) and 85µm (on the right) for : A, the pixel map of the CAD sample; B, the polished CAD sample; C, the pixel map of the .STL sample; D, the polished .STL sample.

One can see on FIGURE 25, the bargraphs representing the lengths and the widths of the lines on the left of FIGURE 24 B and D. Their lengths are more or less similar except the first line of the CAD sample which is longer. Their respective mean are 4282µm and 4255µm. The .STL sample is then closer to the designed value of 4250µm than the CAD sample and presents a smaller standard deviation than the CAD sample.

Concerning the width of those lines, the widths of the lines of the .STL sample is generally higher than the one of the CAD sample, this results in their mean width being of 172µm and 184µm, respectively for the CAD sample and the .STL sample. The CAD sample being here more precise, it is supposed the reason is again the less good polishing of the .STL sample that is leading to higher measures on average. One can see that both standard deviation are similar in this case.

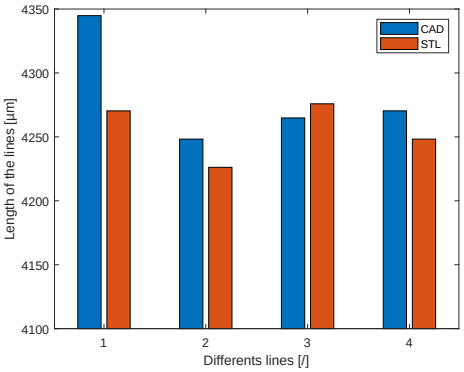

(a) Measured length of the lines supposed to be of length 4250µm

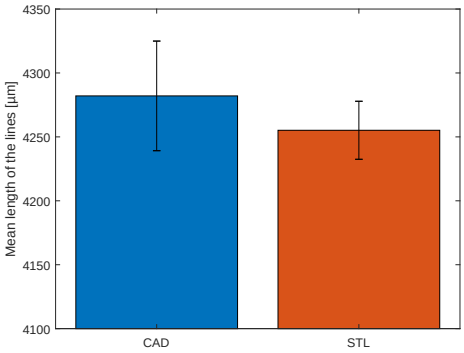

(b) Mean length of the four lines measured

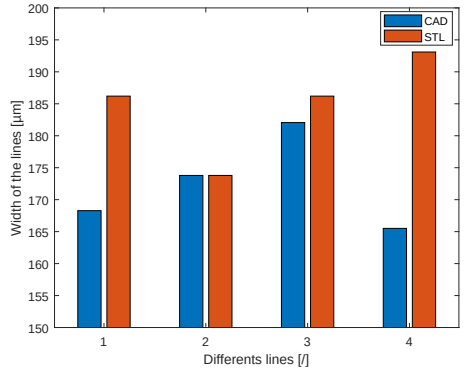

(c) Measured width of the lines supposed to be of width 170µm

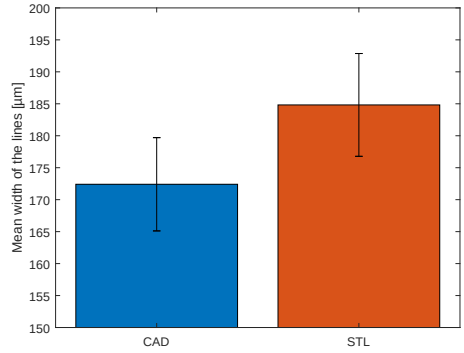

(d) Mean width of the four lines measured

Figure 25: Comparison of the measures of the lengths (a) and widths (b) of the polished horizontal lines supposed to be of 4250µm x 170µm and their mean length (c) and width (d).

FIGURE 26 shows the bargraphs representing the lengths and the widths of the lines on the right of FIGURE 24 B and D. Their lengths are more or less similar but the lines of the .STL sample are a bit longer. Their respective mean length are 4221µm and 4248µm. The .STL sample is then closer to the designed value of 4250µm than the CAD sample and both standard deviation are similar.

Concerning the width of those lines, the widths of the lines of the .STL sample is higher than the one of the CAD sample for the third and fourth lines, this results in their mean width being of 87µm and 97µm, respectively for the CAD sample and the .STL sample. The CAD sample is the most precise of the two but it is of interest to highlight the error on the designed width for the .STL sample that is of 14%, which is a lot and it can be deducted that the precision is not good for its sets of four lines. The CAD sample being here more precise, it is supposed the reason is again the less good polishing of the .STL sample that is leading to higher measures on average. One can see that both standard deviation are similar in this case.

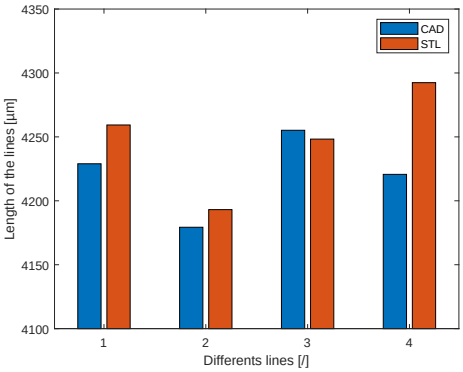

(a) Measured length of the lines supposed to be of length 4250µm

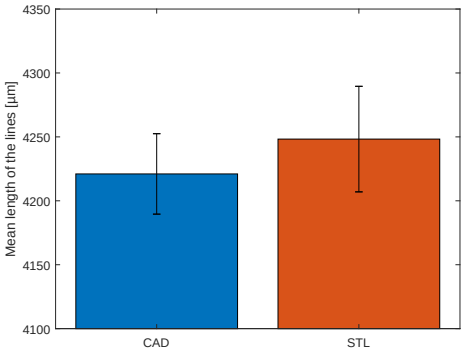

(b) Mean length of the four lines measured

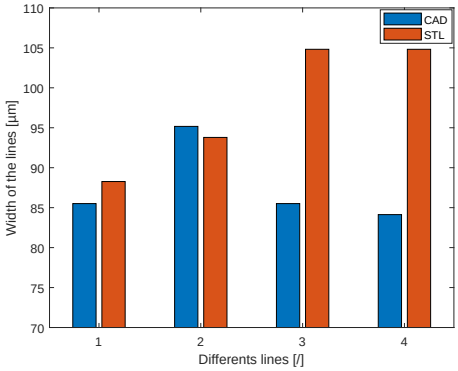

(c) Measured width of the lines supposed to be of width 85µm

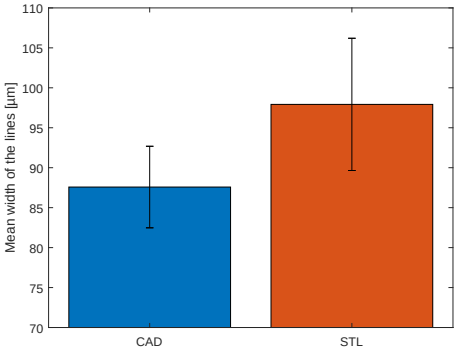

(d) Mean width of the four lines measured

Figure 26: Comparison of the measures of the lengths (a) and widths (b) of the polished horizontal lines supposed to be of 4250µm x 85µm and their mean length (c) and width (d).

Lines perpendicular to printing direction

There are more issue regarding the vertical lines of width 170µm on FIGURE 27 A : first on the pixel map, the two vertical lines of the right exhibit lines of support along both sides, there are three "lines" of holes in between the actual features of approximately the length of the features and there is one line of hole along the third vertical lines starting from the right. The third and fourth vertical lines are of correct dimensions but the last two on the right are of smaller width than 170µm (there are of width 127.5µm, e.g. 3 pixels). The result on the polished sample, visible on FIGURE 27 B is that the first, second and third lines are much wider than they should be even if they are very well drawn. The first two are wider because of the lines of support on their side and the third one is wider because of the "hole-line" along its right side. The fourth vertical line is of correct dimension but exhibit a stronger staircase effect, is continuous but is not as straight as it should be.

On FIGURE 27 C and D, one can see the four vertical lines of width 170µm on the pixelmap and its result. Defects are still present on FIGURE 27 C, the first and fourth lines are of correct width without defect but the second and third lines exhibit a line of support on their right side. There is also a hole/line in between the two. The result on FIGURE 27 D are four identical lines. Neither the defect on the right of the second and third line is apparent or induce a change in the printed sample, neither the hole/line in between the two is present. The hole is completely filled, supposedly because the width of this hole is too thin and it was filled by the droplets of VW+ while printing. The lines are exhibiting a strong staircase effect on both sides due to the printing direction perpendicular to the orientation of the vertical lines.

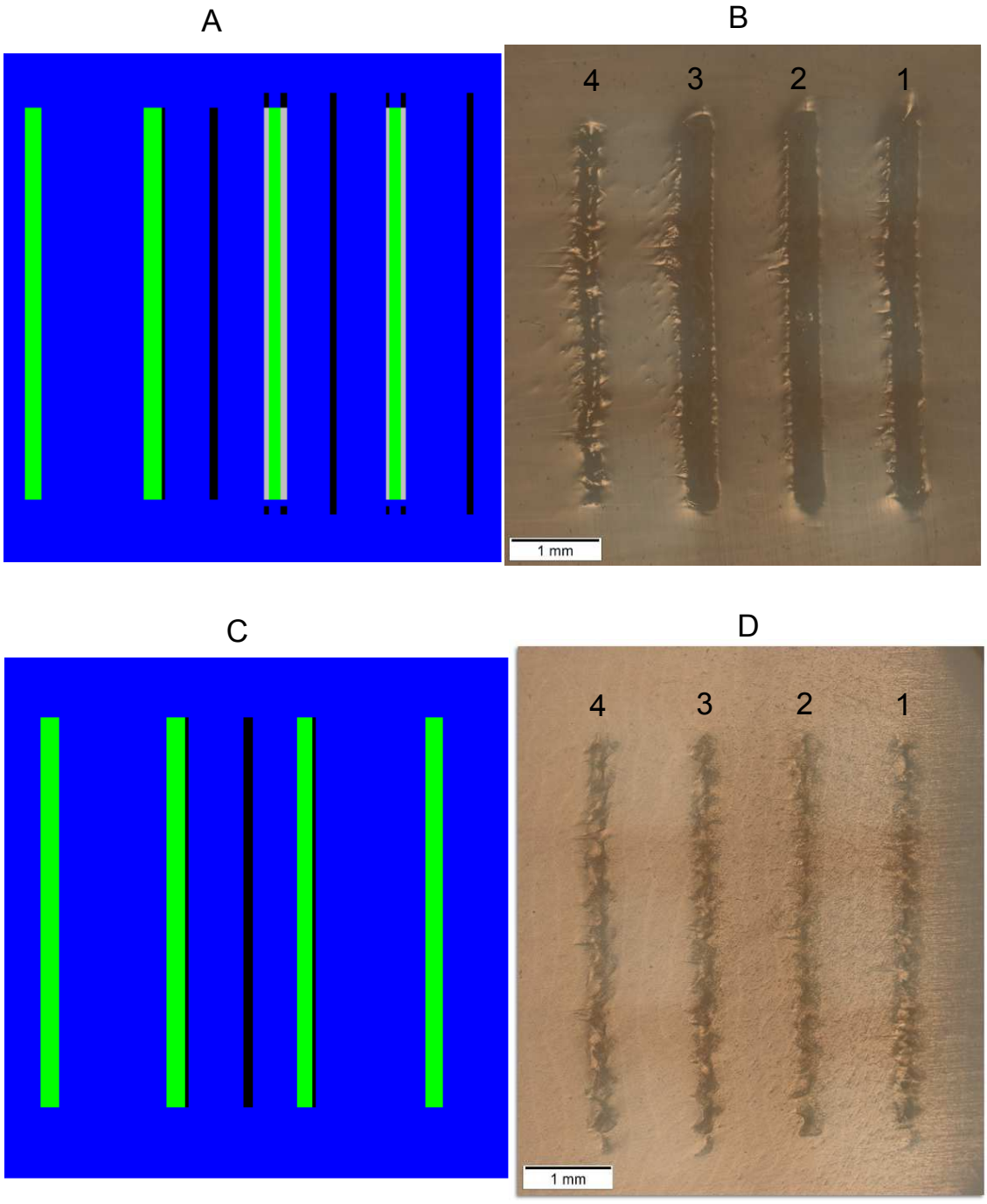

Figure 27: Representation of the vertical lines of width 170µm for : A, the pixel map of the CAD sample; B, the polished CAD sample; C, the pixel map of the .STL sample; D, the polished .STL sample.

FIGURE 28 shows the bargraphs representing the lengths and the widths of the lines on the right of FIGURE 27 B and D. Their lengths are more or less similar but the lines of the .STL sample are generally a bit longer. Their respective mean length are 4237µm and 4252µm. The .STL sample is then closer to the designed value of 4250µm than the CAD sample and the standard deviation of the .STL sample is a bit smaller.

Concerning the width of those lines, one can see that the width of the first, second and third

lines of the CAD sample are much bigger than the one of the .STL sample and the designed width of 170µm. The mean width is 312µm for the CAD sample and 177µm for the .STL sample. The big variation of width in the lines of the CAD sample results in the average width presenting the bigger standard deviation of the two samples.

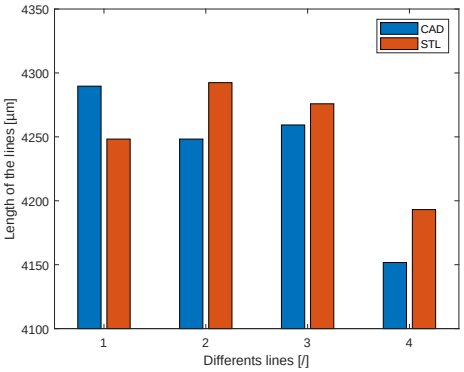

(a) Measured length of the lines supposed to be of length 4250µm

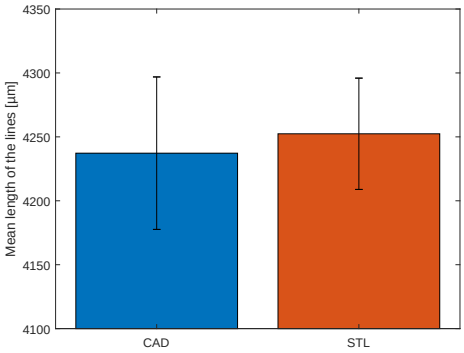

(b) Mean length of the four lines measured

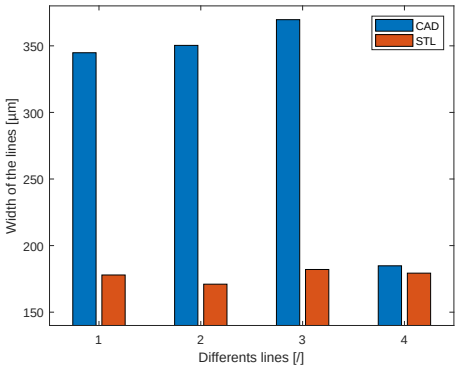

(c) Measured width of the lines supposed to be of width 170µm

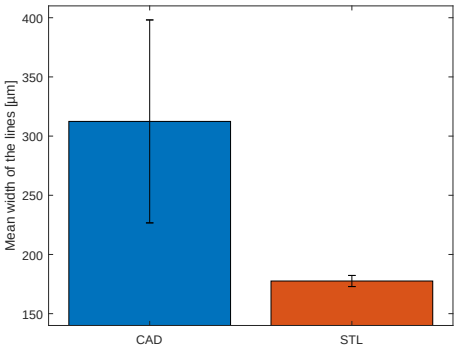

(d) Mean width of the four lines measured

Figure 28: Comparison of the measures of the lengths (a) and widths (b) of the polished vertical lines supposed to be of 4250µm x 170µm and their mean length (c) and width (d).

For the small vertical lines of width 42.5µm and 85µm, the results are good : all the thinnest lines are of correct dimensions on the pixel map (1 pixel wide) on FIGURE 29 A and the lines of width 85µm are all correct (2 pixels wide) except the second one starting from the right, which is thinner (1 pixel wide) than it should be. However, the result on the polished sample is that all lines respect the initial CAD geometry, even the second one from the right whose pixel map was indicating a width of 1 pixel. On FIGURE 29 B its width is similar to the other lines which pixel map was of width 2 pixels. The pixel map from *ObjetStudio* is showing here an element in the display of the bitmap file that seems to not influence the result on the sample.

Both groups of lines from both samples exhibit a strong staircase effect as the width is close to the maximal resolution of the printer and the four lines of width 42.5µm are so thin that the droplets of TB+ are actually mixed within the VW+ surrounding them resulting in a line which can not be considered as made of TB+ only (or even mainly).

FIGURE 29 C shows the pixel map for the four vertical lines of width 42.5µm and 85µm of the .STL sample. One can see that the four vertical lines of width 42.5µm exhibit no defects and are of correct width of 1 pixel. Three of the four vertical lines designed to have a width of 85µm are

correct on the pixel map, they are 2 pixels wide, but the fourth one, which is in the middle of the image, exhibits defects : it is 1 pixel wide only, has a line of support material on its left side and holes at the extremities of this line of support. The printed results, seen on FIGURE 29 D are two groups of lines with the same characteristics : no continuity in the TB+ material meaning they can not be considered lines but aligned packs of TB+. the packs of the four lines supposed to be of width 85µm are wider and bigger than the one of the lines supposed to be 42.5µm. It appears also that the defects present on the pixels map do not influence or do not produce a result different than the three other vertical lines of width 85µm.

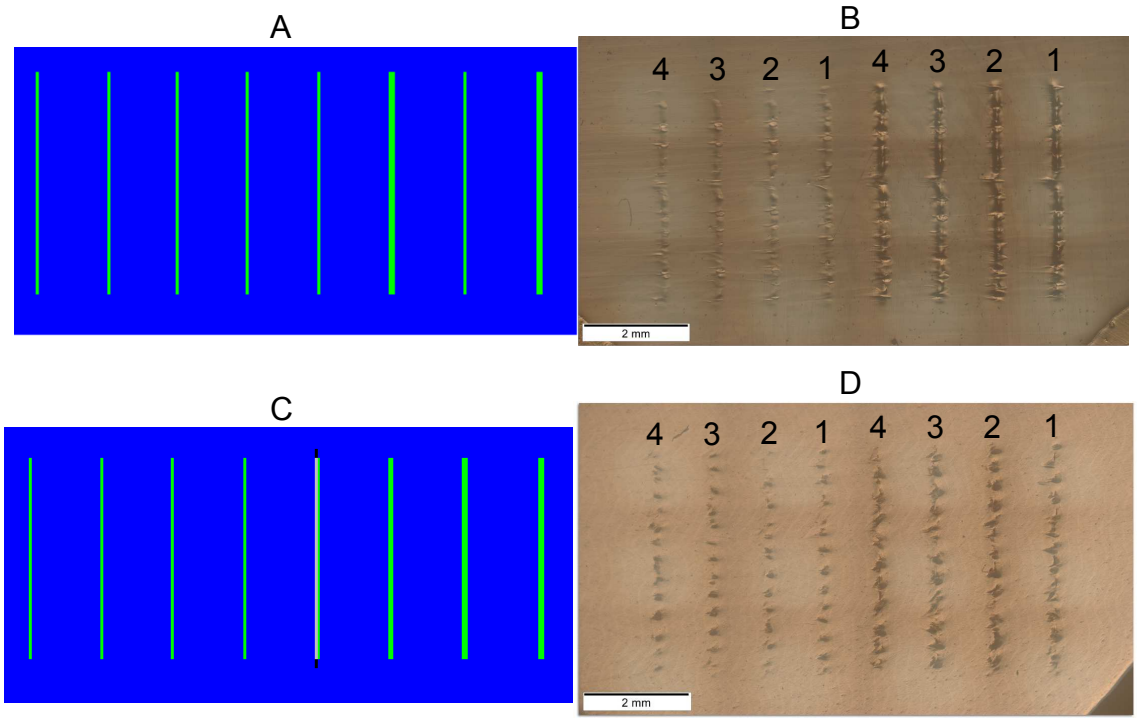

Figure 29: Representation of the vertical lines of width 42.5µm (on the left) and 85µm (on the right) for : A, the pixel map of the CAD sample; B, the polished CAD sample; C, the pixel map of the .STL sample; D, the polished .STL sample.

One can see on FIGURE 30, the bargraphs representing the lengths and the widths of the lines on the right of FIGURE 29 B and D. The lengths of the lines of both samples are more or less similar. Their respective mean length are 4241µm and 4237µm. The CAD sample is in this case closer to the designed value of 4250µm than the .STL sample, but they both present a correct precision, and presents a smaller standard deviation also.

Concerning the width of those lines, the .STL exhibits wider lines in all cases. The mean widths are 89µm for the CAD sample and 98µm for the .STL sample. The CAD sample is then closer to the designed width of 85µm, with an error of less than 5%, but the average error of the .STL sample is of 15%, which is quite important and it can be deducted that the precision is not good for its sets of four lines. This lack of precision in the measured width is supposed to come from the difference of polishing. Finally both standard deviation are similar.

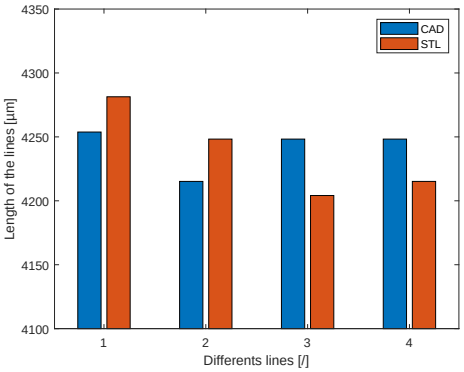

(a) Measured length of the lines supposed to be of length 4250µm

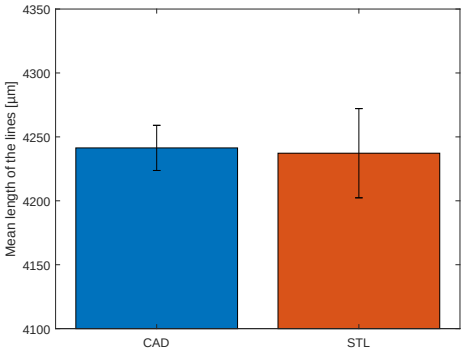

(b) Mean length of the four lines measured

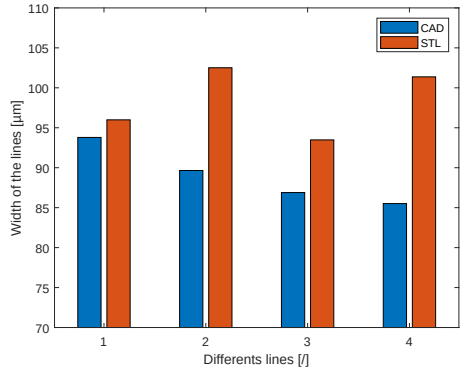

(c) Measured width of the lines supposed to be of width 85µm

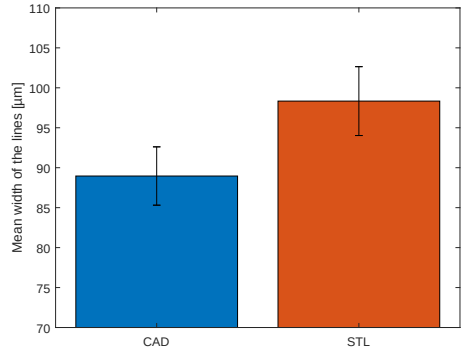

(d) Mean width of the four lines measured

Figure 30: Comparison of the measures of the lengths (a) and widths (b) of the polished vertical lines supposed to be of 4250µm x 85µm and their mean length (c) and width (d).

FIGURE 31 shows the bargraphs representing the lengths of the lines on the left of FIGURE 29 B and D only and not the width of those lines as it was not possible to measure surely a width of TB+ because of the blurred aspect of the TB+ inclusion inside the VW+ matrix around. The lines of the CAD sample are generally longer. Their respective mean length are 4184µm and 4115µm. The CAD sample is in this case closer to the designed value of 4250µm than the .STL sample, but they are both are shorter due to the fact that the lines are not continuous and so there was a loss of length due to a non-presence of TB+ at one end or the other of the lines. The CAD sample also presents the smallest standard deviation.

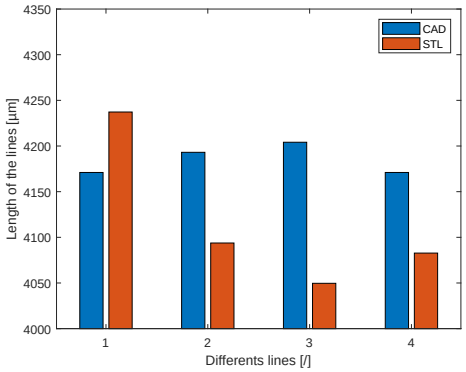

(a) Measured length of the lines supposed to be of length 4250µm

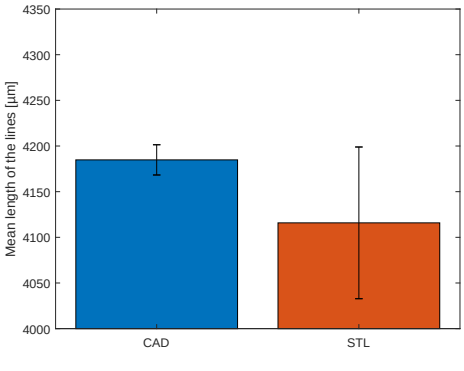

(b) Mean length of the four lines measured

Figure 31: Comparison of the measures of the lengths (a) of the polished vertical lines supposed to be of 4250µm x 42.5µm and their mean length (b).

Squares features

Finally, concerning the squares features, the result is much better are presented here below. On FIGURE 32 most of the squares have the correct dimensions on the pixels map except the second square of the middle column, the third squares of the two column of the right and the second square of the second column starting from the right. Other defects are the smallest square of the column of the right that has disappeared and the small hole instead of it as well as two holes along the right side of the second and third square of the same column. The result are visible on FIGURE 32 B. The biggest squares are the only one clearly respecting the desired geometry even if the third and fourth squares of the column on the right exhibit an extra line on their top right side which is not respecting the desired design. For the others, they are visible but not following the rectangle geometry, the smallest squares are so small that the TB+ was mixed into the VW+ except for the second column from the right which is bigger than it is represented in *ObjetStudio*.

The results for the squares of the .STL sample are visible on FIGURE 32 C and D. On the pixel map, one can see that the first two column of squares (from the left) are respecting the geometry and dimensions, they have correct width of pixels. Defects are in the other three columns, it starts with the second square of the middle column, this square is 5 pixels long instead of 4 pixels; the third square has correct height but is of width 1 pixel and exhibits a hole-line on its left side; the fourth square of this column is made of support material, not TB+ and has a hole-point on its left side. The fourth column has one defect at its third square : it is of correct dimensions but exhibit a line of support material on its right side and hole-points above and below this line. The fifth column exhibits defects at all its squares : the first square is of width 9 pixels instead of 8, the second and third squares are of correct dimensions but have a line of support material on their right with holes of material above and below this line and finally the fourth square is 2 pixels long instead of 1.

FIGURE 32 D shows the result on the printed polished sample : only the elongated shape of the biggest squares tends to respect their designed geometry, the other squares are too small and too blurred to state that they respect their designed geometry. It is even worst for the smallest squares which can not even be seen except the one of the second and third column.

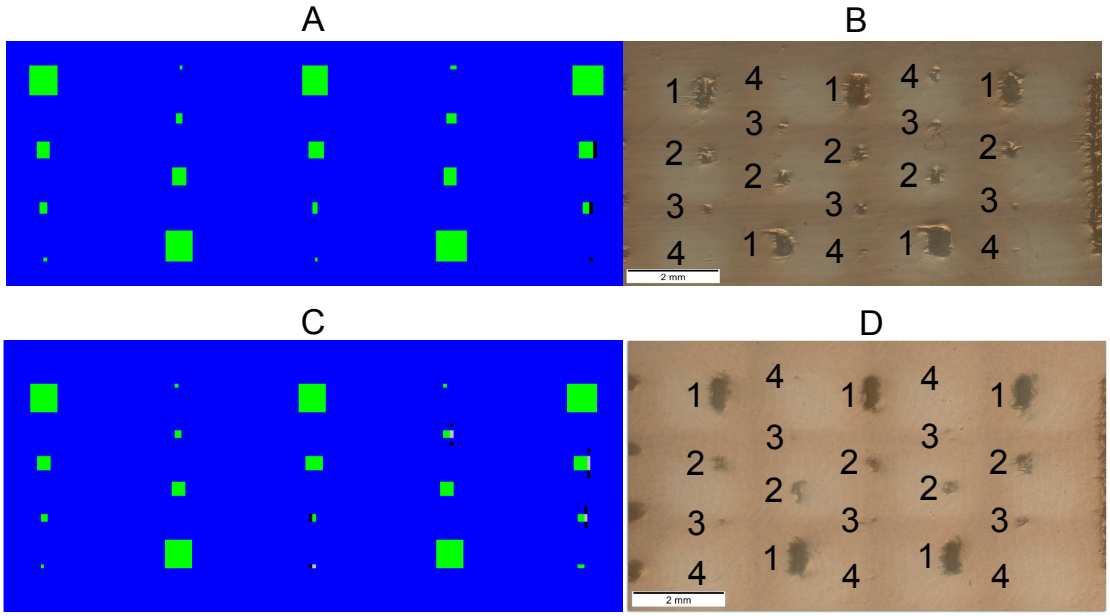

Figure 32: Representation of the squares for : A, the pixel map of the CAD sample; B, the polished CAD sample; C, the pixel map of the .STL sample; D, the polished .STL sample.

One can see on FIGURE 33, the bargraphs representing the lengths and the widths of the squares of FIGURE 32 B and D. The lengths of the squares of the .STL sample are all longer than the one of the CAD sample. Their respective mean length are 629µm and 681µm. The .STL sample is in this case closer to the designed value of 680µm than the CAD sample and it presents a smaller standard deviation also.

Concerning the width of those lines, the squares all have different values but the mean widths are almost similar and are 310µm for the CAD sample and 315µm for the .STL sample. The .STL sample is then closer to the designed width of 340µm, with an error of 7%. Both average widths are below the designed value. The .STL sample is the one presenting the smallest standard deviation of the two.

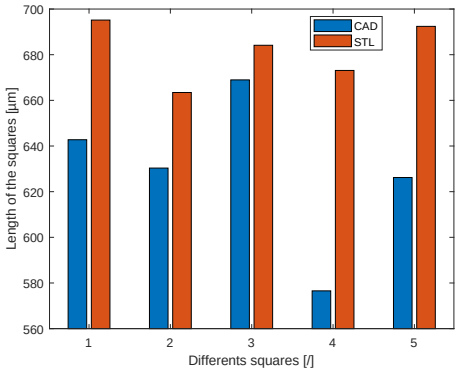

(a) Measured length of the lines supposed to be of length 680µm

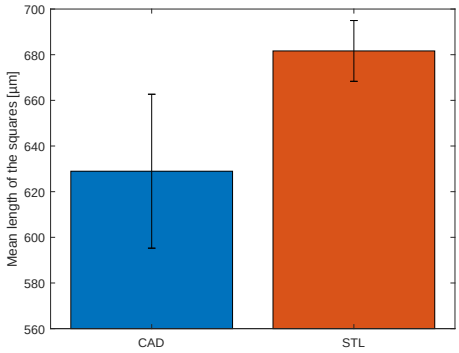

(b) Mean length of the four lines measured

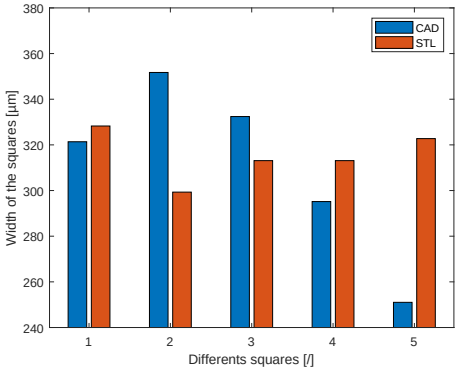

(c) Measured width of the lines supposed to be of width 340µm

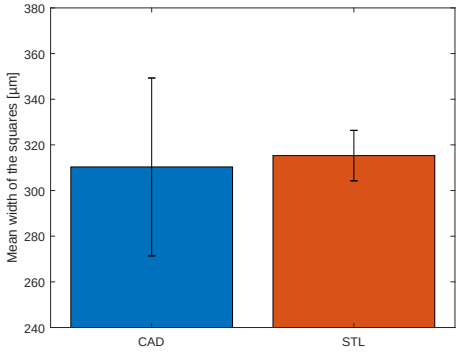

(d) Mean width of the four lines measured

Figure 33: Comparison of the measures of the lengths (a) and widths (b) of the polished squares supposed to be of 680µm x 340µm and their mean length (c) and width (d).

FIGURE 34 shows the bargraphs representing the lengths and the widths of the squares of FIGURE 32 B and D. The lengths of the squares of both samples are all differents. Their respective mean length are 282µm and 305µm. The .STL sample is in this case closer to the designed value of 340µm than the CAD sample but both are quite lower than this value and they present an error of respectively 10% and 17%. Those errors are quite big and it can be considered that the precision on this set of squares is not good. The .STL sample presents the biggest standard deviation of the two.

Concerning the width of those lines, the squares of the .STL are generally wider than those of the CAD sample .The mean widths are 172µm for the CAD sample and 234µm for the .STL sample. The CAD sample is then closer to the designed width of 170µm. The .STL sample presents the biggest error, which is of 37%. Part of this lack of precision is supposed to be due to the difference in the polishing of the two samples.

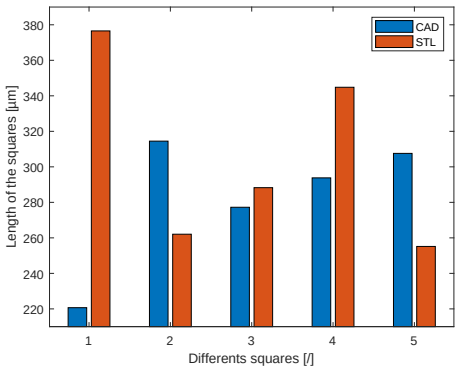

(a) Measured length of the lines supposed to be of length 340µm

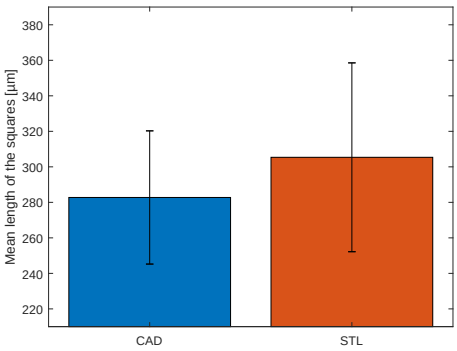

(b) Mean length of the four lines measured

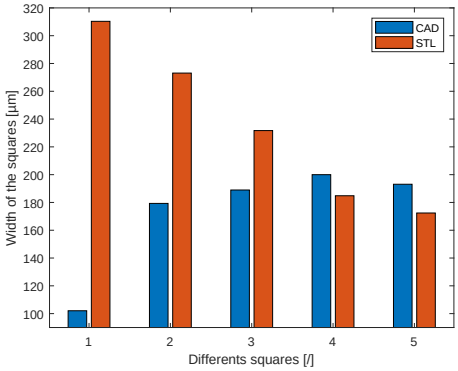

(c) Measured width of the lines supposed to be of width 170µm

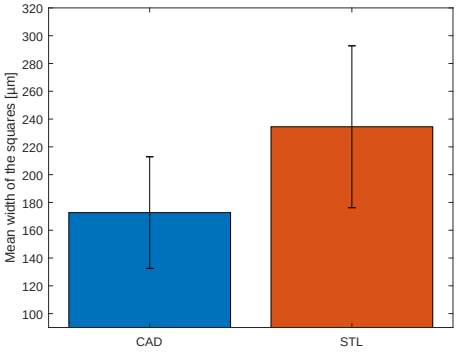

(d) Mean width of the four lines measured

Figure 34: Comparison of the measures of the lengths (a) and widths (b) of the polished squares supposed to be of 340µm x 170µm and their mean length (c) and width (d).

2.3 Conclusion

First, the visual inspection of faces of the multimaterial sample of Grey60 allow to conclude that there is an anisotropy in the geometry of the inclusion of TB+. Anisotropy that is depending on the printing method inherent to the Polyjet technology of the printer and also on the voxel size of the inclusion of TB+. Faces along the xy-plane tends to present elongated inclusion of TB+ resulting from antagonist effects that are the direction of the movement of the printheads and the anisotropic dimensions of the voxel whereas faces along the yz-plane present more elongated inclusion of TB+ that are resulting from the cumulative effects here above presented.

Second, by comparison between the pixel maps and the samples made on IronCAD and directly made in .STL, one can see that :

- Horizontal lines are correctly designed and of correct dimensions on the pixel maps. The printed result is also of very good quality and respect the dimensions of the design.

- There is an improvement in the pixel map concerning the big vertical lines of width 170µm : the one of the .STL sample do not present support material anymore and all the lines are of correct dimension compared to the one of the CAD sample but it still exhibits hole-line. The printed result of the second sample is also better than the first one.

- There is still a defect on the pixel map at one line concerning the vertical lines of medium width (85µm) but at a different position and of a different nature : now there is addition of a line of support and few hole-points instead of a line twice as thin as it should be. However the printed results are both correct.

- There is almost as much defects in the squares in the pixel map but from a different nature as now there is addition of material support that was not there before. For both samples, the geometry of the squares below the dimension 340µm x 170µm do not allow to measure neither the length, neither the width of the squares. They are actually so small that either they are completely mixed in the VW+ matrix around or they are present but not clearly enough to take any measurement.

The polishing of the .STL sample is done only up to 3µm because all attempts to polish it up to 0.05µm led to the features of TB+ being completely filled by the polishing paste without possibility to remove it and then no measurements could be done. This might influence the accuracy of the measurements made on this sample but the general trends of the measures are still catched even with a polishing of 3µm.

The conclusion is that making .STL directly from a matlab code allows to have less great defects on the pixel maps but it do not allow to be completely free of them, there is as much defects in the pixel map of the sample made on IronCAD that the one made on matlab, only the nature and size of the defects change. This means that there is still an advantage to design the .STL files from matlab, which is that the user has total control over the distances, the geometry of the sample and the voxel size as well as the combination ratio of material at the voxel level. Practically speaking, it is also not difficult to take in hand, it might take longer than IronCAD to design piece but that is all.

3 Improving bimaterial attachment with voxel printing

Knowing the limitations of the printer, its resolution and accuracy, it is now possible to play with the material deposition at voxel level in order to try to produce a stronger interface between two materials presenting a high difference of Young modulus than if the interface was just flat. The idea is to play with the dithering pattern at the interface of the two materials in order to improve the resistance to fracture propagation at the interface. To do so, three different design will be investigated and their mode I fracture energy (i.e. under opening) will be computed as well as their pixel map and their broken interface inspected in order to compare them and see which design performs the best.

Plus, such a short transition interface improves the fatigue performances of the pieces as shown by *Dorcas V. Kaweesa et al.* [23]. Their study compared specimens with continuous or stepwise gradients of different lengths of gradients and they showed, between others, that :

- The shorter the material gradient transition lengths are, the better the fatigue performance for multimaterial parts.
- Inserting a functionnally graded materials transition region to the existing designed length of a flexible region improves the fatigue life of a multi- material part.

The analogy with nature in the interest of improving interfaces is the length-scale of the interface in the bone-tendon attachment in the human body. The total length-scale transition from bone to tendon is of approximately 500µm [34] and the load it can withstand is higher than what is actually achievable to manufacture for now. Moreover, this size seems very convenient and of better use for industrial application or biomimetic application than long transition areas as it saves materials and allow the printed part to be more compact.

3.1 Material and Methods

This section consists in a presentation of the designs of the samples, the printing option chosen, the testing procedure followed and the post-processing of the data in order to extract the evolution of crack length and fracture energies of the samples.

3.1.1 Sample design

Three different design strategies are presented : a flat interface which will serve as a reference because it represents the common situation of flat interface between two solids, a vertical gradient interface where the gradient is in the z-axis and a horizontal gradient interface where a scheme of horizontal gradient is repeated along all the interface in the longitudinal axis of the sample.

Reference : flat interface

The flat interface sample follows exactly the design used by *papier de cordisco*, visible on FIGURE 35. The goal of this design is to have a reference to which the results of the gradients interface can be compared. The area in black will be the TB+ material and the two gray part will be the VW+ material. There are two holes in order to mount the sample on hinges to proceed to testing and to allow the free rotation of the sample, as can be seen on FIGURE 40. The drawing is not representative in the proportion as the area of TB+ in the center is bigger than it should be, it is made on purpose for the visibility and understanding of the design. One can see that the crack initiation is made of a staircase of four steps of TB+ on each sides of the interface that link in the center of the drawing at 45mm right starting from the crack opening.

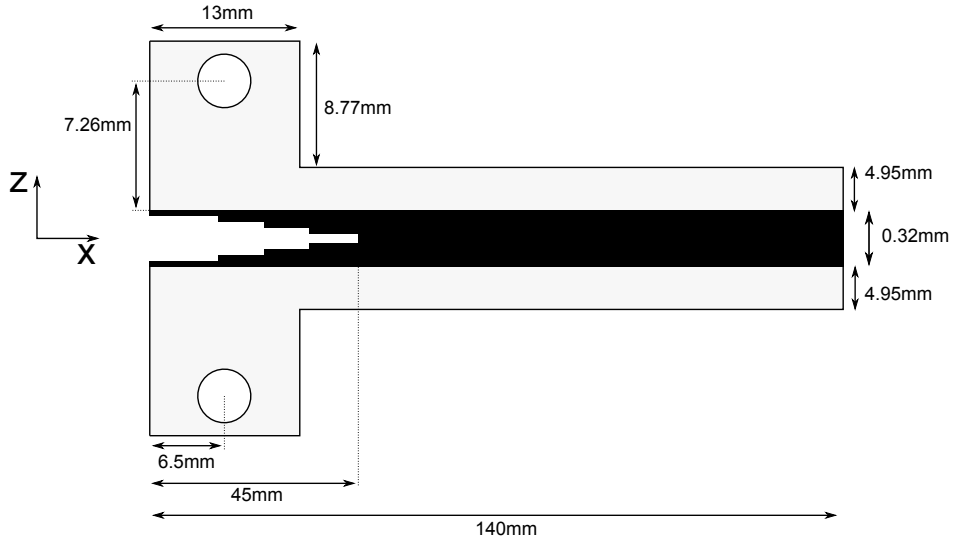

Figure 35: Flat interface design

All the distances are rounded to the closest multiple of the resolution of the direction of the printer in which there are oriented. By recalling that the resolution is of 42.5µm in the x-axis, 85µm in the y-axis and 31.75µm in the z-axis, this gives :

$$\text{x-axis} \begin{cases} 140mm \approx 42.5\text{µm} * 3294 = 139.995mm \\ 45mm \approx 42.5\text{µm} * 1053 = 45.008mm \\ 6.5mm \approx 42.5\text{µm} * 153 = 6.5025mm \\ 13mm \approx 42.5\text{µm} * 306 = 13.005mm \end{cases} \quad \text{z-axis} \begin{cases} 8.77mm \approx 31.75\text{µm} * 276 = 8.763mm \\ 7.26mm \approx 31.75\text{µm} * 229 = 7.2708mm \\ 4.95mm \approx 31.75\text{µm} * 156 = 4.953mm \\ 0.32mm \approx 31.75\text{µm} * 10 = 317.5\text{µm} \end{cases}$$

with a thickness in the y-axis of $10mm \approx 85\text{µm} * 118 = 10.03mm$. All those values are the same for the three different designs.

The radius of the holes are not indicated because as the resolution in the x and z axis are different, the result will not be a hole, but an ellipsoïd. However, this is not a problem as this ellipsoïd will be drilled in order to have an actual hole in which to fix the hinge for the tests. The design of the holes is then used as a reference point which indicates where to drill and it facilitates drilling as the ellipsoïd just needs to be expanded.

For all samples, a Matlab 3D matrix representing the design of the samples is created and then used with the .STL generation code to create an .STL file of the samples using the scales in the three direction as presented here above.

Vertical gradient interface

This design introduces a vertical gradient in the composition of the interface layer. Instead of having a hard transition from VW+ to 10 layers of TB+, there are four layers of intermediate gradient bewteen the two. From the outside to the inside the layers are composed of 20%, 40%, 60% and 80% of TB+ to finish with the two central layers which are 100% composed of TB+. As can be seen on Figure 36, this is implemented by having a repeated pattern of one pixel out of five made of TB+ (the rest is made of VW+) for 20%, two pixels out of five made of TB+ for 40%, three pixels out of five made of TB+ for 60% and 4 pixels out of five made of TB+ for 80% all along their respective line in the x-axis.

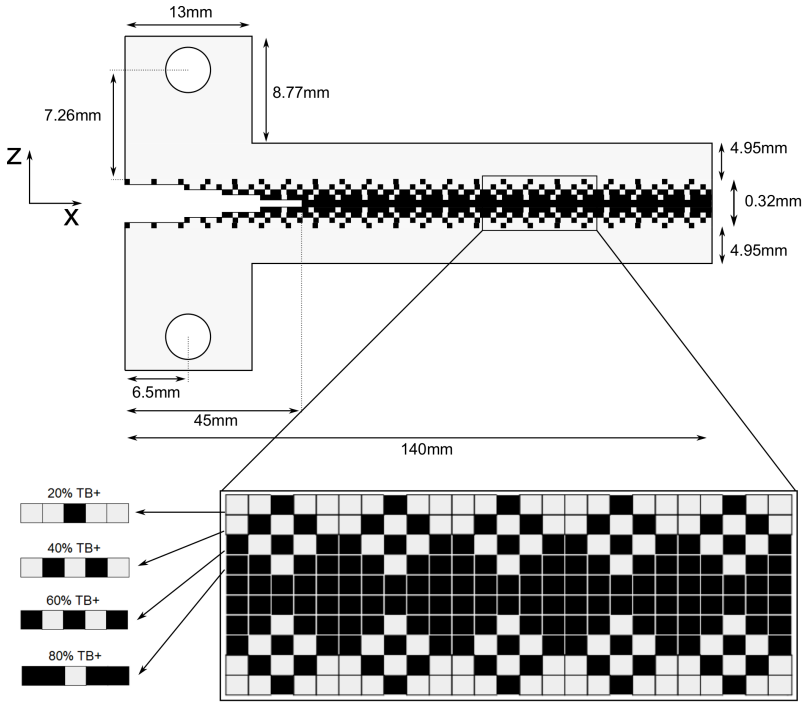

Figure 36: Design of the vertically graded interface

It is expected that this design will require more energy to propagate the crack than the reference one as the interface transition is more smooth and continuous by using the four intermediate gradient layers.

Horizontal gradient interface

This design introduces a horizontal gradient in the composition of the interface layer. It is based on a pattern that is repeated along x until the end of the piece. This pattern is made of six layers in the yz-plane through the x-axis : one layer made fully of TB+, four intermediate layers of respectively 20%, 40%, 60% and 80% of VW+ and a final layer made only of VW. The composition of the four intermediate layers in their pixelised distribution is made exactly as for the previous design. All can be seen on FIGURE 37.

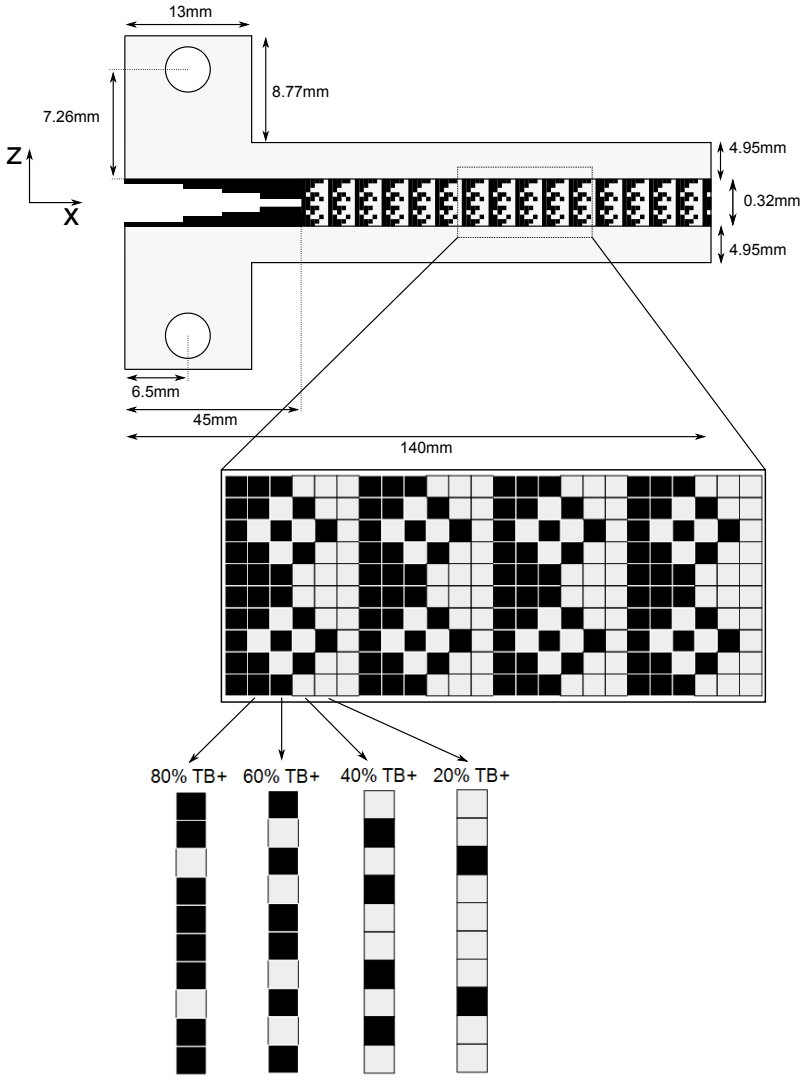

Figure 37: Design of the horizontally graded interface

It is expected that this design will require more energy to propagate the crack than the reference one as every time one layer of VW+ is broken, the crack has to propagate through an increasingly hard material again and again. An analogy can be done with cutting wood by attacking perpendicularly the fibers of the wood with an axe, it takes much more time, energy and effort than to crack the wood by following the direction of its fibers.

3.1.2 Sample manufacturing

All samples are designed to be printed with their longitidinal axis along x-axis of the building tray and their interface being composed of layers in the xy-plane stacked through the z-axis, as can be seen on FIGURE 38. The samples are printed using the "matte" option which surrounds them in support material. This option was chosen in order to have the same surface roughness on all faces of the samples.

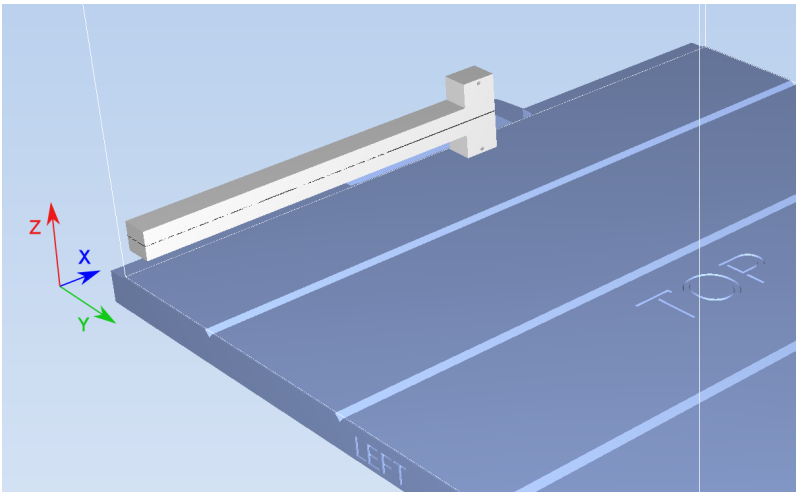

Figure 38: Orientation of the samples on the building tray

It is expected this will be a weak printing configuration because the inter-layer miscibility is less effective along z than along droplets in the same xy-plane due to the printing method (see previous section for explanation) and so delamination is supposed to happen more easily between layers stacked along z. Those gradient are developped here below.

3.1.3 Sample testing

All tests have been conducted on samples 1 day after their printing to have valid results to compare : to avoïd the variability of the material properties during the first 24h [30] and to avoïd decrease of mechanical properties such as shown by Lindsey B. Bass et al. [22].

The MTS machine

The device used for the testing and recording of the data in the second part is a MTS Criterion™model 43 coupled with a MTS - Video Extensometer from MTS for video recording, visible on Figure 39 with its camera and setup ready to operate. The sample mounted on the MTS machine is shown on Figure 40 from two different points of view.

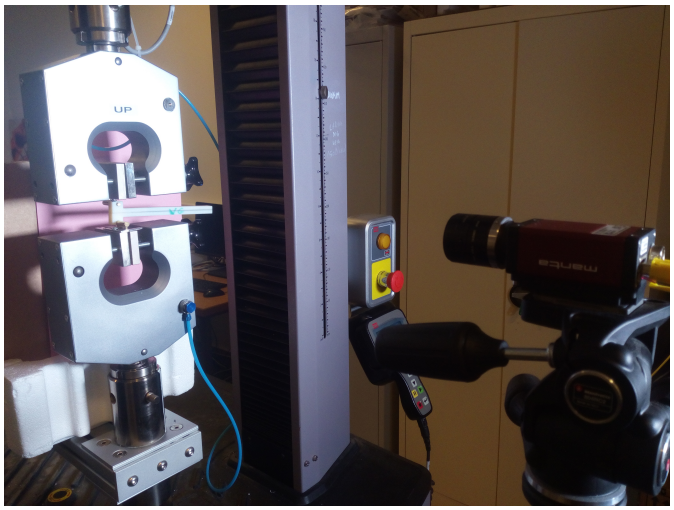

Figure 39: MTS machine

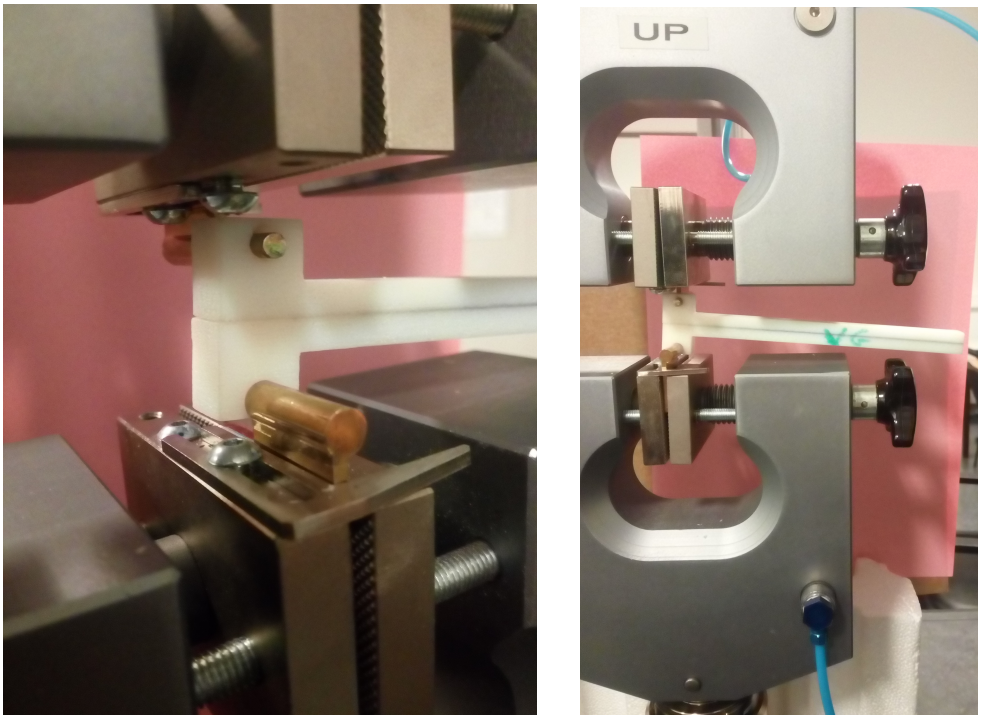

(a) Close look at the hinges holding the sample

(b) Frontal look of the setup

Figure 40: Close and frontal look at the setup

Image processing

The crack length is extracted from the video records of the tests using the image processing software *ImageJ* and *Matlab*. The procedure of the post-processing of the images is shown on FIGURE 41. First, the images, i.e. the frames, of each video record is binarised using the software *ImageJ* in order to have the interface in white and the beams of VW+ in black. Then using *Matlab*, the image is cropped in order to obtain only the area of interest which is the interface. As one can see, when the crack is opening, the interfaces opens and the area of white pixels increases. Based on this, a threshold width of interface (or white pixels) for each position along the x-axis, called t_x, is determined for each video record. It is the width of white pixels for each position of the interface at the initial frame. The detection of the propagation of the crack is done when the current width of white pixels, called W_x, is greater than its threshold value t_x, i.e. when $W_x > t_x$. The position x at which this condition is encountered is an indication of the crack length. The crack length is calculated by

$$L_{crack}(i) = 140 - L(i), \tag{1}$$

where $L_{crack}(i)$ [mm] is the crack length of the ith frame and $L(i)$ [mm] is the length of remaining intact interface.

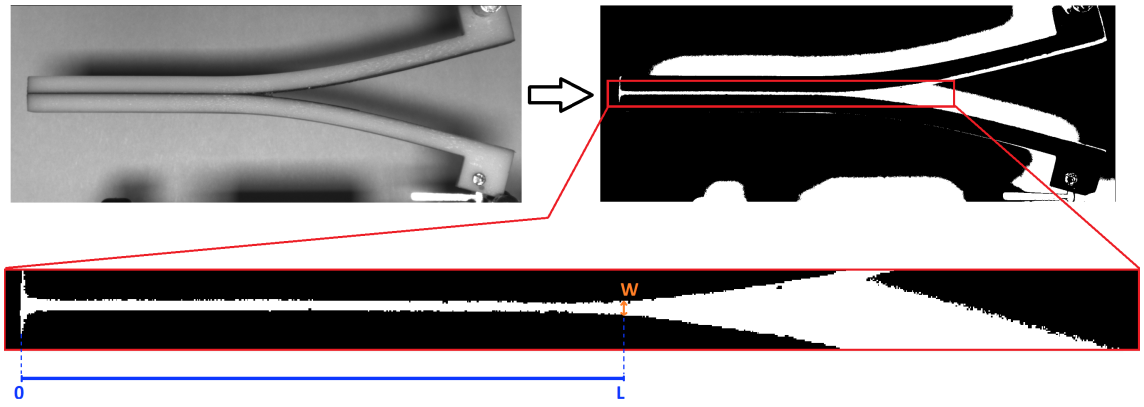

Figure 41: Steps of the image processing in order to obtain the evolution of the crack length.

Fracture energy

The mode I tests are performed on the samples at a displacement rate of 3.5mm/min using the MTS machine. Mode I fracture energy is calculated using corrected beam theory (CBT) [32], [18], [19] :

$$G_{Ic} = \frac{3P\delta}{2B(L_{crack} + crack_{corrected})} . \frac{F}{N}$$

where G_{Ic} is the mode I fracture energy, P is the load [N], δ is the applied displacement [mm], B is the width of the specimen [mm], L_{crack} is the crack length [mm], $crack_{corrected}$ is a "corrected" crack length [mm], F is the large displacement correction [-] and N the load correction [-]. Those last two parameters are calculated by :

$$F = 1 - \frac{3}{10}\left(\frac{\delta}{L_{crack}}\right)^2 - \frac{3}{2}\left(\frac{\delta l_1}{L_{crack}^2}\right) \tag{2}$$

$$N = 1 - \left(\frac{l_2}{L_{crack}}\right)^3 - \frac{9}{8}\left[1 - \left(\frac{l_2}{L_{crack}}\right)^2\right]\frac{\delta l_1}{L_{crack}^2} - \frac{9}{35}\left(\frac{\delta}{L_{crack}}\right)^2 \tag{3}$$

where $l_1 = 7.26$mm and $l_2 = 6.5$mm in FIGURE 35. Also the "corrected" crack length $crack_{corrected}$ is the negative of the abscissa intercept for an extrapolation of a plot of the cube root of the corrected compliance, $\left(\frac{C}{N}\right)^{1/3}$ depending on the crack length L_{crack}. By so, it can also be found analytically by understanding that $L_{crack} = crack_{corrected}$ when $\left(\frac{C}{N}\right)^{1/3} = 0$ which can be translated as

$$\lim_{L_{crack} \to crack_{corrected}} \frac{1}{N(L_{crack})} \to \infty \tag{4}$$

and further by $N(crack_{corrected}) = 0$, which is then an equation of degree 4 in $crack_{corrected}$ to resolve.

Those three factors : the large displacement correction, F, the load correction, N, and the "corrected" crack length, $crack_{corrected}$, are factors accounting for the compliance of the beams while the test is running and correcting the fracture energies computed in consequences.

3.2 Results & Discussion

3.2.1 Pixel map of the graded samples

The pixel maps of the successsive layers at the level of the interface between VW+ and TB+ of the horizontal and vertical gradient where extracted from ObjetStudio and reconstructed using

ImageJ in order to obtain the pixel map in the xz-plane of the interface. Those pixel map will be compared to the designed interface in the .STL to see if it was reproduced correctly.

First, the pixel map of the vertical gradient sample is shown on FIGURE 42. As one can see, the correct design, as shown on FIGURE 36 is present on this pixel map but there are also defects. The defects are a set of repeating uncorrectly distributed pixels supposed to account for a precise intermediate gradient of 20%, 40%, 60% or 80%. Those defects are repeating more or less every 3.5mm all along the sample and they are almost all identical in the scheme that they draw.

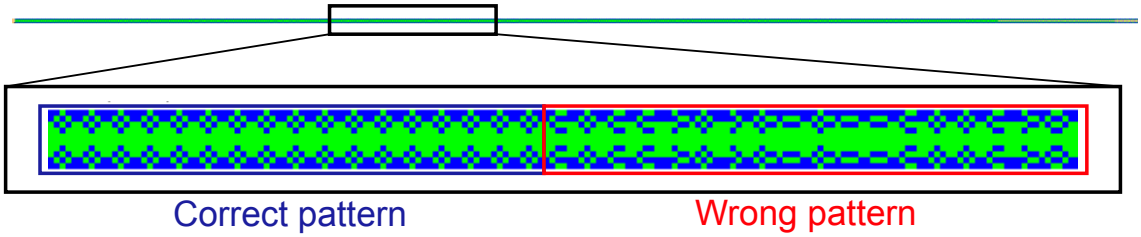

Figure 42: Bitmap of the vertical gradient sample with highlights on the correct and wrong pattern.

The analysis of the distribution of the VW+ pixels and the TB+ pixels of its pixel map is performed in order to verify that the gradient designed for each layers is respected. The results of this analysis is available on TABLE 4. One can see that the average VF of each layer of different gradient respect very well (less than 1% error) the gradient designed for each layer. Even though there is a repeated pack of defects along the sample, the gradient of each layer is on the average respected, which allow to say that the printed sample is valid in its specific design of vertical gradient.

Designed VF of TB+	**Average VF TB+**
Layers of 100% TB+	100% TB+
Layers of 80% TB+	79.82% TB+
Layers of 60% TB+	60.08% TB+
Layers of 40% TB+	39.91% TB+
Layers of 20% TB+	20.17% TB+

Table 4: Comparison between the overall designed VF of TB+ and the one of all layers of the pixel map of the sample

Second, the pixel map of the horizontal gradient sample is shown on FIGURE 43. The same observation can be done regarding the repeated scheme of the defects along the axis of the sample.

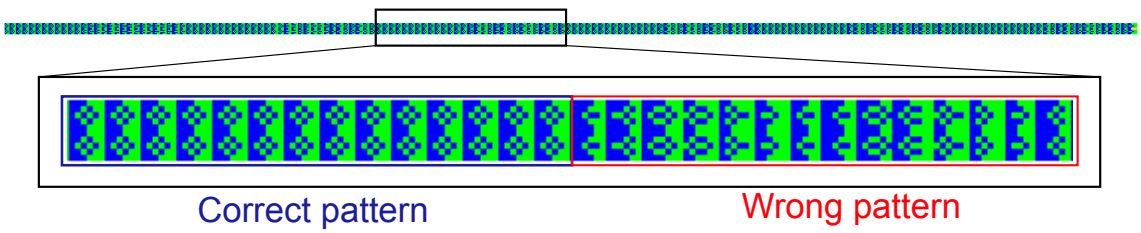

Figure 43: Bitmap of the horizontall gradient sample with highlights on the correct and wrong pattern.

The analysis of the distribution of the VW+ pixels and the TB+ pixels of its pixel map is also performed but this time on each of the layers along the yz-plane in order to verify that the sum

of the layers of supposedly same gradient is respecting the designed gradient. The result of the verification are shown on Table 5. One can see that the percentages of TB+ are not respected at all and that they are almost independant from their designed value to stay approximately around 50%. However, they are still ordered with the highest percentage of TB+ being for the layers designed to have 100% of TB+ and the least percentage of TB+ being for the layers designed to have 0% of TB+.

It seems that the defects in the pixel map are completely falsing the results of the average VF for each type of layer. The defects are repeating along the sample in such a way that the design pattern is shifted along the x-axis resulting in this average value of 50% for all the different layers. The pixel map is alternating between packs of correct design ,and by so correct gradients, and between packs of defects that are not following at all the desired pattern.

Designed VF of TB+	**Average VF TB+**
Layers of 100% TB+	52.94% TB+
Layers of 80% TB+	52.13% TB+
Layers of 60% TB+	50.37% TB+
Layers of 40% TB+	50.1% TB+
Layers of 20% TB+	47% TB+
Layers of 0% TB+	46.71% TB+

Table 5: Comparison between the overall designed VF of TB+ and the one of all layers of the pixel map of the sample

It is unclear why there is a regular repeating of defects inside the pixel map of the samples. Such an error can not come from the .STL as there are not presenting this defects. The intuitive explanation of such a regularly repeated defects would be that the scale of the longitudinal axis used to produce the .STL file is not exactly the one achievable by the printer but it can not be this explanation as the scale used is exactly the one of the printer's specification that produced good result in the previous part and because the samples are exactly of length 140mm.

3.2.2 Crack length & fracture energies

At first, one can see the load-displacement curve for the three samples for a displacement rate of 3.5mm/min on Figure 44. The vertical gradient is completely breaking the first one at a displacement of 56mm and exhibits a peak of load before the initial breaking at $\approx$ 35N. The second one is the flat interface sample which has a peak load of 44N and is completely broken for a displacement of 66mm. The horizontal gradient is exhibiting a peak of load of 52N and is completely broken for a displacement of $\approx$ 95mm. The three curves all exhibit the same trend, but if the vertical gradient and the flat interface present relatively smooth decreasing load curve after the peak, the horizontal gradient one exhibits periodically small increases of load but still in the decreasing part of the load curve. A specific investigation will be conducted in the next section.

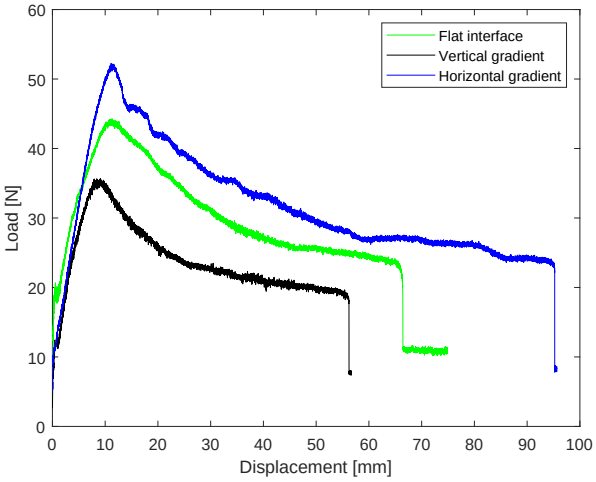

Figure 44: Load-displacement curve for the three samples at a displacement rate of 3.5mm/min

Surprisingly, the vertical gradient sample is breaking more easily than the flat interface one which is at the counter intuition of what the author expected. A closer look at the interfaces of the sample in order to understand better why will be done later.

FIGURE 45 represents the evolution of the crack length depending on time. One can see that the curves are more or less identical until 50s, because until then it is only the crack initiation that is seen opening to 45mm and from there the curves diverge. The flat interface gradient sample do not reach a crack value of 140mm but of $\simeq$ 138mm because ,even while being completely broken, the end edges of the sample where still holding together due to the remaining TB+ at the interface, as can be seen on FIGURE 46. This position is considered as a total breaking position as the sample could not withstand any more load.

One can see that the three samples are not continuoulsy breaking until 140mm, instead they are all breaking suddenly from $\simeq$ 126mm to 140mm. This sudden break is explained by the energy stored in the beams that are bending while the test is running and when the interface is not strong enough to withstand this bending energy anymore, it is released by a sudden break. Images of the bending beams can be seen on FIGURE 47.

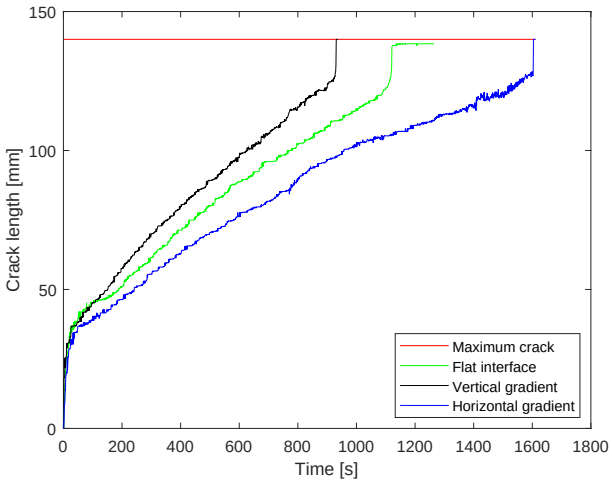

Figure 45: Crack length evolution with time at a displacement rate of 3.5mm/min

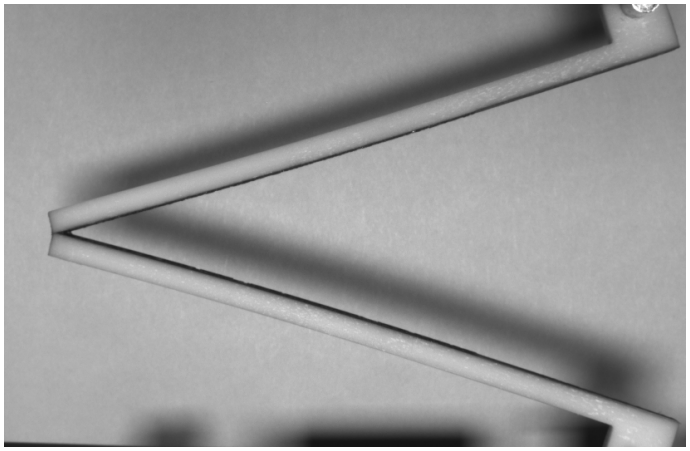

Figure 46: End position of the flat interface sample

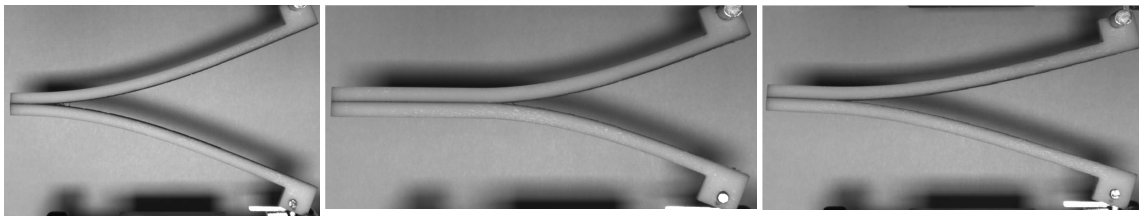

Figure 47: Images of, respectively, the flat interface (A), the horizontal gradient (B) and the vertical gradient sample (C) where the bending of the beam is visible.

FIGURE 48, one can see the graphs of the cube root of the corrected compliance depending on the crack length for the three samples as well as a linear interpolation for the horizontal gradient sample and for the flat interface one, the linear interpolation for the vertical gradient is not shown as it would overload the graph and reduce the visibility. The corrected crack length â computed

are respectively -4.2, -3.9 and -3.7 for the vertical gradient, the flat interface and the horizontal gradient. Those values are in quite well agreement with the data acquired for the different samples as one can see on the graph. They tend to validat the use of this corrected beam theory.

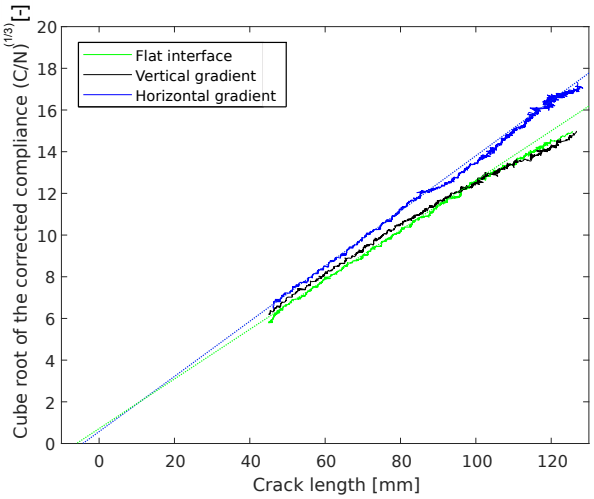

Figure 48: Cube root of the corrected compliance depending on the crack length

Finally the fracture energies can be compared on FIGURE 49. The interesting part of the graph is the one after 45mm, all before is not corresponding to a fracture energy because it is in the length of the crack initiation. One can see that while the flat interface and the vertical gradient samples exhibits a smoothened almost constant fracture energy curve after 45mm, the one of the horizontal gradient is much more serrated.

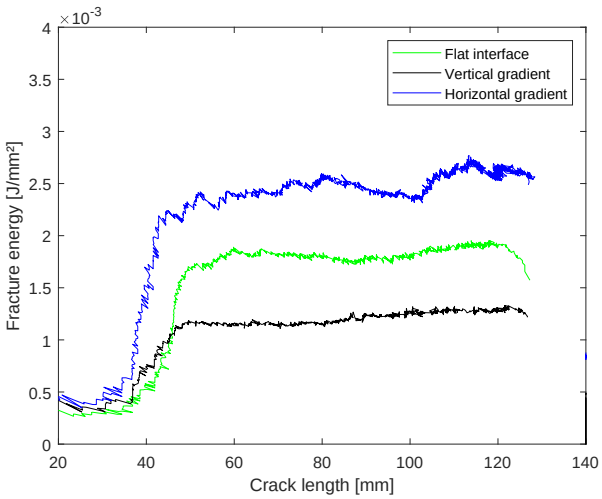

Figure 49: Fracture energies of the samples

Surprisingly, the flat interface sample performs better in all matters than the vertical gradient one, which is at the counter intuition of the author. It breaks faster with less load which is translated by this sample having the lowest fracture energy, twice less than the horizontal gradient one for example.

3.2.3 Post-failure analysis

In order to better understand the surprisingly bad results of the vertical gradient sample, the interfaces of the three samples are compared to see how the breaking is characterised. The interfaces of the sample are shown on FIGURE 50. One can see that each interface of the flat interface sample and of the horizontal gradient one are characterised by a mosaic pattern complementary of the other one, such as showed by [32], and which clearly shows that the crack is propagating at the interface bewteen VW+ and TB+. On the interfaces of the horizontal gradient sample, there are regularly presence of pack of wide lines perpendicular to the longitudinal axis of the sample, whereas it would be expected that either all perpendicular lines of the design are seen, such as on FIGURE 37, either none of them are seen. The closer investigation regarding this feature is done at the end of this section.

Finally, the interfaces of the vertical gradient can be observed. Here, both sides are uniformly gray with no particular distinguishable pattern or features. It seems that crack propagated not at the interfaces between the gradient of materials but completely inside the TB+ layer. This would explain why the vertical gradient sample is weaker than the flat interface one : the crack is propagating inside the TB+ which a very soft material and not at the interface between TB+ and the intermediate gradients.

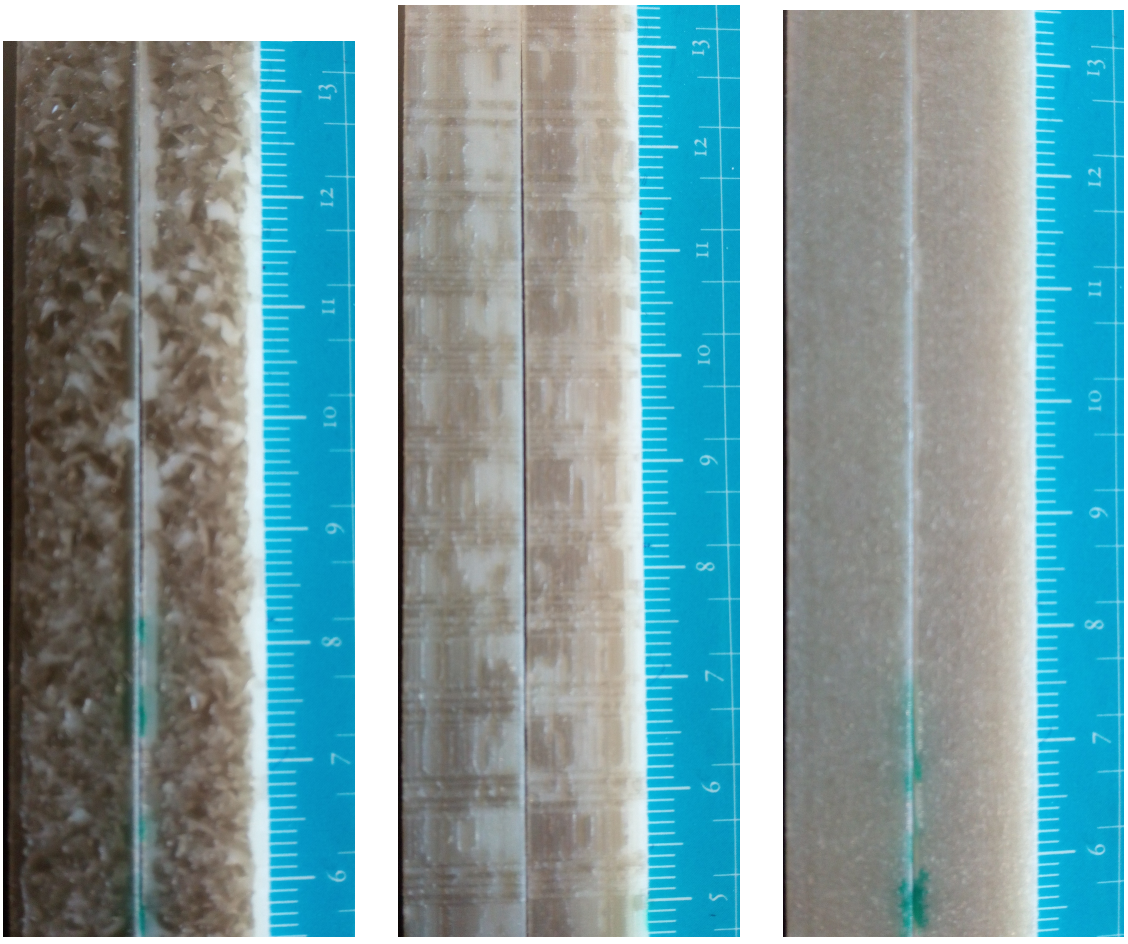

(a) Flat interface sample (b) Horizontal gradient sample (c) Vertical gradient sample

Figure 50: Images of the interfaces of the three samples.

In order to investigate more about the interface of the horizontal gradient sample, a comparison between the pixel map of the interface and the broken interface itself is done on FIGURE 51. One

can see that the defects in the pixel map are actually corresponding to the larger lines perpendicular to the longitudinal axis of the sample. The defects in the pixel map are producing wider lines than the one it is supposed to do when it is following the correct design and that can be seen on FIGURE 52. Those wider lines, or defects, are then explaining the small repeated increases of load in the load-displacement curve of the horizontal gradient on FIGURE 44.

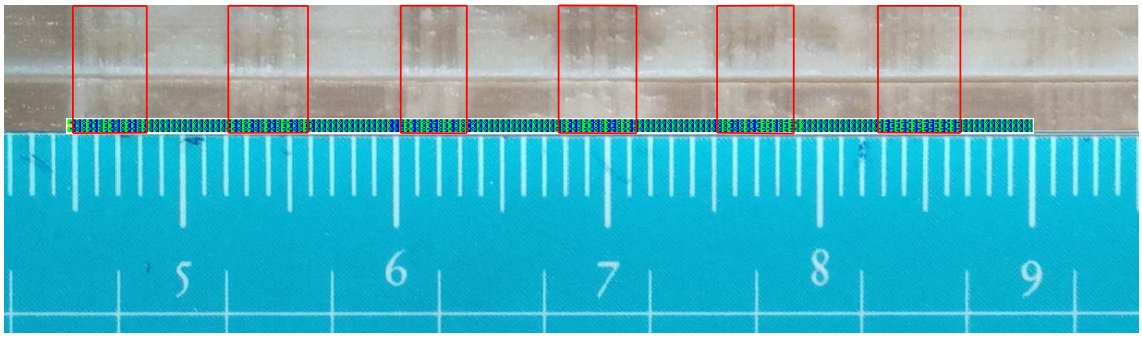

Figure 51: Comparison between the bitmap and the interface of the horizontal gradient for the first 45mm after the crack initiation.

On FIGURE 52, one can see, between the packs of defs, the small lines perpendicular to the longitudinal axis of the sample corresponding to the correct design of the interface.

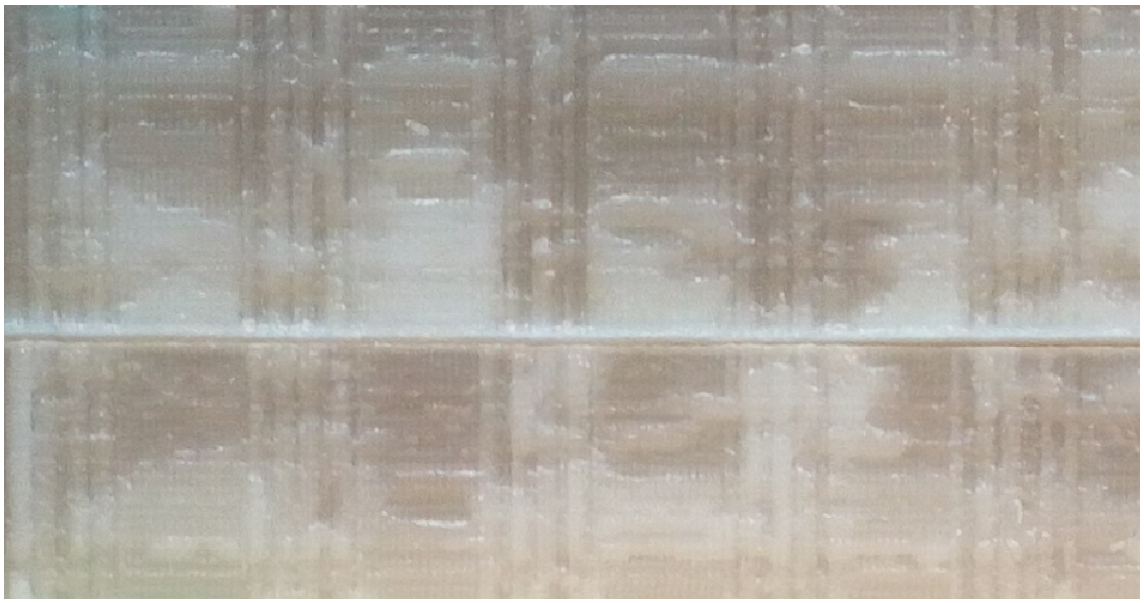

Figure 52: Image of a closer look at the interface corresponding the first 45mm after the crack initiation.

Influence of the displacement rate

The influence of the displacement rate on the mode I fracture energy has been investigated by *Vu and al.* [32]. They measured that fracture energy is highly displacement rate dependent as it increases for higher displacement rate. They tested three different rates : 0.01mm/min, 0.1mm/min and 1mm/min and the increase in fracture energy is up to 600% for the highest rate compare to the lowest one.

It is interesting to note that they also compared the fracture surfaces and for all three of them the crack had propagate at both interfaces, breaking by small patches but never inside the soft material. It is a clear illustration that the weak point is the interface and not the soft material. For the smallest displacement rate, they even showed that the crack propagated all along the same interface.

The author of the present work also proceeded to testing of two samples at a displacement rate of 0.25mm/min at the very begining but the test were soon modified to have a displacement rate of 3.5mm/min as it was not possible to continue with the previous one due to a lack of time and logistic storage of data. The tests were stopped before the total breaking of the samples as it was taking too much time. Nonetheless, the load-displacement curve of those testing are still presented here below on FIGURE 53 in order to compare it to FIGURE 44 to visualise the effect of the displacement rate. One can see that the peak load of the horizontal gradient sample is approximately twice higher than the one of the vertical gradient and that both peak load are lower that when the test is conducted at a displacement rate of 3.5mm/min.

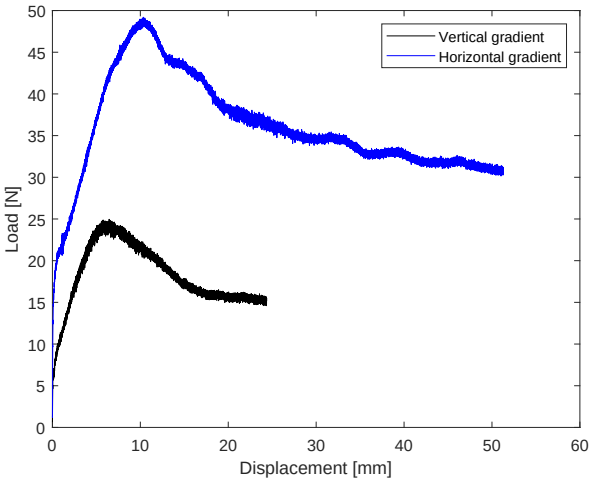

Figure 53: Load-displacement curve for two samples at a displacement rate of 0.25mm/min

Influence of the printing direction

The influence of the printing direction for the design of the flat interface has also been investigated by *Vu and al.* [32]. They tested four printing configurations :

- 1 : the first one was printed with its longitudinal axis along the x-axis with the interfaces in the zx-plane. The load was applied in the y-axis.
- 2 : the second one was printed with its longitudinal axis along the y-axis with the interfaces in the xy-plane. The load was applied in the z-axis.
- 3 : the third one was printed with its longitudinal axis along the x-axis with the interfaces in the xy-plane. The load was applied in the z-axis. It is the configuration used in this study.
- 4 : the fourth one was printed with its longitudinal axis along the y-axis with the interfaces in the zy-plane. The load was applied in the x-axis.

At constant strain rate, they showed that the printing configuration producing the samples needing the most fracture energy are respectively, in decreasing order, the n°1, the n°2, the n°3 and finally the least fracture energy needed was for the n°4. It is then confirmed that the printing configuration chosen in this study is a weak one, as expected and explained previously.

3.3 Conclusion

First, about the pixel maps : the analysis of the pixel maps revealed a repeating pattern of defects on both the interface of the vertical and horizontal gradient. Defects that are alternating at almost constant length with correct pattern design. The explanation for the recurrence of such defects along the interface of the x-axis is unknown. The most intuitive explanation would be that there is a problem with the scale used along the x-axis when creating the .STL file, i.e., that this scale would not be the same of the hardware of the printer, thus resulting in ObjetStudio producing defects when computing the pixel maps. However, such an explanation is to reject as the scale used is precisely the one of the printer, and moreover, using this scale resulted in good results in the first part of this work, results not showing this kind of repeating defects pattern. One last argument for the exclusion of this explanation is that the samples are exactly 140mm long as designed initially, it would not be the case if the scale in the x-axis used to create the .STL file was not the same as the one of the printer.

A closer analysis of the distribution of the volume fraction of TB+ in the pixel maps revealed more information :

For the vertical gradient sample, the average gradient of each layer in the xy-plane stacked along the z-axis was not affected by the defects and was in very good concordance with the gradients designed for each of those layers. This allows to conclude that even though defects are presents in the layers, they do not disturb the average gradient of each layer, meaning that the results obtained for the vertical gradient can be considered valid for the entire sample as properties can be considered uniform..

For the horizontal gradient sample, results are differents. The defects completely modify the overall average gradient of the 6 types of layers in the yz-plane. All those gradients present a value around 50% volume fraction, no matter the designed gradient. The horizontal gradient sample then has to be considered as an alternative succession of correct pattern followed by packs of defects which can not allow to consider an overall uniform distribution on the total length of the sample, and by so can not allow to consider the properties of the sample uniform along its length.

This difference in the pixel map has a direct influence on the results : The vertical gradient present a smooth load-displacement curve while the horizontal one is serrated (same observation for the fracture energy curve). It is then possible to say now that this alternation between correct pattern and packs of defects in the pixel map of the horizontal gradient sample is at the origin of the serrated curve. Indeed, the load is increasing everytime the crack encounters a defect pack as those defects present wider lines of VW+, as seen on FIGURE 52, they can withstand a higher load before breaking.

Concerning the results in themselves, it is surprising the see that the vertical gradient sample performed less good than the flat interface. It can be explained by comparison of the broken interfaces. The interfaces of the vertical gradient sample are both exactly identical without any mosaïc pattern normally characterising the interfaces after such a test. It seems that the crack is propagating in the soft pure TB+ layers and not at any intermediate gradient layers below or above. This results in a much lower fracture energy than the flat interface sample as the TB+ is a very soft rubber-like material.

On the other hand, the horizontal gradient sample is performing better than the flat interface one : the crack is propagating slower and the sample is more has a higher fracture energy as expected while designing it.

Finally, the values of corrected crack length $crack_{corrected}$ obtained for all three samples being in good accordance with the experimental data, the use of the model of the corrected beam theory for computing the fracture energies is validated.

4 Conclusion

4.1 Voxel 3D printing

First, the pixel maps of the different designs present defautls and errors that cannot be explained by an error of voxel scale input when proceeding to the creation of the .STL file. Those defects are more present as the size of the features is approaching the minimal voxel size and are even producing a repeated defect pattern in the pixel map of the second part of this work.

Visual inspection revealed that the quality of the inclusion features of TB+ into a bulk of VW+ material are depending on the printing direction. For features printed with their longitudinal axis along the printing direction, the quality is very good with very well defined features and a clear sharp interface between the two materials and so no matter of the width of the features. However, the features with their longitudinal axis oriented perpendicular to the printing direction have a less good quality of print : there is presence of a staircase effect along the features, especially for the thinner ones where it becomes so strong below 170µm that the features seems cut and segmented into small patchs of TB+ inclusion. This effect is most probably due to the printing technology : a high speed of printheads depositing droplets while moving along only one direction causes an inertia effect in the droplets that are then elongated along the printing direction and by consequence less elongated along the direction perpendicular to the printing one.

Visual inspection of the squares features revealed that standalone features are viable only when their dimension does not go less than 200µm, as suggested [33]. For stand alone features smaller than 200µm, they seems to be mixed and hardly distinguishable from the builk of VW+ around them and when they are distinguishable they cannot be considered as inclusion of pure TB+ anymore.

The visual inspection of faces of the multimaterial sample of Grey60 allow to conclude that there is an anisotropy in the geometry of the inclusion of TB+. Anisotropy that is depending on the printing method inherent to the Polyjet technology of the printer and also on the voxel size of the inclusion of TB+. Faces along the xy-plane tends to present elongated inclusion of TB+ resulting from antagonist effects that are the direction of the movement of the printheads and the anisotropic dimensions of the voxel whereas faces along the yz-plane present more elongated inclusion of TB+ that are resulting from the cumulative effects here above presented.

4.2 Bimaterial attachment

Second, the vertical gradient sample could be considered uniform in the volume fraction and so in the properties of each of the layers of its interface as an analysis of the distribution of the bimaterial on the pixel map of each layers was conducted and even though the repeating defect was present, it was not affecting the overall volume fraction of each layer. This conclusion cannot be applied for the horizontal gradient sample has the same analysis revealed that it needs to be considered as an alternation of uniform packs of layers, one pack being the defect one and one pack being the correct pattern.

The result of this alternation of packs of different properties is that the interface of this sample is consisting in a succession of large lines of materials perpendicular to the longitudinal axis of the sample followed by lines of normal width. This succession is repeating every ≈ 3.5µm and is translated in a serrated load-displacement curve whereas the flat interface and the vertical gradient sample present a smooth decreasing load-displacement curve after the peak load. This serration can also be seen on the fracture energy curve.

The fracture energy curves revealed that the horizontal gradient sample is performing the best but most surprisingly it showed that the vertical gradient sample is performing less good than the flat interface sample, which is a the counter intuition of the author. It can be explained by

comparison of the broken interfaces. The interfaces of the vertical gradient sample are both exactly identical without any mosaïc pattern normally characterising the interfaces after such a test. It seems that the crack is propagating in the soft pure TB+ layers and not at any intermediate gradient layers below or above. This results in a much lower fracture energy than the flat interface sample as the TB+ is a very soft rubber-like material. It results in the horizontal gradient performing twice as good as the vertical one is doing and it can be seen on all the graph of the eveolution of the crack length depending on time and the fracture energy graph.

The results are considered valid as the interpolation of the cube root of the corrected compliance fits quite well theexperimental datas, which a indication of the validity of the corrected beam theory applie to the samples here [32], [18].

4.3 Limitations

After comparison of the different pixel maps between them and a frequent use of the software *ObjetStudio*, it appears that it presents some unexplainable behaviour :

- When the position of the sample on the building tray changes, the pixel map changes. One could think it is due to the grid deposition pattern due to the hardware of the printer, and so by proceeding to "automatic placement" after moving the sample on the tray, it would come back to an initial position corresponding to the first placement, position who would be the same for every "automatic placement", but it is not. The pixel map changes everytime the sample is moved even the ones after proceeding to "automatic placement" are different from another.

- It is still not understood why defects appears on the pixel map of samples built and designed with the given resolution of the hardware (the printer). Theoritically, they should not be present.

For all those reasons, it is not possible to be 100% sure that *ObjetStudio* will respect all geometries and material composition that are given to print, especially when the dimensions of the features are below four times the minimal voxel size

4.4 Experimetal tests

Regarding the fracture energies tests, only one sample for each configuartion was printed and tested and so no statistical inference can be drawn out of the results. This is due the lack of time remaining when proceeding to those tests during the work on this master thesis. It would be interesting for further work to investigate the repeatability of the results, especially because the surprising bad performances of the vertical gradient sample needs to be confirmed.

Also the displacement rate of 3.5mm/min is high compare to the other studies [32] [20] but it was due to the lack of time remaining and a limitation of data storage for the video recording. The influence of the displacement rate can still be seen on the load-displacement curve of the test conducted under the first displacement rate of 0.25mm/min. The peak load are less high and the horizontal gradient peak load is twice as big as the vertical gradient one whereas it is no longer the case at 3.5mm/min. It would be interesting for further work to reduce it to a maximum of 0.1mm/min for reducing strain rate effects and to fit others studies to be able to compare the results with them.

4.5 Design only achievable with 3D printer

One design in this study is not transposable to a normal CNC building process, it is the one of the horizontal gradient interface. One can see here all the interest of using additive manufacturing technologies to create new design with specific functionalities.

4.6 Indication for further work

4.6.1 Voxel 3D printing

If further investigations will be done on voxel printing using the Stratasys Objet260 Connex 1, it would be interesting to investigate more in details the slicing process of *ObjetStudio* in order to understand why there are presence of defects which presence are not explained yet. If the problem remains, direct contact with the Stratasys company should be encouraged as those defects are probably only due to the software *ObjetStudio* and not to the .STL file given in input.

Concerning further studies done using the Polyjet technology in general, it would be interesting to investigate the material properties of sample printed in digital materials mode with volume ratios close to 50% to see if the material in the least proportion can still be considered as an inclusion inside the base material or not. Functionally graded materials using any volume fraction should be more investigated as it will open the range of combination and possibilities of applications.

4.6.2 Bimaterial attachment

If further investigations will be done on fracture toughness of the interface of a bimaterial, it would be intersting to test samples that presents different widths of intermediate gradients between the VW+ and the TB+. Varying this width to stay in a range close to 500µm [34] can also be combined to vary the volume fraction of materials in the intermediate layers. One could also make the number of intermediate layers vary. As so, the characterisation of the fracture toughness of the interface depending on the width of the intermediate layers, theirs numbers and their composition would be complete. As such a study would be too much time consumming if it was to be done experimentally, it is advised to proceed to use of a FEM code to iterate over all the possibilities and to print only the most interesting configurations to confirms the simulationn results by experimentals tests [14].

5 Bibliography

References

[1] Qi Ge, H. Jerry Qi and Martin L. Dunn, *Active materials by four-dimension printing*, Applied Physics Letters 103, 131901 (2013); http://dx.doi.org/10.1063/1.4819837.

[2] E.L. Doubrovski, E.Y. Tsai, D. Dikovsky, J.M.P. Geraedts, H. Herr and N. Oxman, *Voxel-based fabrication through material property mapping : A design method for bitmap printing*, Computer-Aided Design 60 (2015) 3–13, http://dx.doi.org/10.1016/j.cad.2014.05.010.

[3] Wonjoon Cho, Emanuel M. Sachs, Nicholas M. Patrikalakis and Donald E. Troxel, *A dithering algorithm for local composition control with three-dimensional printing*, Computer-Aided Design 35 (2003) 851–867.

[4] W. Cho, E. M. Sachs, N. M. Patrikalakis, M. J. Cima, T. R. Jackson, H. Liu, J. Serdy, C. C. Stratton, H. Wu and R. Resnick, *Methods for Distributed Design and Fabrication of Parts with Local Composition Control*.

[5] W.K. Chiu and K.M. Yu, *Direct digital manufacturing of three-dimensional functionally graded material objects*, Computer-Aided Design 40 (2008) 1080-1093, doi:10.1016/j.cad.2008.10.002.

[6] P. Fratzl, H. S. Gupta, E. P. Paschalis and P. Roschger, *Structure and mechanical quality of the collagen–mineral nano-composite in bone*, J. Mater. Chem. , 2004, 1 4 , 2115–2123.

[7] Laura Zorzetto, *Bioinspired and Architectured Materials with Enhanced Mechanical Performance by Three-dimensional Printing*, PhD report, University of Liège.

[8] Dimitri Kokkinis, Florian Bouville and André R. Studart, *3D Printing of Materials with Tunable Failure via Bioinspired Mechanical Gradients*, Adv. Mater. 2018, 1705808, https://doi.org/10.1002/adma.201705808.

[9] Theresa Swetly, Jürgen Stampfl, Gero Kempf, Rainer-Michael Hucke, Marcus Willing and Marina Warkentin, *Bioinspired engineering polymers by voxel-based 3D printing*, BioNanoMat 2015; 17(3-4): 145-157, DOI 10.1515/bnm-2015-0021.

[10] Studart A. R. , textitAdditive manufacturing of biologically-inspired materials, Chemical Society Reviews, 2016, 45(2):359–376.

[11] Jonathan Hiller Hod Lipson, (2010), *Tunable digital material properties for 3D voxel printers*, Rapid Prototyping Journal, Vol. 16 Iss 4 pp. 241 - 247

[12] J.P. Moore and C.B.Williams, *Fatigue characterization of 3D printed elastomer material*, Solid Freeform Fabrication Symposium 2012, pp. 641–655.

[13] J.P. Moore and C.B.Williams, *Fatigue properties of parts printed by PolyJetmaterial jetting*, Rapid Prototyp. J. 21 (2015) 675–685, https://doi.org/10.1108/Rpj-03-2014-0031.

[14] Grace X. Gu, Susan Wettermark and Markus J. Buehler, *Algorithm-driven design of fracture resistant composite materials realized through additive manufacturing*, Additive Manufacturing 17(2017)47–54, http://dx.doi.org/10.1016/j.addma.2017.07.002.

[15] Fernando A. Cordisco, Pablo D. Zavattieri, Louis G. Hector Jr. and Blair E. Carlson, *Mode I fracture along adhesively bonded sinusoidal interfaces*, International Journal of Solids and Structures 83 (2016) 45–64.

[16] Yizhong Hu, Victor Birman, Alix Deymier-Black, Andrea G. Schwartz, Stavros Thomopoulos, Guy M. Genin, *Stochastic Interdigitation as a Toughening Mechanism at the Interfacebetween Tendon and Bone*, Biophysical Journal, Volume 108, January 2015, 431-437.

[17] Antoine De Brouwer, *Toughness And Damage Tolerance Of Biologically Inspired Bi-Material Interfaces Investigated By 3D Printing And Testing*, Master Thesis, University of Liège, June 2018.

[18] B.R.K. Blackman, H. Hadavinia, A.J. Kinloch, M. Paraschi and J.G. Williams, *The calculation of adhesive fracture energies in mode I:revisiting the tapered double cantilever beam (TDCB) test*, Engineering Fracture Mechanics 70 (2003) 233–248.

[19] B. Standards, *Determination of the Mode I Adhesive Fracture Energy, GIc, of Structural Adhesives Using the Double Cantilever Beam (DCB) and Tapered Double Cantilever Beam (TDCB) Specimens*, British Standards Institution, BS 7991:2001, London, 2001.

[20] Thomas S. Lumpe, Jochen Mueller and Kristina Shea, *Tensile properties of multi-material interfaces in 3D printed parts*, Materials and Design 162 (2019) 1–9.

[21] Nicholas Alexander Meisel, David A. Dillard and Christopher B. Williams, *Impact of material concentration and distribution on composite parts manufactured via multi-material jetting*, Rapid Prototyping Journal, DOI 10.1108/RPJ-01-2017-0005.

[22] Lindsey B. Bass, Nicholas A. Meisel and Christopher B. Williams, *Exploring variability in material properties of multi-material jetting parts.*

[23] Dorcas V. Kaweesa and Nicholas A. Meisel, *Quantifying fatigue property changes in material jetted parts due to functionally graded material interface design*, Additive Manufacturing 21 (2018) 141–149.

[24] D.J. Brackett, I.A. Ashcroft, R.D. Wildman and R.J.M. Hague, *An error diffusion based method to generate functionally graded cellular structures*, Computers and Structures 138 (2014) 102–111.

[25] Qun Lou and Peter Stucki, *Fundamentals of 3D Halftoning.*

[26] M. J. Mirzaali, M. E. Edens, A. Herranz de la Nava, S. Janbaz, P. Vena, E. L. Doubrovski and A. A. Zadpoor, *Length-scale dependency of biomimetic hard-soft composites*, Scientific Reports (2018) 8:12052.

[27] Shawn Moylan, John Slotwinski, April Cooke, Kevin Jurrens and M. Alkan Donmez, *An Additive Manufacturing Test Artifact*, Journal of Research of the National Institute of Standards and Technology, Volume 119 (2014) 429-459.

[28] Hongyi Yang, Jingying Charlotte Lim, Yuchan Liu, Xiaoying Qi, Yee Ling Yap, Vishwesh Dikshit, Wai Yee Yeong and Jun Wei, *Performance evaluation of ProJet multi-material jetting 3D printer*, Virtual and Physical Prototyping, 2017, Vol. 12, No. 1, 95-103, `http://dx.doi.org/10.1080/17452759.2016.1242915`.

[29] Jochen Mueller, Diana Courty, Manuel Spielhofer, Ralph Spolenak and Kristina Shea, *Mechanical Properties of Interfaces in Inkjet 3D Printed Single- and Multi-Material Parts*, 3D Printing and Additive Manufacturing, Volume 4, Number 4, 2017, DOI : 10.1089/3dp.2017.0038.

[30] J. Mueller, K. Shea, C. Daraio, *Mechanical properties of parts fabricated with inkjet 3D printing through efficient experimental design*, Materials and Design 86 (2015) 902-912, `http://dx.doi.org/10.1016/j.matdes.2015.07.129`.

[31] Laura Zorzetto, *Multiscale Analysis of Interface Properties in 3D Printed Composites*, soon to be published.

[32] Ivan Q. Vu, Lindsey B. Bass, Christopher B. Williams and David A. Dillard., *"Characterizing the effect of print orientation on interface integrity of multimaterial jetting additive manufacturing"*, Additive Manufacturing 22 (2018) 447–461.

[33] Nicholas Alexander Meisel, *Design for Additive Manufacturing Considerations for Self-Actuating Compliant Mechanisms Created via Multi-Material PolyJet 3D Printing*

[34] L. Rossetti, L. A. Kuntz, E. Kunold, J. Schock, K. W. Müller, H. Grabmayr1, J. Stolberg-Stolberg, F. Pfeiffer, S. A. Sieber, R. Burgkart and A. R. Bausch, *The microstructure and micromechanics of the tendon–bone insertion*, Nature Materials, volume 16, June 2017, DOI: 10.1038/NMAT4863.

6 Appendix

The appendix is composed of mainly two parts. The first part is an investigation on the possibility to print more digital materials than the 12 settled by the manufacturer by using different algorithms that are producing such dithering patterns that are what ObjetStudio is actually doing. A comparison between the results obtained using those different algorithms is done regarding the distribution of the materials inside the dithering pattern and the error on the desired volume fraction.

The second part is a presentation of the very first sample design that was done to investigate voxel 3D printing and its results.

6.1 Digital materials & dithering patterns

12 intermediate ratios between the VW+ and the TB+ is very restrictive, not even taking into consideration that there is a gap of achievable ratio between 18% and 64% of TB+. The first objective will be to find a method that allows to produce dithering patterns with whatever ratio desired. This will allow to bypass the limitation of the printer and to print pieces with any volume ratio.

Different algorithms for producing a dithering pattern with a desired volume ratio will be investigated : the random distribution; the semi-random pattern in 2D and 3D, also called the error diffusion. For each algorithms, the accuracy of the volume ratio of the obtained dithering pattern and the cluster size distribution will be analysed and compared. It is of interest to not only have an idea of the accuracy of the algorithms but also to have information about the distribution produced. The cluster is defined as building blocks being directly in contact with each other by a side, not by a corner. Basically, are counted as in the cluster, the neighbor building blocks in "cross". An example is shown on FIGURE 54.

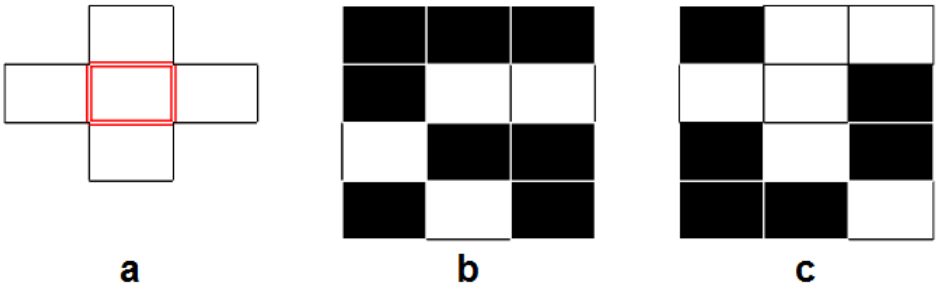

Figure 54: a : cross showing how neighbor building blocks are counted as from the same cluster. b and c : example images showing respectively 1 white cluster of size 2 and 2 white clusters of size 1 for b and 1 white cluster of size 5 and 1 cluster of size 1 for c.

The information given by the clusters size distribution are considered enough for this work as the dithering patterns will be produced from a non existing image and will not be a transformation of an existing grayscale image to its dithering pattern image or the final dithering image will not exhibit a specific design feature requiring another information parameter. There is no need here to use a metric such as the edge density as suggested by Meisel [33].

The influence of the size of the dithering pattern in terms of matrix size (that are taken square) on the obtained ratios will also be investigated as speaking about mechanical properties of a dithering pattern has a meaning only at an overall length scale, higher than the one of his smallest element (the building blocks here).

6.1.1 Random pattern in 2D

The random distribution is obtained using the *rand* function from Matlab that fills a 2D array of uniformly distributed random number. The elements of this matrix are then compared to the volume fraction desired and changed accordingly : if the number is higher than the desired ratio, it is turned to 0 and if the number is lower than the desired ratio, it is turned to 1. A random pattern using this technique is shown on FIGURE 55.

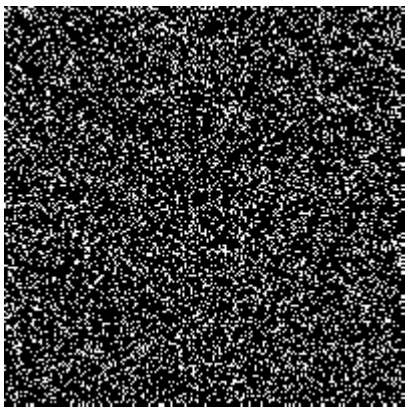

Figure 55: Example of dithering pattern at 20% volume fraction of white pixels using the random distribution. The image is 200x200 pixels.

Because of the variability of the *rand* function in Matlab, multiples draws need to be taken in order to compute an average volume fraction over all those draws and to be able to show the average error of the obtained VF.

6.1.2 Error diffusion in 2D [24]

Error diffusion is one of the two category of 2D halftoning. Error diffusion transforms a grayscale input image into a binary (black and white) representation using an adaptive algorithm and a fixed threshold. It stores the error at each pixel and diffuses it to its neighbours pixels. Let "A" be a 2D array with each pixel representing a color value in the grayscale. Each position A_{xy} is compared to a threshold value (t), here taken at 127, and the difference determines if the corresponding pixel in the binary matrix should be black or white :

$$b_{x,y} = \begin{cases} 255 & \text{si } b_{x,y} > t \\ 0 & \text{otherwise.} \end{cases}$$

where black = 0 and white = 255.

the error, e_{xy}, is obtained by $e_{xy} = A_{xy} - b_{xy}$ and is carried to the adjacents pixels using the relation :

$$\begin{bmatrix} A_{x+1,y} \\ A_{x+1,y+1} \\ A_{x,y+1} \\ A_{x-1,y+1} \end{bmatrix}^{i+1} = \begin{bmatrix} A_{x+1,y} \\ A_{x+1,y+1} \\ A_{x,y+1} \\ A_{x-1,y+1} \end{bmatrix}^{i} + e_{x,y} \begin{bmatrix} f_{x+1,y} \\ f_{x+1,y+1} \\ f_{x,y+1} \\ f_{x-1,y+1} \end{bmatrix}$$

where f_{xy} are the coefficient of the filter of Floyd and Steinberg illustrated on TABLE 6.

	A_{xy}	7/16
3/16	5/16	1/16

Table 6: Filter of Floyd-Steinberg for 2D images

The parameter to tune in order to obtain any volume ratio with this algorithm is the value of each pixel on the initial grayscale input array. All pixels needs to have the same value in order for the method to work. The 2D array A_{xy} is then initialised as :

$$A_{x,y} = VF \times \frac{255}{100} \times U_{x,y}$$

where VF is the desired volume fraction and U_{xy} is the unitary matrix of size $x \times y$. An illustration of the procedure is shown on FIGURE 56.

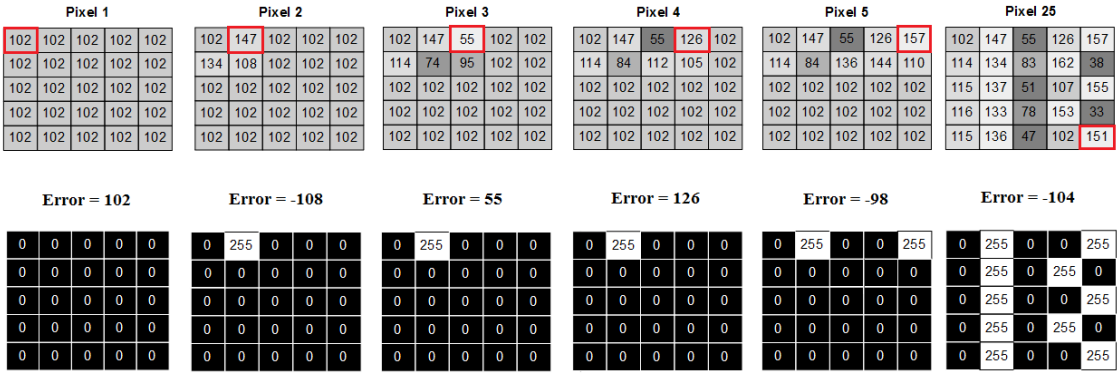

Figure 56: Example of the procedure of the algorithm for a matrix of 5×5 with an initialised desired VF of 40%.

The illustration possesses 10 white pixels as 40% of 25 is 10.

An example of dithering pattern using this error diffusion method is visible on FIGURE 57 for a VF of 23%.

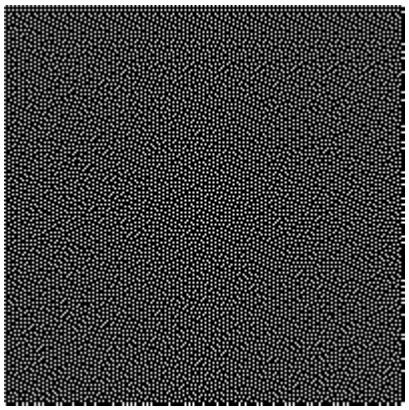

Figure 57: Example of dithering pattern at 23% volume fraction of white pixels using the semi-random distribution. The image is 200x200 pixels.

6.1.3 Error diffusion in 3D [25]

As explained by Lou & Stucki [25], applying the filter of Floyd-Steinberg slicewise to obtain a 3D error diffusion is not suitable as it brings artifacts into the resulted dithering image. Instead, a new filter, called the *Stucki filter*, is applied in order to get a dithering image.

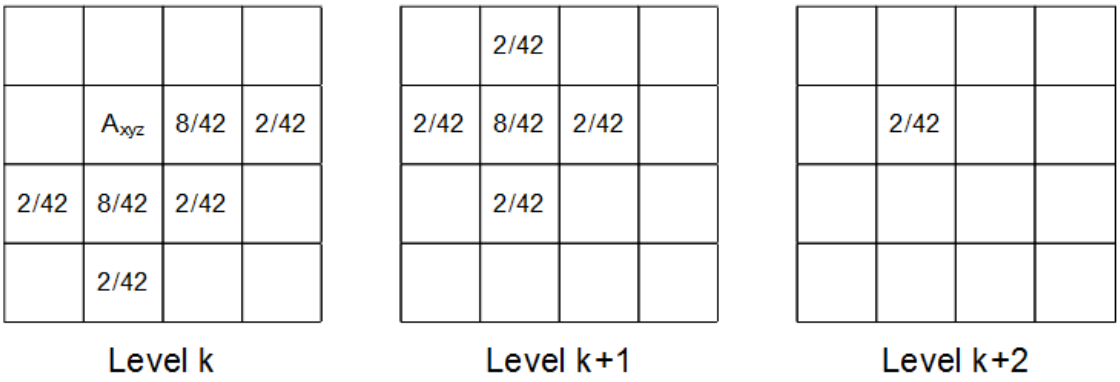

Figure 58: The 3D error diffusion filter, also called Stucki filter.

The algorithm is the same as for 2D error diffusion, only the filter changes. As one can see on FIGURE 58, the filter affects different level of depth, represented by the index k, in order to truly work on a 3D level and not just slicewise. As for the 2D error diffusion, the influence of the size of the 3D array on the accuracy of the obtained VF will be investigated as well as the cluster size distribution.

An example of the dithering pattern obtained for a volume fraction of 40% is shown on FIGURE 59. As one can see, the filter does work in a 3D fashion as the axial, sagital and coronal slice are all different and without artifacts.

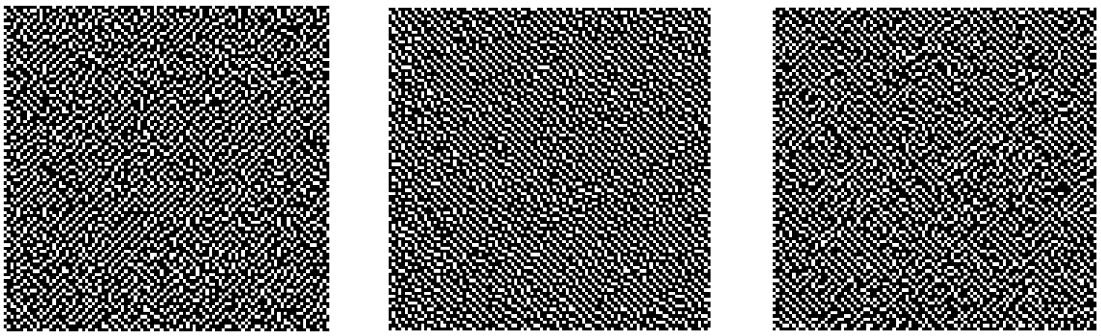

(a) Axial view (b) Sagital view (c) Coronal view

Figure 59: Axial, sagital and coronal view at slice 50 each of a dithering 3D image for a VF of 32%

6.1.4 Ordered pattern

Ordered pattern are usually qualified as "chessboard pattern" because of the regular ordering it produces. An example of such an ordered pattern is shown on FIGURE 60.

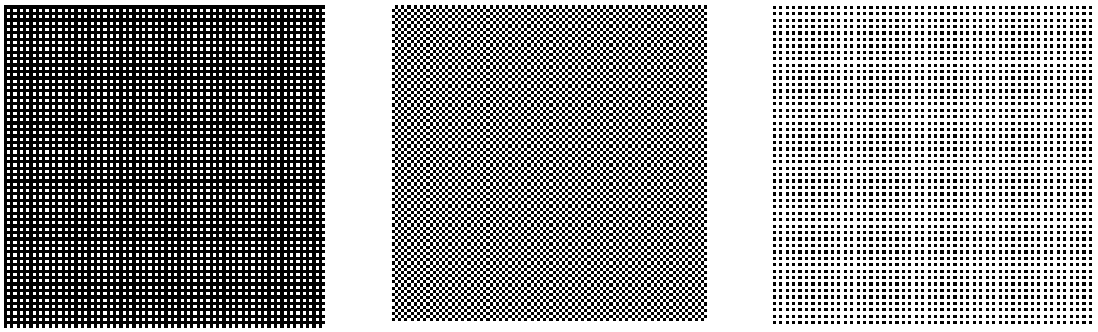

(a) Ordered dithering pattern for a VF of 25%

(b) Ordered dithering pattern for a VF of 50%, a chessboard pattern

(c) Ordered dithering pattern for a VF of 75%

Figure 60: Ordered dithering pattern for VF of (a) 25%, (b) 50%, (c) 75%

Ordered pattern are usually appreciated in the literature [26] for designing parts because of its easy pattern and the fact that the distribution is uniform (so risk of defect area are reduced) which is easy to characterise and account for homogenous properties through the all sample.

6.1.5 Random dithering pattern

The FIGURE 61 here below shows that the error on the objective VF decreases as the dimension of the cell increases, as expected. One can see that for a cell dimension of 100, the error is approximately 0.05% only and reach a constant value near 0% for a dimension of 300 (it means a cell of 300x300). Even for the smaller cell dimension, the error is very small, 0.3% at the begining, which means that the average volume fraction over the 100 draws is very accurate.

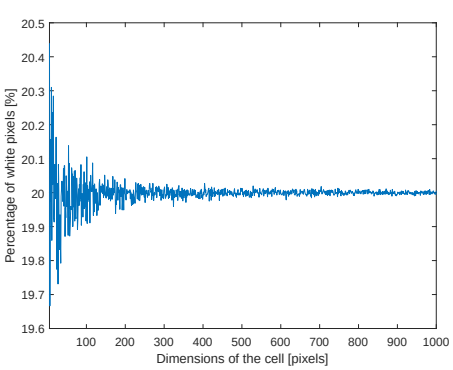

(a) Obtained VF in function of the dimension of the cell for an objective VF of 20%

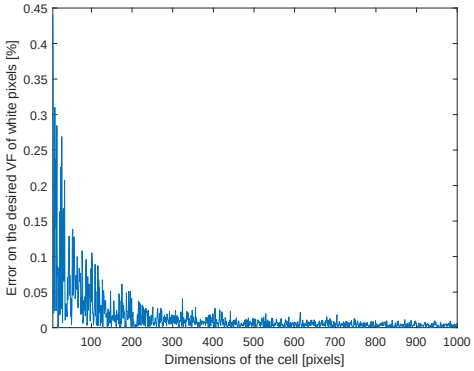

(b) Error in percent of the VF compared to the objective one in function of the dimension of the cell

Figure 61: Evolution of the obtained VF (a) and the error of VF (b) in function of the dimension of the cell for an objective VF of white pixels of 20% over 100 draws

Those graphs were obtained after averaging 100 draws from the random function in *Matlab* to account for the variability of this function and have an average of the random pattern.

An histogram of the cluster size distribution of the whites pixels is shown on FIGURE 62 for a cell of dimension 200 and of VF 20%.

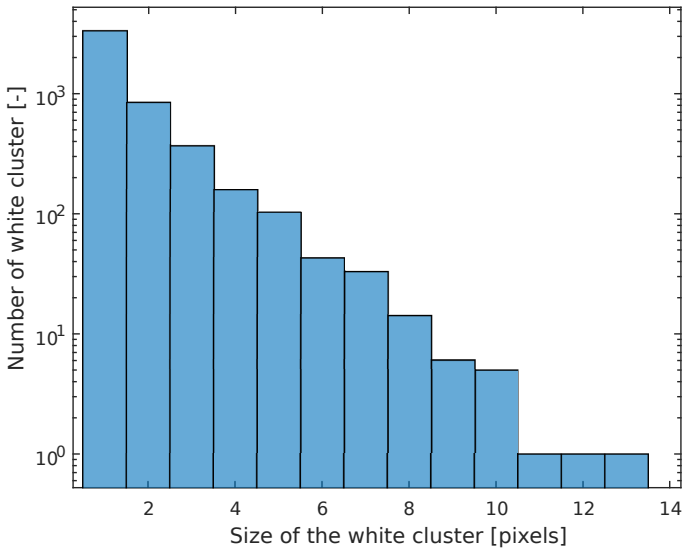

Figure 62: Cluster size distribution for a cell of dimension 200 and objective VF of 20%.

One can see that the size distribution of the clusters is quite broad as it goes up to cluster of size 13. It is also decreasing as the size of the cluster is increasing with the maximum of clusters for cluster of unitary size.

6.1.6 Semi-random dithering pattern in 2D

On FIGURE 63, one can see that as the dimension of the cell increases, the error on the objective VF is decreased, as expected. The error decreases rapidly as the dimension of the cell increases until it reaches a dimension of 100, for which the error is approximately 1%. It then decreases very

slowly as the dimension increases. Here it is reasonable to consider that a cell of dimension 100 can represent correctly enough an overall uniform material of objective VF as its error is of 1%. The limit of the error could be pushed at a dimension of 50 (2125µm) , which would be consistent with other findings stating that the smallest feature size for uniform material properties is 2mm [21].

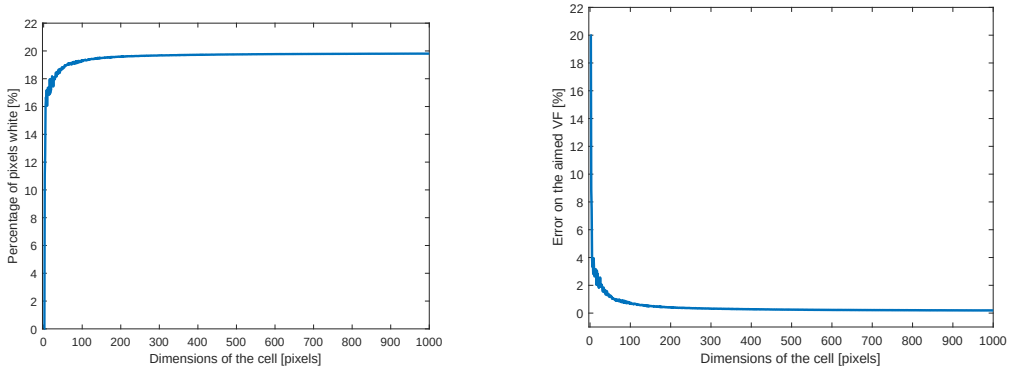

(a) Obtained VF in function of the dimension of the cell for an objective VF of 20%

(b) Error in percent of the VF obtained compared to the objective one in function of the dimension of the cell

Figure 63: Evolution of the obtained VF (a) and the error (b) in function of the dimension of the cell for an objective VF of white pixels of 20%

An histogram of the cluster size distribution of the whites pixels is shown on FIGURE 64 for a cell of dimension 200 and of VF 20%.

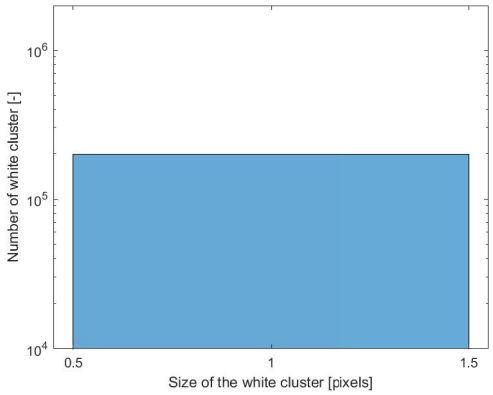

Figure 64: Cluster size distribution for a cell of dimension 200 and objective VF of 20%.

For the semi-random dithering pattern, there are only cluster of unitary size for a VF of 20%.

6.1.7 Semi-random dithering pattern in 3D

One can see on FIGURE 65 that when the dimension of the cell increases, the obtained VF tend to approach the desired VF of 32% but it exceeds it around the dimension of 41. As consequence, the error on the VF decreases until this dimension, where it is minimal, and increases again after as the VF exceeds the one desired. The error decreases rapidly under 0.5% and after the minima it seems to tend to an error of 0.25% as cell dimension increases. The same remark concerning the smallest feature size for uniform material properties [21] can be done here.

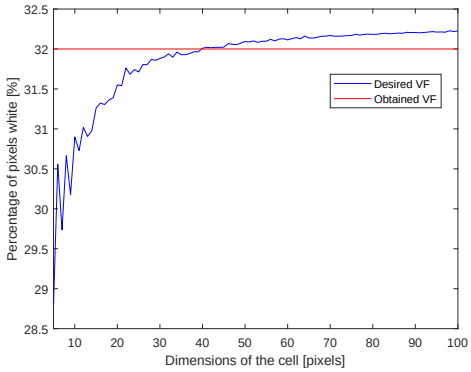

(a) Obtained VF in function of the dimension of the cell for an objective VF of 32%

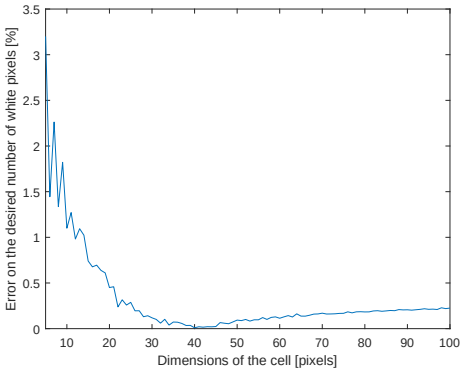

(b) Error in percent of the VF obtained compared to the objective one in function of the dimension of the cell

Figure 65: Evolution of the obtained VF (a) and the error (b) in function of the dimension of the cell for an objective VF of white pixels of 32%

A closer look at the evolution of the error is available on FIGURE 66. One can see that even though the dimension of the cell increases a lot, the error increases very slowly in comparison but it is not possible to state that it tends asymptotically to a constant value or if the increase is unlimited.

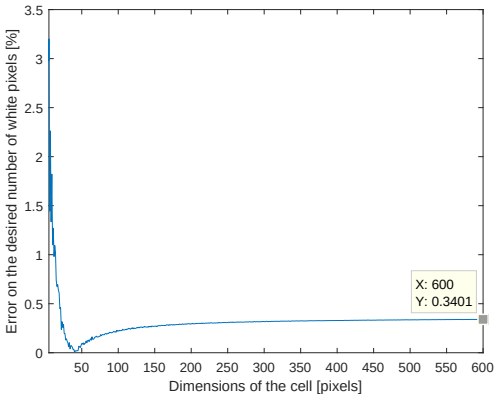

Figure 66: Evolution of the error for a desired VF of 32%.

On FIGURE 67, one can see that clusters are ranging from the most numerous for clusters of size 1 to the least numerous for clusters of size 8 (1 cluster of size 7 and 1 of size 8) and that their number decreases every time their size increases . Even for a dithering image of $100 \times 100 \times 100 = 1$ million elements, the maximal cluster size is 8, which can allow to say from the Stucki filter that it allows an homogeneous distribution through the 3D array without formation of big clusters. This suggests that when the cell dimension is big enough, the properties of the cell are global and not only local.

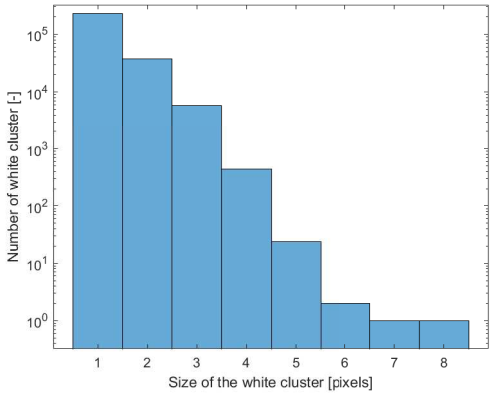

Figure 67: Cluster size distribution for a cell of dimension 100 and desired VF of 32%.

6.1.8 Comparison between random and semi-random dithering pattern

To compare the two different dithering pattern obtained in 2D, the focus will be put on their accuracy on the aimed VF, with dimension chosen at 200 so that the error can be considered as having reached its constant value, and their cluster size distribution. It will be compared for every step of VF of 10%. The Table 7 and Table 8 show that the random pattern is generally more precise than the semi-random one for which it seems that the error stays around 0.4%, except for an aimed VF of 50% where the semi-random pattern makes no error.

Random pattern	10%	20%	30%	40%	50%
Average VF of VW	10.0033%	19.9966%	29.9969%	40.0075%	49.9982%
Average error on VF	0.0033%	0.0034%	0.0031%	0.0075%	0.0018%
Semi-random pattern	10%	20%	30%	40%	50%
VF of VW	10.025%	19.5875%	29.95%	49.6125%	50%
Error on VF	0.025%	0.4125%	0.05%	0.3875%	0%

Table 7: Volume fraction obtained for aimed VF of 10 to 50 and the error on the VF for the random and the semi-random dithering pattern for a cell dimension of 200. The averaging for the random pattern has been done on 500 draws.

Random pattern	60%	70%	80%	90%
Average VF of VW	59.9936%	70.0102%	80.0085%	89.9956%
Average error on VF	0.0064%	0.0102%	0.0085%	0.0044%
Semi-random pattern	60%	70%	80%	90%
VF of VW	59.7425%	69.54255%	79.645%	89.575%
Error on VF	0.2575%	0.4575%	0.355%	0.425%

Table 8: Volume fraction obtained for aimed VF of 60 to 90 and the error on the VF for the random and the semi-random dithering pattern for a cell dimension of 200. The averaging for the random pattern has been done on 500 draws.

The comparison of the cluster size distribution will allow to understand the qualitative "mixing" of the dithering pattern. Meaning how big the clusters are, if they aggregate into the matrix of complementary material or if they stay separated to have dispersed clusters.

As can be seen on FIGURE 68, the cluster size distribution of the two patterns are very different for a VF under 50%. The cluster size of the random pattern are in a broad range of values, from size 1 to size 6 for FIGURE 68 (A) and from size 1 to size 63 for FIGURE 68 (D). Also as the size of the cluster increases, their numbers decrease and discontinuities in the size of the clusters present appears. The semi-random pattern gives a different cluster size distribution as it has only very few different size of clusters, only clusters of size 1 for FIGURE 68 (A) & (B), of size 1 and 2 for FIGURE 68 (C) and only three clusters size of 1 to 3 for FIGURE 68(D). For those value of VF, the semi-random pattern gives much smaller clusters than the random pattern. It can be understood that the distribution of the VF material is more homogeneous and dispersed inside the matrix material for the semi-random pattern than for the random one. Said differently, the random pattern favours clusters of big size, leading to an uneven heterogeneous distribution of the VF material inside the matrix material.

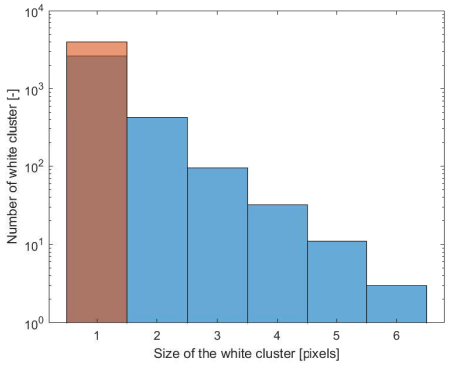

(a) Histogram of the cluster size distribution of the random pattern and the semi-random pattern for an aimed VF of 10%

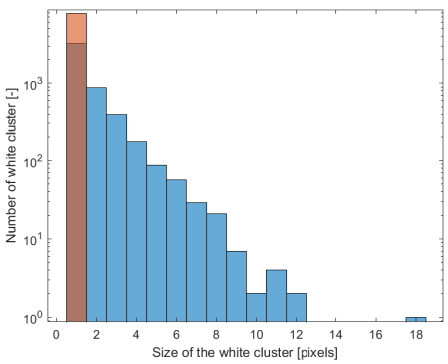

(b) Histogram of the cluster size distribution of the random pattern and the semi-random pattern for an aimed VF of 20%

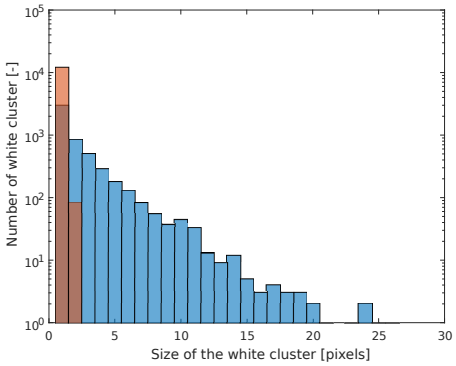

(c) Histogram of the cluster size distribution of the random pattern and the semi-random pattern for an aimed VF of 30%

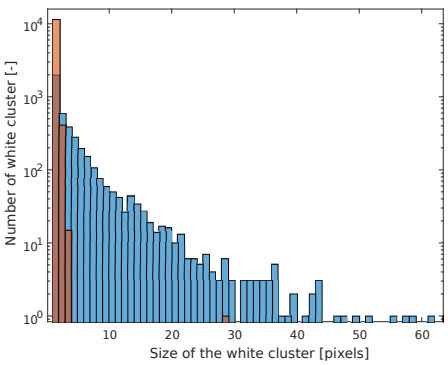

(d) Histogram of the cluster size distribution of the random pattern and the semi-random pattern for an aimed VF of 40%

Figure 68: Histogram of the cluster size distribution for an aimed VF of 10% (a), 20% (b); 30% (c); 40% (d), for a dimension of cell of 200. In blue are the data for the random pattern and in orange are the data for the semi-random one.

FIGURE 69 shows the cluster size distribution for an aimed VF of 50%. The Figure actually shows a zoomed area on the origin of axes as it is the area of interest to compare the random algorithm to the semi-random one. The random algorithm gives clusters of size 1 until size 470 (not represented here) with discontinuities on the sizes represented. The semi-random algorithm gives only clusters of size 1, 50% VF is a specific configuration which corresponds to a chessboard pattern. Then it explains the result presenting only unitary size clusters.

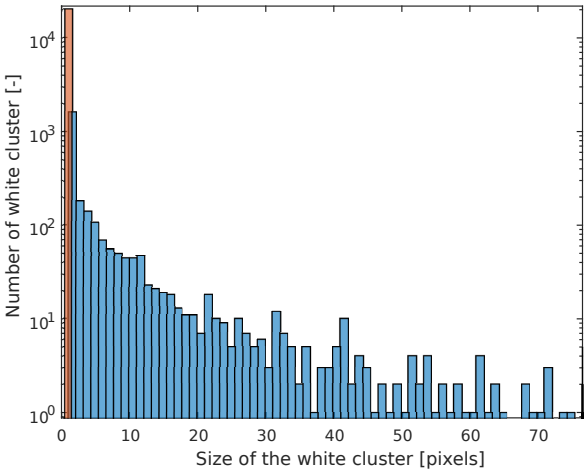

Figure 69: Histogram of the cluster size distribution (zoom on the origin of axes) for an aimed VF of 50% for a dimension of cell of 200. In blue are the data for the random pattern and in orange are the data for the semi-random one.

On FIGURE 70, one can see the histograms of the cluster size distribution for an aimed VF from 60% to 90%. All the clusters of the semi-random algorithm are present on the histogram FIGURE 70 (A). The size ranges from 1 to 50. The random algorithm gives one huge cluster of size $\approx$ 18000, few clusters of size 100 spread discontinuously until size 1. FIGURE 70 (B) the situation is the same for the random algorithm except that the huge cluster is of size $\approx$ 27000. All the clusters of the semi-random algorithm are present except one big cluster also of size $\approx$ 27000. FIGURE 70 (C) shows clusters of size 1 to size 3 for the random algorithm and clusters of size 1 for the semi-random one. Both algorithm show a huge cluster of size $\approx$ 31000. For FIGURE 70 (D), both algorithms have a big cluster of size $\approx$ 36000 and only the random one shows four clusters of size 1.

The behavior of the cluster size distribution tends to change for VF above 50%, first the two algorithms have one big cluster for a VF of 60% and 70% but still they present a lot of smaller clusters. Above those values, the size of the biggest clusters increases while the occurrence of smaller clusters decreases as the VF increases to finally arrive to a result where there is one huge cluster with very few clusters of size 1. This is of course explained as there is more white clusters so the probability that they touch each other and are neighbour increases.

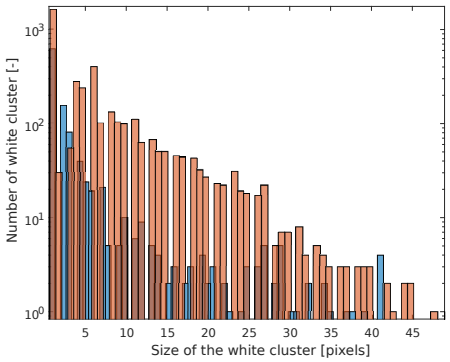

(a) Histogram of the cluster size distribution of the random pattern and the semi-random pattern for an aimed VF of 60%

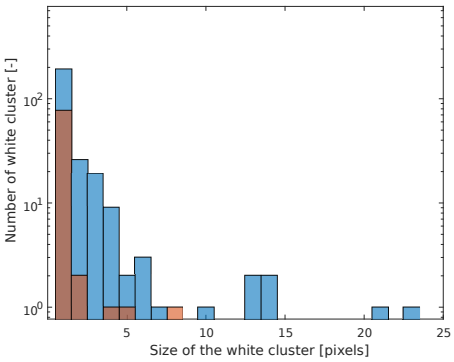

(b) Histogram of the cluster size distribution of the random pattern and the semi-random pattern for an aimed VF of 70%

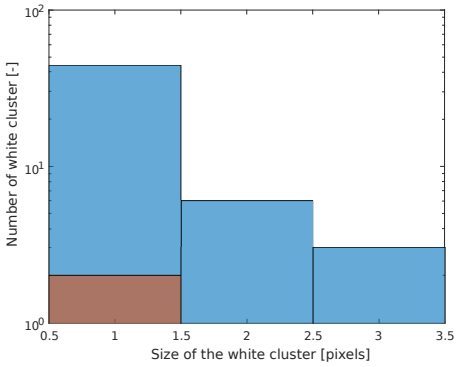

(c) Histogram of the cluster size distribution of the random pattern and the semi-random pattern for an aimed VF of 80%

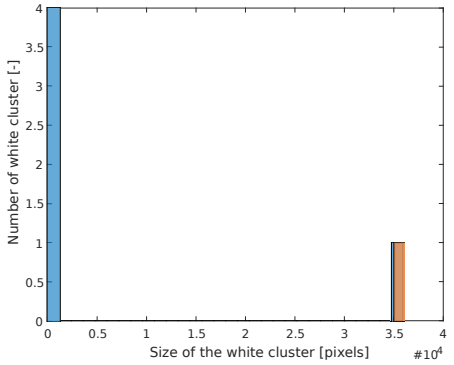

(d) Histogram of the cluster size distribution of the random pattern and the semi-random pattern for an aimed VF of 90%

Figure 70: Histogram of the cluster size distribution for an aimed VF of 60% (a), 70% (b); 80% (c); 90% (d), for a dimension of cell of 200. In blue are the data for the random pattern and in orange are the data for the semi-random one.

6.2 Very first sample design

6.2.1 Sample geometry

The design of the benchmark is made to analyse the capability of the printer to repeatably print elongated features of different dimensions and to investigate the printing directions quality, the smaller dimensions that it can correctly print as suggested for making a design strategy of benchmark [27]. Such a design is done accordingly and is shown on FIGURE 71. The CAD is done using IronCAD software and extraced as a .STL file.

The sample presents lines of length $4mm$ and of various width, as well as squares of various dimensions. The goal is to check if the printing is done well depending on the printing direction and the small dimensions. Once printed, the sample will be polished, images at the microscope will be taken and compared to the pixel maps sent to the 3D printer by the post-processing software *ObjetStudio*, which is the final software to use for printing samples.

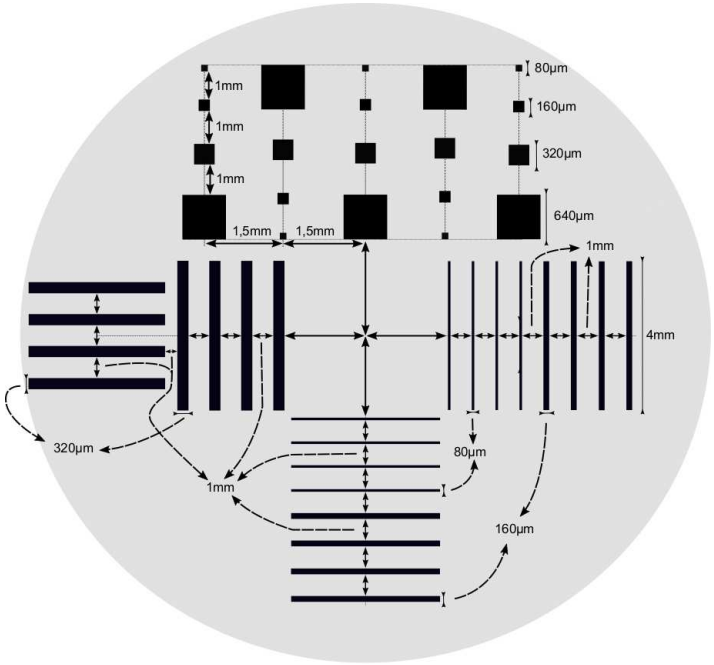

Figure 71: First design of the benchmark of the lines and squares.

6.2.2 Results

This section will compare the design obtained in the printed part with the pixel map sent directly to the printer. In order to clearly make the comparison, the different local parts composing the design will be compared separately to their corresponding local pixel map. An overview of the whole pixel map and sample can be seen on FIGURE 72.

The black areas present on the top of FIGURE 72(b) around the two squares are a solid phase resulting from the polishing. As one can see at a first look, the pixel map possesses a lot of defect that are not in the design of FIGURE 71. A closer look at those defect will be presented in the following figures. For all those figures, the printing direction is from bottom to top of the images.

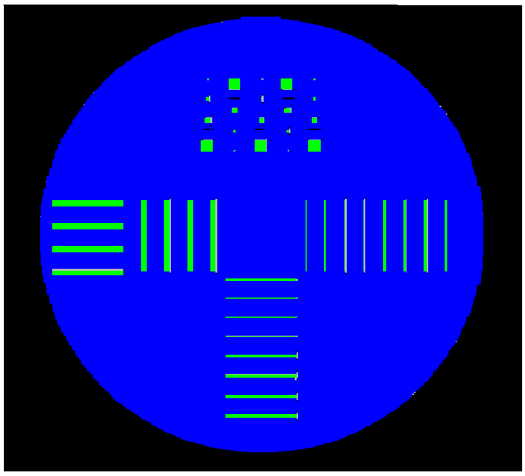

(a) Pixel map of the whole sample

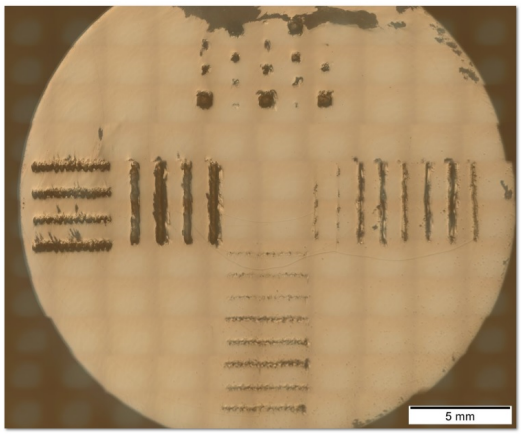

(b) The whole sample polished with silicon carbide polish 0.05µm

Figure 72: Comparison between the pixel map and the polished sample of the benchmark design represented in FIGURE 71.

As one can see on FIGURE 73(a), the lines of width 320µm are almost all respected. There are unwanted features appearing along the longitudinal axis at the border of the top horizontal lines and at the second and fourth vertical lines. Those unwanted features are a line of support and one or two holes at the side of this line. Those features do not respect the original design as there should only be TB+ composing the line-feature inside a bulk of VW+.

When looking at FIGURE 73(b), the difference in quality between the vertical lines and the horizontal one is outstanding : the horizontal lines present a very clear and pronounced staircase effect along their border while the vertical ones are smoother and so look more continuous. The lines with their longitudinal axis along the printing direction are better drawn than the ones with their longitudinal axis perpendicular to the printing direction.

The influence of the defect on the pixel map seems to result in a wider lines for the second and fourth vertical ones whereas the top horizontal one do not seem affected. The explanation for the two vertical lines would be that the line of support is removed easily during the polishing process as it is a very soft material (as well as the TB+), thus leading to a wider soft area that creates an overall wider feature. However, it would then apply also to the top horizontal line but it does not seem to affect its width. The reason is then unknown why the two vertical lines are affected and not the horizontal one. Another difference is visible on FIGURE 73(b) at the second horizontal line starting from the bottom : this line is thinner than the others horizontal ones but there is no apparent reason to it as neither in the design, neither in the pixel map anything has changed.

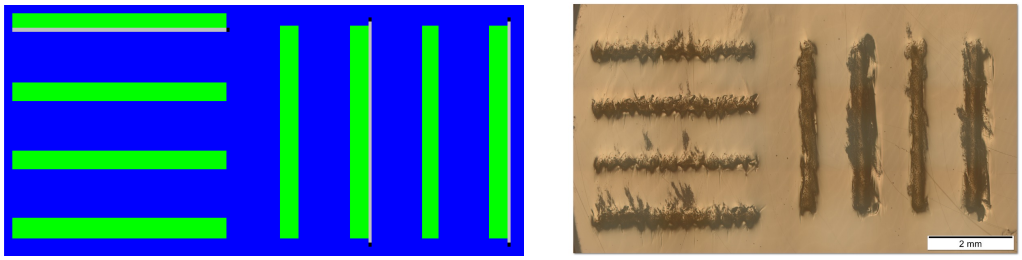

(a) Pixel map of the big lines

(b) A closer look at the big lines of the polished sample

Figure 73: Comparison between the big lines of the pixel map and the polished ones of the printed sample

On FIGURE 74(a), one can see that the pixel map contains a lot of defect compare to the initial design composed of four top horizontal lines of width 80µm and four bottom horizontal lines of width 160µm. First of all, the four bottom lines exhibit a vertical line of support and holes at the end of it on their right side. The third line starting from the bottom also has a line of support along its side. This results on FIGURE 74(b) in a defect at least as wide as the lines on their right end and the third lines seems bigger due to the line of support.

The four top lines are all different in the pixel map and only the second one from the top has the correct width. The top one is too wide as well as the third one and the fourth one is too thin but also has one line of support along its side. Even with all those differences, the results in the polished sample on FIGURE 74(b) seem the same for the first three lines starting from the top : a line so thin that it does not look continuous in the TB+ material, the lines are segmented because of their width and the staircase effect. Only the fourth line is wider, the reason seems to be the line of support that goes away easily during the polishing process.

On the overall, the quality of those lines is quite bad.

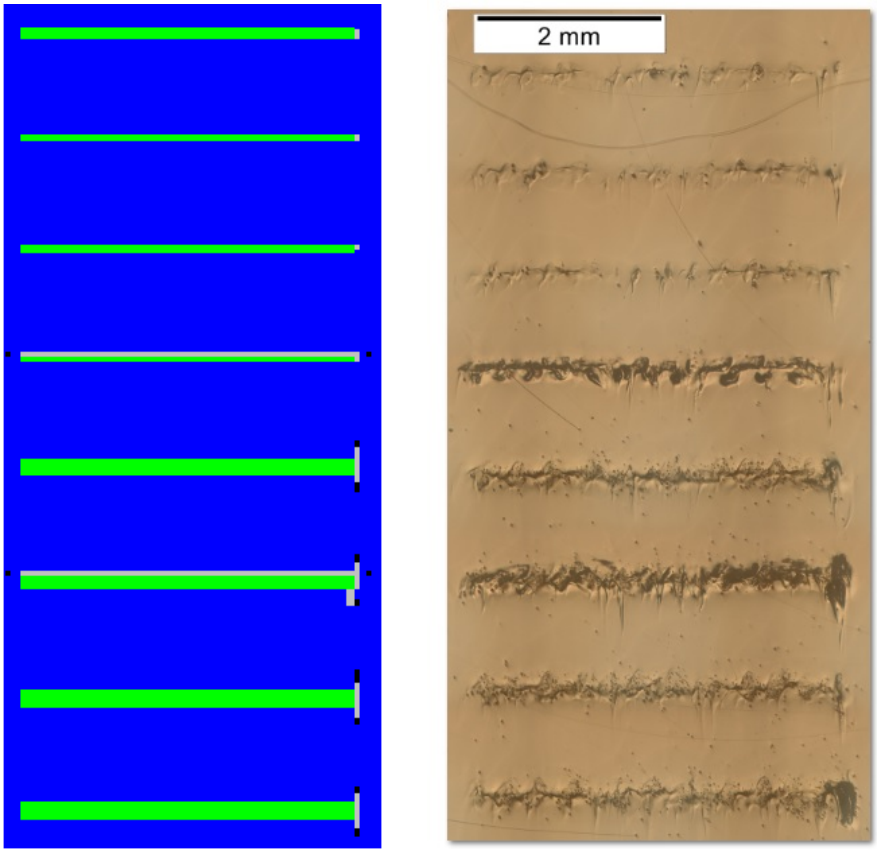

(a) Pixel map of the small horizontal lines

(b) A closer look at the small horizontal lines of the polished sample

Figure 74: Comparison between the small horizontal lines of the pixel map and the polished ones of the printed sample

As on can see on Figure 75(a), the design on the pixel map do not respect the CAD design. Supposedly, the four lines on the left are designed with a width of 80µm and the four on the right with a width of 160µm. The first two lines starting from the left have different width on the pixel map but result in almost identical polished lines on Figure 75(b), very thin and not continuous. The next two lines exhibit the same width and line of support on their right side which lead to the same result on the polished sample of a much wider line than the two very thin on their left (which they are supposed to be identical to in the CAD design).

The four lines on the right of Figure 75(a) which are suppose to be of width 160µm are also very different on the pixel map : the first one starting from the right is the only correct one, the second one is too big and with a line of support along its side, the third one is too thin with also a line of support along its side and the fourth one is too wide. However the result on Figure 75(b) is that the first line and the fourth one are quite identical and correct in their width while both lines of the center are too wide, probably due to the line of support along their side. The second one this time respecting the pixel map and being wider than the third one.

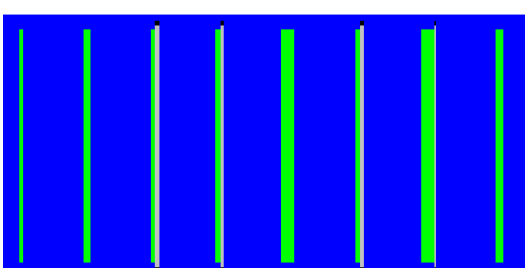

(a) Pixel map of the small vertical lines

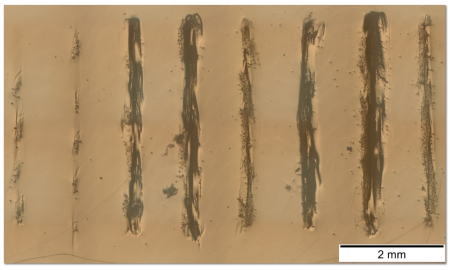

(b) A closer look at the small vertical lines of the polished sample

Figure 75: Comparison between the small vertical lines of the pixel map and the polished ones of the printed sample

Finally, the squares features are observed. As one can see, the pixel map on FIGURE 76(a) exhibits a lot of defect, almost all the the squares present some : the smallest squares are all deformed except the one on top right of the pixel map and three of them present lines of support on their side. The second smallest squares are all incorrect in their geometry and three of them exhibit lines of support wider than themselves. The second biggest squares all present lines of support on their side and holes close to them but the ones of the second and fourth column have correct geometry. The biggest squares all exhibit lines of support along at least one of their side but they respect the geometry of the CAD design except the one of the middle column. It can be noted that there are also holes of materials on each columns between the biggest square and the second biggest one.

The results on the polished sample can be seen on FIGURE 76(b). The squares on the top line are not clearly visible due to a solid phase resulting from polsihing. The two smallest squares on the bottom and the one on top in the middle column follow the geometry indicated by the pixel map. For the second smallest squares, the ones with a large line of support on their side are wider on the polished sample whereas the two others that are without support lines are not following the geometry of the pixel map and the one of the right column is almost not present. The second biggest squares are all clearly printed even though they do not respect totally the geometry of a square except the one of the second column from the right. Finally, the biggest squares are the one who respect the most the geometry indicated in the pixel map. The influence of the line of support can be seen on them as the sides where the lines are present result in a more blurred edge.

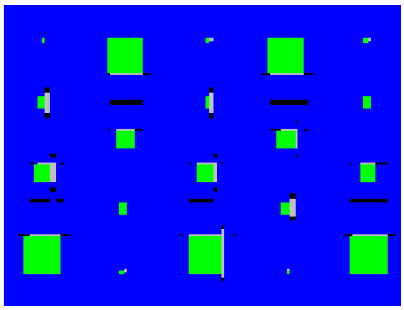

(a) Pixel map of the squares features

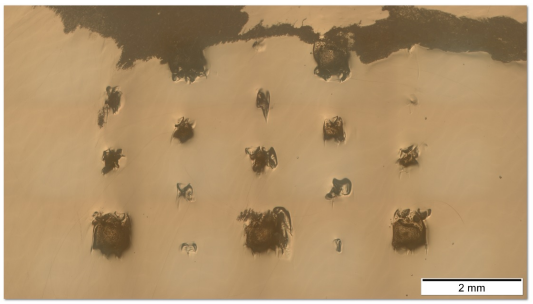

(b) A closer look at the squares features of the polished sample

Figure 76: Comparison between the squares features of the pixel map and the polished ones of the printed sample

6.2.3 Conclusion

ObjetStudio seems to introduce defect in the pixel map representing the CAD design given in input, which lead to defects in the corresponding printed part. From the comparison between the pixel map and the microscope image of the same region of features, it can be outlined that :

- The support lines along the side of features tend to make them wider in the actual printed part and with edges more blurred.

- The quality of the printing for elongated features depends on its orientation toward the printing direction. If the longitudinal axis of the elongated feature is in the direction of printing then the draw quality of the feature will be better than if this axis is perpendicular to the printing direction. It is more and more visible as the width of the elongated features decreases : for lines of width 320µm on FIGURE 73(b), both groups of lines are continuous but the ones with axis perpendicular to printing direction exhibit a strong staircase effect on their edges, whereas the ones with their axis along the printing direction are better drawn. This difference of quality is due to the working principle of the printer : the heads of the printer moves the nozzles on the x-axis at high speed, and at discrete time, droplets are deposited. They are not deposited while the head moves along the y-axis. Those very small droplets, by inertia and because of the roller, spread along the direction of printing, leading to this continuous line feature which is not present in the other direction. Instead in this other direction, the staircase effect is clearly visible due to the dithering pattern being respected by the droplets deposition.

- There is a certain limit of width under which the printer cannot warranty and effective printing and respect of the geometry,as said in the datasheet and by Meisel [33]. It can be seen on FIGURE 74(b) and FIGURE 75(b) that for lines of 80µm, the lines are not continuous anymore and that the staircase effect is so strong that they look made out of pixel of TB+. It is to note also that at specific spots there is no TB+ anymore but just VW+, this is probably due to the miscibility of the TB+ and the VW+, the TB+ being so few that it mixes in the bulk of VW+ around it.

- The holes in the bulk material of VW+ indicated by the pixel map on FIGURE 76 are not present anymore in the printed sample. Instead they are filled with VW+ : it is assumed that as the holes are very small they are filled by the action of the roller and by the capillary attraction of the droplet of VW+ forming the bulk around it.

It is unclear why sometimes the printed result do not follow the geometry indicated by the pixel map, as the top lines on FIGURE 74 and the fourth lines from the right on FIGURE 75.

6.2.4 Sample design for inverse materials

The opposite configuration, i.e. a matrix of TB+ in which they are features of VW+ has also been tested. Such a sample has been printed and put into resin, as the TB+ is a rubbery material, for proceeding to polishing. The polishing has been conducted until the smallest grain size paper (P2500) and the polishing paste for going into a finer polishing were not used as the paste would be trapped inside all the matrix of TB+ making the features unvisible. An image of the resulting sample is shown on FIGURE 77.

As one can see, all the features are present and visible except for the smaller squares who disapeared. It is to note also biggest squares and lines exhibit the characteristic white color of the VW+, the thinner the lines and squares become, the less they are in intensity of white. This can be explained by either the fact that as the polishing is less precise, the surface of the thin VW+

features is not smooth enough to correctly reflect the light and so only the biggest features looks white because of their greater width that quantitatively relfects more light, either it is because the miscibility of small droplets of VW+ inside a matrix of TB+ is greater than the opposite, i.e. the miscibility of small droplets of TB+ inside a matrix of VW+, either it a combination of both phenomena.

Also on FIGURE 77, it is visible that concerning the small vertical lines, three of the four lines of width 85µm are incorrect as they visually are as wide as the vertical lines of thinner width 42.5µm. Only the one on the right is wider.

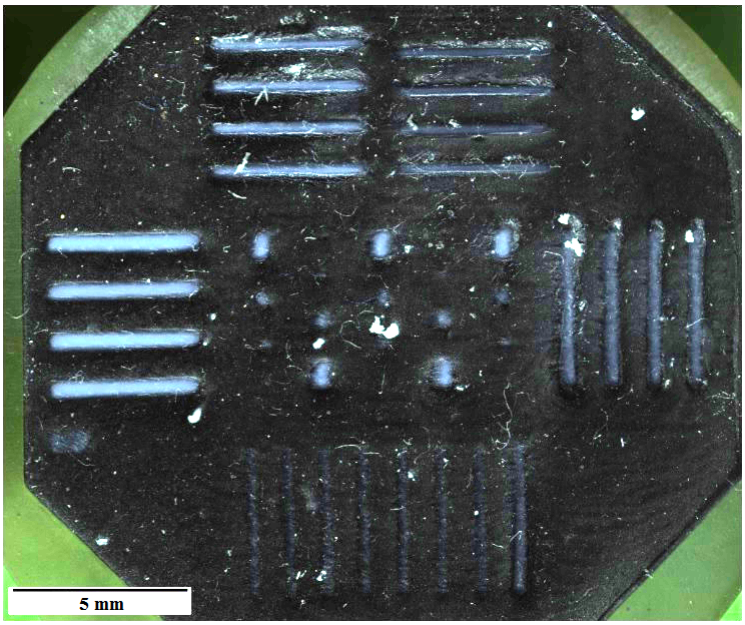

Figure 77: Polished sample of TB+ matrix and VW+ features

An exhaustive analysis of the features quality and fidelity to its bitmap will not be performed here. Instead, the results of the average measurements will be presented in FIGURE 9. Only the biggest squares could be measured correctly, all the others are either to small or to blurred to take any valuable measurement.

Feature	Mean length	Mean width
Big horizontal (4250µm x 340µm)	4211.7µm	377.2µm
Medium horizontal (4250µm x 170µm)	4162.7µm	259.9µm
Small horizontal (4250µm x 85µm)	4233.1µm	228.3µm
Big vertical (4250µm x 170µm)	4254.1µm	296.2µm
Medium vertical (4250µm x 85µm)	4077.2µm	229.6µm
Small vertical (4250µm x 42.5µm)	4141µm	214.4µm
Biggest squares (680µm x 340µm)	719.7µm	369.6µm

Table 9: Mean length and width of the line and squares features

It appears that while the length of all lines are of correct length with a maximum error of 4%, the width of those features are highly incorrect (from 53% to 403 %) except for the big horizontal lines. Such an error can not be explained only by the possible lack of accuracy due to a more superficial polishing. However, the lines and squares of higher dimension exhibit much less error : 11% for the big horizontal lines and 8% for the biggest squares. No lines supposed to be of width 170µm or thinner are below 200µm. It seems that there is a critical dimension under which the

width of the feature can not be respected and is limited to a value above 200µm. The explanation is probably related to the miscibility of the two materials.